

# HYDROPHOBIC HYDRATION OF A SINGLE POLYMER

by

Isaac T. S. Li

A thesis submitted in conformity with the requirements  
for the degree of Doctor of Philosophy  
Department of Chemistry  
University of Toronto

© Copyright 2012 by Isaac T. S. Li

# Abstract

## Hydrophobic Hydration of a Single Polymer

Isaac T. S. Li

Doctor of Philosophy

Graduate Department of Chemistry

University of Toronto

2012

Hydrophobic interactions guide important molecular self-assembly processes such as protein folding. On the macroscale, hydrophobic interactions consist of the aggregation of “oil-like” objects in water by minimizing the interfacial energy. However, the hydration mechanism of small hydrophobic molecules on the nanoscale ( $\sim 1$  nm) differs fundamentally from its macroscopic counterpart. Theoretical studies over the last two decades have pointed to an intricate dependence of molecular hydration mechanisms on the length scale. The microscopic-to-macroscopic cross-over length scale is critically important to hydrophobic interactions in polymers, proteins and other macromolecules. Accurate experimental determination of hydration mechanisms and their interaction strengths are needed to understand protein folding.

This thesis reports the development of experimental and analytical techniques that allow for direct measurements of hydrophobic interactions in a single molecule. Using single molecule force spectroscopy, the mechanical unfolding of a single hydrophobic homopolymer was identified and modeled. Two experiments examined how hydrophobicity at the molecular scale differ from the macroscopic scale. The first experiment identifies macroscopic interfacial tension as a critical parameter governing the molecular hydrophobic hydration strength. This experiment shows that the solvent conditions affect the microscopic and macroscopic hydrophobic strengths in similar ways, consistent with theoretical predictions. The second experiment probes the hydrophobic size effect by studying how the size of a non-polar side-chain affects the thermal signatures of hy-

dration. Our experimental results reveal a cross-over length scale of approximately 1 nm that bridges the transition from entropically driven microscopic hydration mechanism to enthalpically driven macroscopic hydration mechanism. These results indicate that hydrophobic interactions at the molecular scale differ from macroscopic scale, pointing to potential ways to improve our understanding and predictions of molecular interactions. The system established in this thesis forms the foundation for further investigation of polymer hydrophobicity.

## Acknowledgements

The pursuit of truth is fun and exciting, but what made this PhD so meaningful and memorable is the wonderful group of people in my life over the past 5 years. What I have learned go far beyond science. Foremost, I want to express my deepest gratitude to Prof. Gilbert C. Walker, my PhD advisor. I was drawn by his passion and curiosity for science since our very first meeting. His persistence, wild imagination and rigorous attitude towards science helped me push through numerous obstacles to answer deeper questions. Gilbert has always been considerate, supportive, and has offered invaluable advices not only in science, but also in life, for which, I am forever thankful.

I want to thank my thesis committee members, Prof. Raymond Kapral, Prof. Stuart Whittington, and Prof. Christopher Yip for overseeing the progress of this thesis and contributing many insightful discussions. I am grateful to Prof. John Polanyi for kindly agreeing to be on my defense committee with short notice. To Prof. Shekhar Garde and Prof. Dor Ben-Amotz, thank you both for offering invaluable discussions on the interpretations and implications of my experimental results; your encouragements are motivating and are highly appreciated. Finally, I am grateful to Prof. Sudipta Maiti and Prof. Matthew Paige for sharing their expertise.

To my friends from the Walker Labs, Dr. Nikhil Niki Gunari, Dr. Shan Zou, Dr. Shell Ip, Dr. Ruby May Sullan, Dr. Weiqing Shi, Dr. James Li, Dr. Zahra Fakhaari, Adrienne Tanur, Claudia Grozea, Melissa Paulite, Christina MacLaughlin, Michelle Joseph, and Mandy Koroniak, thank you for being such a friendly, supportive, encouraging, and cohesive group! I owe much of my success to Dr. Gunari, who mentored me on single molecule force spectroscopy. Dr. Gunari began the work on hydrophobic polymer pulling experiments and taught me many experimental tricks. A particular trick named after him, the Niki-shot has been widely applied in many measurements. Without the experimental foundations Dr. Gunari has previously laid, this thesis would not have progressed this far. I am grateful to Dr. Shan Zou, currently at the NRC, who patiently taught me AFM and answered many questions about force spectroscopy. Being in a group with diverse expertise, I had the privilege and opportunities to take numerous measurements with Dr. Shell Ip, Dr. Nikhil Gunari, Adrienne Tanur, Dr. Weiqing Shi, Michelle Joseph, Christina MacLaughlin, and Dr. Zahra Fakhaari to learn, discuss, and improve various techniques. Thanks to the comments and feedbacks from Dr. Shell Ip, Dr. James Li, Dr. Ruby May Sullan, Adrienne Tanur, Melissa Paulite, and in particular, Michelle Joseph, I learned to better communicate science. I am indebted to Mandy Koroniak and Anna Liza Villavelez for their assistance that made my graduate life so much easier.

Working with members from the group has been fun and inspiring. I have learned

a great deal from a number of enjoyable and spontaneous collaborations, in particular, with Dr. Weiqing Shi, Claudia Grozea, and Melissa Paulite. I want to thank Dr. Weiqing Shi for many thoughtful discussions and suggestions, and for her assistance from protein expression to single molecule experiments. I want to thank Claudia Grozea for sharing experiment ideas, making countless samples and working long hours in front of the AFM with me. The collaboration with Melissa Paulite had been a daring endeavor. Besides interesting ideas that sprang from our discussions, her dedication, focus, and never-giving-up spirit were inspiring. To Dr. Zahra Fakhaari, currently at UPenn, I enjoyed our continuous science discussions.

I wish to take this opportunity to offer my best wishes to all my friends from the Walker group.

I want to thank my parents for their continuous and unconditional support through my 22 years of schooling. I promise, no more tuition! In particular, I want to thank my mom for the most wonderful food; it was suggested by an insider that I would have been a malnourished nerd without her balanced recipe. And thanks to my dad for the occasional surprises that allowed me to catch some fresh air in the most breathless days of my PhD.

And to my beloved Winnie, your simple presence is light in my darkest moments and sunshine in my finest hours. You added a new dimension full of laughter and joy to my life.

Isaac Li  
Milton, Ontario  
June 25, 2012

# Contents

<b>1</b>	<b>Introduction</b>	<b>1</b>
1.1	Hydrophobic interactions at molecular scale . . . . .	1
1.2	Studying molecules, one at a time . . . . .	2
1.3	Thesis Organization . . . . .	4
<b>2</b>	<b>Hydrophobic Hydration</b>	<b>7</b>
2.1	Macroscopic interfacial thermodynamics . . . . .	8
2.2	Small molecule hydration anomalies . . . . .	9
2.3	Hydrophobic size effect . . . . .	10
<b>3</b>	<b>Single Molecule Force Spectroscopy</b>	<b>14</b>
3.1	Principles of Atomic Force Microscopy . . . . .	15
3.2	Using AFM for single molecule force spectroscopy . . . . .	17
3.2.1	Strategies for tethering a single molecule . . . . .	18
3.2.2	Comparison between force spectroscopy techniques . . . . .	21
3.3	Cantilever calibrations . . . . .	22
3.3.1	Preparation of calibration substrate . . . . .	22
3.3.2	Calibration of cantilever sensitivity . . . . .	23
3.3.3	Calibration of cantilever spring constant . . . . .	24
3.4	Force-extension curves . . . . .	25
3.5	Mechanical noise control . . . . .	26
3.5.1	Acoustic noise . . . . .	26
3.5.2	Floor vibration noise . . . . .	27
3.5.3	Evaluation . . . . .	28
3.6	Environment control . . . . .	30
3.7	Drift control . . . . .	30
3.7.1	Thermal drift . . . . .	31
3.7.2	Optical sensitivity drift . . . . .	32

3.8	Contamination control . . . . .	33
3.9	Conclusion . . . . .	34
<b>4</b>	<b>Theories of Single Polymer Pulling</b>	<b>36</b>
4.1	Polymers in good solvents . . . . .	37
4.1.1	Freely jointed chain (FJC) model . . . . .	37
4.1.2	Worm-like chain (WLC) model . . . . .	42
4.2	Polymers in poor solvents . . . . .	44
4.2.1	Analytical model of pulling a single chain from collapsed state . . . . .	45
4.2.2	Ising model simulations . . . . .	50
4.3	Conclusion . . . . .	57
<b>5</b>	<b>Experiments of Hydrophobic Polymer Pulling</b>	<b>59</b>
5.1	Typical force curve of hydrophobic homopolymer unfolding . . . . .	59
5.2	Extract hydration free energy from force curves . . . . .	61
5.3	Methods and materials . . . . .	62
5.3.1	Substrate preparation . . . . .	62
5.3.2	Polymer preparation . . . . .	63
5.4	Evidence of single chain unfolding due to hydrophobic hydration . . . . .	64
5.4.1	Surface topography of a single polymer . . . . .	65
5.4.2	Surface independence of plateau force . . . . .	68
5.4.3	Step size distribution of multiple force plateaus . . . . .	68
5.4.4	Consistent last force plateau marks unfolding of a single chain . . . . .	70
5.4.5	Normalization of contour length . . . . .	71
5.4.6	Length distribution of the last force plateau . . . . .	71
5.4.7	Reversibility and velocity independence of plateau force . . . . .	72
5.5	Conclusion . . . . .	76
<b>6</b>	<b>Single Molecule Data Analysis</b>	<b>77</b>
6.1	Automated data analysis program design . . . . .	77
6.2	InvOLS correction . . . . .	80
6.3	Baseline tilt correction . . . . .	81
6.4	Rupture point detection . . . . .	83
6.4.1	Differential detection . . . . .	83
6.4.2	Hypothesis test detection . . . . .	84
6.5	Drag correction . . . . .	85
6.6	Statistical analysis of force plateaus . . . . .	89

6.7	Graphical User Interface (GUI)	90
6.8	Conclusion	91
<b>7</b>	<b>Solvent Dependence of Hydrophobic Hydration</b>	<b>93</b>
7.1	Introduction	94
7.2	Methods and materials	96
7.2.1	Sample preparation	96
7.2.2	Single molecule force spectroscopy	96
7.3	Determination of macroscopic interfacial tension	96
7.4	Unfolding polystyrene in aqueous solutions	99
7.5	Unfolding polystyrene in good solvents	101
7.6	Correlation between extension force and interfacial tension	102
7.7	Interfacial tension provides solvent condition on microscopic scale	104
7.8	Conclusion	105
<b>8</b>	<b>Temperature &amp; Size Dependence of Hydrophobic Hydration</b>	<b>107</b>
8.1	Introduction	107
8.2	Methods and materials	109
8.2.1	Choosing polymers	109
8.2.2	Polymer sample preparation	109
8.2.3	Single molecule force spectroscopy	110
8.2.4	Renormalization of forces	111
8.3	Single chain hydration responsible for force plateau in all three polymers	112
8.4	Temperature and size dependencies of single chain hydration	113
8.4.1	PS unfolding energy is temperature dependent	114
8.4.2	Differences in temperature dependence due to side-chain sizes	115
8.4.3	Significance of the temperature and size dependence	119
8.5	Other sources of possible temperature dependencies	123
8.5.1	Temperature dependence of polymer desorption from surface	124
8.5.2	Temperature dependence of cantilever spring constant	126
8.5.3	Temperature dependence of the piezoelectric actuators	126
8.6	Conclusion	128
<b>9</b>	<b>Summary and Future Work</b>	<b>129</b>
9.1	Summary	129
9.2	Ongoing and future work	130

<b>Bibliography</b>	<b>135</b>
<b>A Derivation &amp; Numerical Solution of Analytical Model</b>	<b>153</b>
<b>B Derivation of Expected End-to-end Distance in FJC Model</b>	<b>155</b>

# List of Tables

3.1	Comparison of single molecule force spectroscopy techniques . . . . .	22
4.1	List of parameters used in the analytical model . . . . .	47
4.2	List of surface area, distance and degeneracy of non-overlapping polymer model . . . . .	53
4.3	List of surface area, distance and degeneracy of the modified polymer model	53
5.1	Force plateau magnitude using different tip-surface combinations . . . . .	68
7.1	Dispersive and polar contributions to surface tensions of PS . . . . .	98
7.2	Dispersive and polar contributions to surface tensions of various solvents	99
7.3	Plateau force increases in NaCl solution . . . . .	100
8.1	Experimental data of the temperature dependence of the plateau force. .	115

# List of Figures

1.1	Hydrophobic polymer as model for protein collapse . . . . .	3
2.1	Anomalous temperature dependence of small molecule hydration $\Delta G$ . .	10
2.2	Theoretical prediction of hydrophobic size effect . . . . .	12
3.1	World's first AFM . . . . .	14
3.2	AFM micro-cantilever . . . . .	15
3.3	Laser detection scheme of cantilever deflection . . . . .	16
3.4	AFM feedback control . . . . .	17
3.5	Single molecule force spectroscopy by AFM . . . . .	18
3.6	Topography scan of fibronectin molecules . . . . .	19
3.7	AFM topography scan can scratch samples . . . . .	20
3.8	Single molecule events correlate to surface topography scan . . . . .	20
3.9	Single molecule attachment strategies . . . . .	21
3.10	AFM cantilever calibration . . . . .	24
3.11	Power spectra of an AFM cantilever . . . . .	25
3.12	AFM distance relations . . . . .	26
3.13	Transmissibility spectrum of the AFM acoustic isolation enclosure . . . .	27
3.14	Transmissibility spectrum of a passive vibration isolation table . . . . .	27
3.15	Two stage vibration isolation strategy . . . . .	28
3.16	Evaluation of vibration isolation strategies . . . . .	29
3.17	Closed fluid cell assembly . . . . .	30
3.18	Temperature induced bending of the AFM cantilever . . . . .	31
3.19	Cantilever deflection drift . . . . .	32
4.1	Freely jointed chain . . . . .	37
4.2	FJC force-distance response . . . . .	42
4.3	The worm-like chain. . . . .	43
4.4	Comparison of WLC, FJC and Gaussian chain force-distance response curves	44

4.5	Force extension curve of polystyrene in good solvent . . . . .	44
4.6	Studies of homopolymer unfolding in poor solvent . . . . .	45
4.7	Results of the simple analytical model . . . . .	48
4.8	Illustration of the solvent model on a 2D lattice . . . . .	51
4.9	Configurations between two adjacent non-overlapping polymer units . . .	52
4.10	Modified model allowing some overlapping between adjacent polymer units	53
4.11	Simulation of hydrophobic polymer collapse in water . . . . .	54
4.12	Radius of gyration trajectories of hydrophobic and hydrophilic polymers	55
4.13	Simulation of polymer in good solvent fits the WLC model . . . . .	56
4.14	Simulation of polymer collapse under tension . . . . .	56
4.15	Equilibrium end-to-end distance and fluctuation vs. external tension . . .	57
5.1	Single molecule pulling experiment of a hydrophobic polymer . . . . .	60
5.2	Typical AFM force-extension curve of a hydrophobic polymer . . . . .	60
5.3	Calculate $\Delta G^{hyd}$ per monomer from pulling experiments . . . . .	61
5.4	Polymer deposition checked by contact angle . . . . .	64
5.5	Mechanical unfolding of GB1 protein . . . . .	65
5.6	The alternative mechanism that can give rise to force plateau profiles . .	66
5.7	Surface topography of polystyrene deposited on Si surface . . . . .	67
5.8	Conformation of DNA adsorbed on mica surface . . . . .	68
5.9	Uniform and non-uniform force plateau step size distribution . . . . .	69
5.10	Mechanism behind uniform and non-uniform step size distributions . . .	70
5.11	Discrete distribution of force plateau by overlapping hundres of force curves	71
5.12	Contour length normalized force-extension curves can be superimposed .	72
5.13	Plateau length distribution from PS . . . . .	73
5.14	Pulling velocity dependence of plateau force . . . . .	74
5.15	Schematic of the energy landscape of the pulling experiment . . . . .	75
6.1	Data analysis program structure . . . . .	78
6.2	Data analysis program flow diagram . . . . .	79
6.3	invOLS corrected and uncorrected force curves . . . . .	81
6.4	Identifying the indentation portion of force curve . . . . .	82
6.5	Force curves before baseline correction . . . . .	83
6.6	Differential detection method for rupture events . . . . .	84
6.7	Hypothesis test rupture detection test cases . . . . .	86
6.8	Effects of solvent viscous drag on the force curves . . . . .	87
6.9	Tip velocity calculation from force curves . . . . .	88

6.10	Statistical analysis of plateau force trajectories . . . . .	89
6.11	Distribution of the mean force . . . . .	90
6.12	GUI for loading and filtering force curves . . . . .	91
6.13	GUI for force curve analysis . . . . .	92
7.1	Plateau force and interfacial tension as a function of ethanol concentration	100
7.2	Discrete force plateaus from overlapping force curves . . . . .	100
7.3	Pulling PS in toluene . . . . .	101
7.4	Correlation between plateau force and $\gamma_{ps}$ . . . . .	103
7.5	Theoretical solvent dependence of hydrophobic size effect . . . . .	105
7.6	Relating solvent-dependence experiment results to theory . . . . .	106
8.1	The three hydrophobic polymers used in this study . . . . .	110
8.2	Temperature sequences used in the experiment . . . . .	111
8.3	Normalizing the temperature dependence data from several independent experiments . . . . .	112
8.4	AFM topography and cross-section analysis of PVBP on Si . . . . .	113
8.5	The temperature dependence of PS plateau force distributions . . . . .	114
8.6	Size and temperature dependence of polymer hydrophobic hydration . . . . .	116
8.7	Temperature dependencies of hydration entropy, enthalpy and free energy of PtBS . . . . .	119
8.8	Molecular structure of a short segment of PS . . . . .	120
8.9	Transfer free energy from water to hexadecane at 298 K for small alkanes and derivatives . . . . .	122
8.10	The effect of temperature on the size-dependence of hydration . . . . .	123
8.11	Relating experimental results to theoretical hydrophobic size effect . . . . .	124
8.12	Theoretical temperature dependence of polymer desorption force curves . . . . .	125
8.13	Temperature dependence of the Youngs modulus of the cantilever . . . . .	127
8.14	Temperature dependence of the piezoelectric actuator . . . . .	127
9.1	Molecular volume vs. area of 118 small hydrocarbons. . . . .	131
9.2	The rugged energy landscape of hydrophobic polymer unfolding . . . . .	132
9.3	Velocity dependent plateau force at very high pulling velocities . . . . .	133

# Chapter 1

## Introduction

The hydrophobic effect describes the apparent “dislike of water” by materials such as oil and wax. The characteristic unfavorable interaction energy between water and hydrophobic materials drives their self-association hence we call it the “hydrophobic effect”. The hydrophobic effect is a major driving force behind numerous phenomena we see daily such as the cleaning action of detergent and the beading of water on wax. In all these macroscale scenarios, the unfavorable interfacial free energy arises from loss of one hydrogen bond, on average, for each water molecule at the interface with the non-polar material. This large enthalpic cost drives the system to reduce the contact area.

However, as the size of the system shrinks to the microscopic scale, the physics of the hydrophobic effect changes too. On this length scale, the assumption of an extended planar surface no longer holds, making it difficult to define an exact “surface”. In addition, as the hydrophobe shrinks to about one nanometer (several water molecules), hydrogen bonds of water molecules in the hydration shells no longer need to be sacrificed, making the hydration physics entirely different for small molecules on the microscopic scale.

### 1.1 Hydrophobic interactions at molecular scale

Water actively mediates the interactions between biological molecules on the microscopic scale. On this scale (order of one nanometer), a non-polar molecule can be incorporated in water’s dynamic hydrogen bond network without breaking any hydrogen bonds. However, the configurational freedom of the surrounding water is obstructed in doing so, giving such arrangement a high entropic cost. The implications of this for hydrophobic interactions at the molecular scale are not fully understood.

Hydrophobic interaction is considered a fundamental determinant of the self-assembly of biological macromolecules into ordered structures, in particular, protein folding [15,

11, 101]. During folding, the non-polar amino acids induce the hydrophobic collapse of proteins into compact structures. Simulations indicate that the sequence of hydrophobic residues in a peptide alone can encode the secondary and tertiary structure of a protein [38]. Therefore, understanding molecular hydrophobic interactions in polymers and proteins is vital to understanding protein folding and achieving better engineering controls in macromolecular systems.

The thermodynamics of hydrophobic interactions are subtle, both to model and measure. At equilibrium, the free energy of hydrophobic interaction is the difference between the hydration free energies of the systems before and after the interaction. Therefore, the hydrophobic interaction strength relies on accurate assessment of the hydration behavior of hydrophobic species (hence the oxymoronic term “hydrophobic hydration”). Significant theoretical efforts have advanced the understanding of hydrophobic hydration from microscopic to macroscopic length scales (see reviews [15, 5, 32, 91, 14, 183, 39, 84, 71, 153]). A natural question is: what are the length-scales operating in polymers and proteins? The length of extended polymers is macroscopic (hundreds of nanometers), the side-chains are microscopic (sub-nanometer), and the folded structure is somewhere in between. Theoretical studies on polymer hydration have been sparse [57, 166, 7, 170] as have been direct experimental studies [149, 60, 68, 105, 106]. Although hydrophobic interactions in proteins can be studied by amino-acid substitutions, the interactions are usually complicated by their innately complex intra-molecular interactions. Furthermore, whether the hydrophobic interior of a protein can be treated as a simple non-polar solvent is still debated, making it inappropriate to directly apply traditional amino acid transfer free energy obtained between water and organic solvents. Therefore, direct experimental measurement of polymer unfolding is needed to determine the energy of hydrophobic collapse. Hydrophobic homopolymers are good candidates for studying hydrophobic interactions and hydrophobic collapse in proteins due to their chemical homogeneity and the abundance of theoretical predictions (Figure 1.1). However, the polymers’ insolubility in water and the difficulties to change the polymer conformation have been obstacles for traditional bulk measurements.

## 1.2 Studying molecules, one at a time

Traditional bulk experiments measure the ensemble average of molecular properties in response to perturbations such as temperature and solvent. With high signal to noise ratio, these measurements can be reliably and quickly performed. However, ensemble measurements suffer from two major drawbacks: 1. the molecular mechanisms and dy-

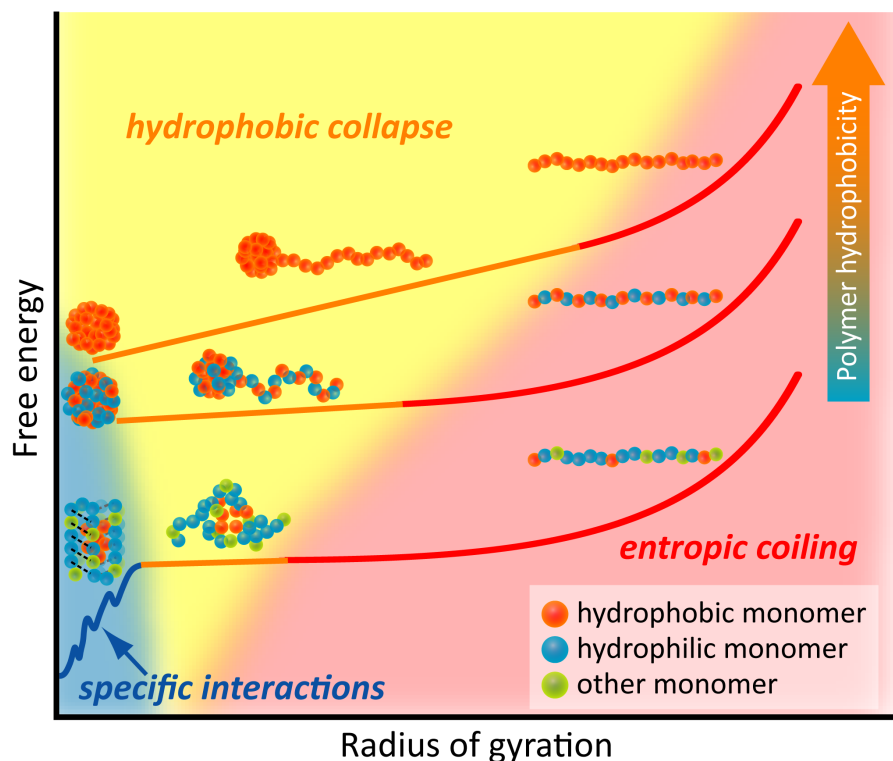


Figure 1.1: A hydrophobic polymer provides a model for hydrophobic collapse in proteins and other macromolecules. From top to bottom, in order of decreasing hydrophobicity, are a homopolymer, a co-polymer, and a protein. Starting from an extended conformation in water, chains coil under entropic elastic driving force (red). When sufficiently relaxed, hydrophobic collapse (yellow) occurs and reduces the size of the collapsed globule. Hydrophobic collapse in less hydrophobic copolymers and proteins occurs at later stages due to lower hydrophobic driving forces. For proteins, specific interactions (blue) plus the formation of secondary structures bring the protein to an energy minimum with a more compact structure. Hydrophobic polymers do not have such specific interactions and collapse to compact, random coils.

namics cannot be easily followed, and 2. only the most populated molecular states are detected.

For example, an enzyme that rapidly fluctuates between two conformational states will appear as an averaged conformation in ensemble measurement. Furthermore, if an enzyme modulates activities by the duration in one of the two conformations, the apparent ensemble measurement will show a gradually change of the enzyme's conformation. Furthermore bulk measurement of the dynamics of molecules in response to external factors (i.e. chemical and thermal) is limited by diffusion, and hence the detected molecular dynamics is convolved with the probing event. Therefore, in order to study the dynamics of the molecular mechanism, one needs to follow the reaction trajectory of a single molecule. Furthermore, the ability to manipulate the conformation of molecules is also quite limited in bulk experiments. Therefore, only the most populated conformational states can be detected, making it difficult to probe the properties of the molecule in a less populated state.

The above limitations imposed by conventional bulk experiments are overcome by recent single molecule techniques. In particular, single molecule force spectroscopy allows one to simultaneously manipulate and monitor molecular properties of a single molecule at a time. Using the optical tweezers or atomic force microscopy, one molecule can be pulled into extended conformations that bulk measurements cannot access with large enough population. It has been shown that mechanical unfolding of proteins follow the same pathway as chemical unfolding [30], making such studies by force spectroscopy a comparable alternative to bulk experiments.

In this thesis, single molecule force spectroscopy was used to unfold a single hydrophobic homopolymer in water and measure the hydration free energy ( $\Delta G^{hyd}$ ), a process so energetically unfavorable that it would not be observed under bulk measurement conditions. The dependence on solvent condition, temperature, and the size of polymer side-chain were studied. The results provided evidence that the signature of polymer hydrophobic hydration closely resemble those of small molecules, rather than macroscopic objects.

### 1.3 Thesis Organization

The primary objective of this thesis is to study the hydrophobic effect in a single macromolecule using the atomic force microscopy. In particular, we want to understand how the hydrophobic effect at molecular level differs from macroscopic level. Single molecule techniques were developed to unfold hydrophobic polymers. Furthermore, analysis meth-

ods were developed to detect and process single molecule events and uncover the energy of hydrophobic interaction from such experiments.

- Chapter 2: Theoretical background on hydrophobic hydration is described and how its recent development inspired the experiments undertaken in this thesis. Particular attention is given to the anomalous hydration behavior of small non-polar molecules and the hydrophobic size effect that arise from it.
- Chapter 3: Atomic force microscopy is introduced with particular attention given to its application in single molecule force spectroscopy. Experimental methods to run single molecule force spectroscopy are discussed in detail, including: cantilever calibration, noise control, environment control, and contamination control.
- Chapter 4: The polymer physics models needed to understand the mechanical pulling of polymers in a single molecule force spectroscopy experiment are provided in this chapter. The entropic elastic behaviors of polymers in good solvents are described using the freely-jointed chain model and the worm-like chain model. In addition, an analytical model and an Ising model are developed to describe the pulling behavior of polymers in poor solvents, which has a signature force plateau due to hydrophobic hydration.
- Chapter 5: Single molecule pulling experiments on hydrophobic polymers are described in detail in this chapter. The resulting force curves containing force plateaus are interpreted and compared with theoretical predictions from Chapter 4. This chapter provides evidence for why the force plateau is a signature of single molecule event, and why such plateau is caused by hydration events rather than other mechanisms that may generated force plateaus.
- Chapter 6: This chapter describes the development of automated data analysis methods.
- Chapter 7: With the above development as foundation, this chapter describes how solvent condition affects the hydrophobic hydration of a single hydrophobic polymer. The relationship between the hydration energy of the polymer on the microscopic scale and interfacial tension on the macroscale is discussed.
- Chapter 8: This chapter describes how the hydrophobic hydration of a single polymer depends on both temperature and size of polymer side-chain. The temperature dependence found in polymer hydration resembles those found in small non-polar molecules, indicating a length-scale dependent hydration mechanism exists for

macromolecules such as polymers and proteins. The interpretation and implication of the results are provided.

- Chapter 9: Conclusion of the thesis as well as the ongoing and future directions to continue the work reported here.

# Chapter 2

## Hydrophobic Hydration

The hydration of a solute describes the process to insert the solute into water. This process can be separated into two steps: first, a cavity in water is created to host the solute; then the solute is placed into the cavity establishing interactions with interfacial water. The first step of cavity creation is energetically unfavorable due to disruptions to its hydrogen bond network such as breaking water molecule contacts and constraining the configurational freedom of bonded water molecules. The special properties of water's hydrogen bond network make water molecules highly cohesive as suggested by water's large surface tension; this gives rise to a particularly large energetic penalty for cavity creation. The second step of placing the solute into the cavity is energetically favorable as interactions between water and solute such as hydrogen bonds, electrostatic, polar, and dispersive interactions are usually attractive. What determines solubility is the balance between the penalty from cavity creation and the reward from establishing solute-water attractions.

Hydrophobic hydration describes the process to insert a hydrophobic solute into water. What differentiates a hydrophobic solute is the relatively weak solute-water attraction that allows the cavitation free energy  $\Delta G^{cav}$  to dominate the overall hydration free energy  $\Delta G^{hyd}$ . The large unfavorable  $\Delta G^{hyd}$  makes the solute less soluble and hence, hydrophobic. Therefore, cavity formation and its associating  $\Delta G^{cav}$  are vital to understanding hydrophobic hydration.

When we consider a macroscopic object such as an oil droplet in water,  $\Delta G^{cav}$  is mostly due to the loss of hydrogen bonds of interfacial water. The volume expansion work at 1 atmospheric pressure is negligible comparing to the bond breaking enthalpy. Therefore,  $\Delta G^{cav}$  is proportional to the surface area of the solute in what has been traditionally understood as the interfacial thermal dynamics (Section 2.1). On the other hand, the anomalous hydration behavior of a small non-polar molecule like methane

indicates the breakdown of interfacial thermodynamics, as the molecular size is on the same order of magnitude as water molecules.  $\Delta G^{cav}$  to create a small cavity in water does not require breaking hydrogen bonds. Instead, the entropic cost of restructuring of water molecules in the hydration shells is believed to contribute to  $\Delta G^{cav}$  (Section 2.2). Recent theoretical efforts aiming to explain the small molecule anomalies lead to the development of hydrophobic size effect, which will be reviewed in Section 2.3.

## 2.1 Macroscopic interfacial thermodynamics

From the aggregation of oil in water to the lotus effect, the classic hydrophobic effect is dominated by macroscopic interfacial thermodynamics where the minimization of the unfavorable total interfacial free energy  $G$  is accomplished by reduction of interfacial surface area  $A$ .

$$\Delta G = \gamma \Delta A \quad (2.1)$$

The phenomenological model assumes a linear relationship between  $G$  and  $A$ , where the interfacial tension  $\gamma$  is the scaling factor. The interfacial tension can be calculated from the surface tension of solvent  $\gamma_{solvent}$ , solute,  $\gamma_{solute}$  and the work of adhesion,  $W_{ad}$ , describing the attractive interactions:

$$\gamma = \gamma_{solute} + \gamma_{solvent} - W_{ad} \quad (2.2)$$

The work of adhesion arises from contributions from the dispersive and polar components of the solvent and solute surface tensions, according to extended Fowkes equation [50]:

$$W_{ad} = 2 \left( \sqrt{\gamma_{solute}^d \gamma_{solvent}^d} + \sqrt{\gamma_{solute}^p \gamma_{solvent}^p} \right) \quad (2.3)$$

$$\gamma = \gamma^d + \gamma^p \quad (2.4)$$

For a non-polar solute, the dispersion component is dominant ( $\gamma^d \gg \gamma^p$ ); for water, the dispersive and polar components have similar magnitudes. We derived Equation (2.5) by splitting the  $\gamma^d$  and  $\gamma^p$  components of solute and solvent in Equation (2.2). The mismatch (Equation (2.5)) of dispersive and polar components between the solute and solvent gives rise to large unfavorable interfacial tensions, thereby creating the solvophobic effect.

$$\gamma_{interface} = \left( \sqrt{\gamma_{solute}^d} - \sqrt{\gamma_{solvent}^d} \right)^2 + \left( \sqrt{\gamma_{solute}^p} - \sqrt{\gamma_{solvent}^p} \right)^2 \quad (2.5)$$

This relationship describes the chemical basis of unfavorable interfacial energy. Although the effective interfacial tension is influenced by the interfacial curvature on the scale of the Tolman length, as we shall discuss later, a smooth macroscopic interfaces can be effectively treated as planar. In this phenomenological framework, interfacial tension is a measure of the chemical compatibility between the solvent and solute, implying that the hydrophobic effect is essentially a solvophobic effect in water. However, the unusual physical properties of water and the anomalous behavior of hydration thermodynamics of small non-polar molecules indicate that water is significantly different from other solvents and that the phenomenological model does not apply for such molecules.

At what length does a macroscopic interfacial description begin to fail? Variations in the definition of solute-water interface location by a few angstroms have little influence on  $\Delta G^{hyd}$  of macroscopic objects, but has large effect on the interfacial area of nanometer sized solutes. However, interface definition on the microscopic scale is fuzzy: a methane-sized particle has a solvent-accessible surface area (SASA) defined by a sphere of 3.3 Å radius, whereas the van der Waal surface is defined by a sphere of 1.9 Å [5], resulting in an area 3 times smaller. Ashbaugh and Pratt suggested an optimal surface between the hard-sphere surface and the solvent-accessible surface that makes surface tension size independent [5]. However, whether this definition is generally applicable to complex geometries and surface chemistry is yet to be investigated. Wagoner et al. investigated the proportionality between  $\Delta G^{hyd}$  and the SASA on molecular length scale and found that the SASA failed to discriminate the different conformation states of non-polar solutes, which leads to inaccurate assessment of the hydrophobic interaction strength [171]. As we shall outline next,  $\Delta G^{hyd}$  at small length scale is better described by a volume scaling relationship.

## 2.2 Small molecule hydration anomalies

In 1979, Tanford showed that macroscopic interfacial tension failed to explain the significantly lower hydration  $\Delta G$  of small non-polar molecules such as methane [165]. However, the discrepancy cannot be accounted for by redefining a smaller molecular surface. The temperature dependence of small molecule hydration  $\Delta G$  is qualitatively different than that for macroscopic interfacial hydration, which suggests different hydration mechanisms. The macroscopic interfacial tension between water and a non-polar solute monotonically decreases as temperature increases (Figure 2.1a). The hydration  $\Delta G$  of a small non-polar molecule increases with temperature to a maximum then decreases (Figure 2.1b), distinguishing it from macroscopic hydration. For small molecules, the

increasing hydration  $\Delta G$  is associated with negative hydration entropy,  $S = -(dG/dT)_p$ , which has traditionally been associated with formation of ordered clathrate-like water structure around small non-polar solutes. In contrast, the temperature dependence of surface tension leads to positive hydration entropy upon forming a macroscopic interface. Experiments later found that although water molecules in the hydration shell have reduced conformational freedom, they do not form rigid clathrate structures [9, 144, 25, 22]. Above the turn-over temperature, the hydration entropy becomes positive, resembling macroscopic hydration. The turn-over temperature also strongly depends on the solute size; increasing the particle size lowers the turn-over temperature. This anomalous temperature and size dependence signify microscopic hydrophobic hydration. Theories predict a transition of the hydration physics from microscopic to macroscopic scales.

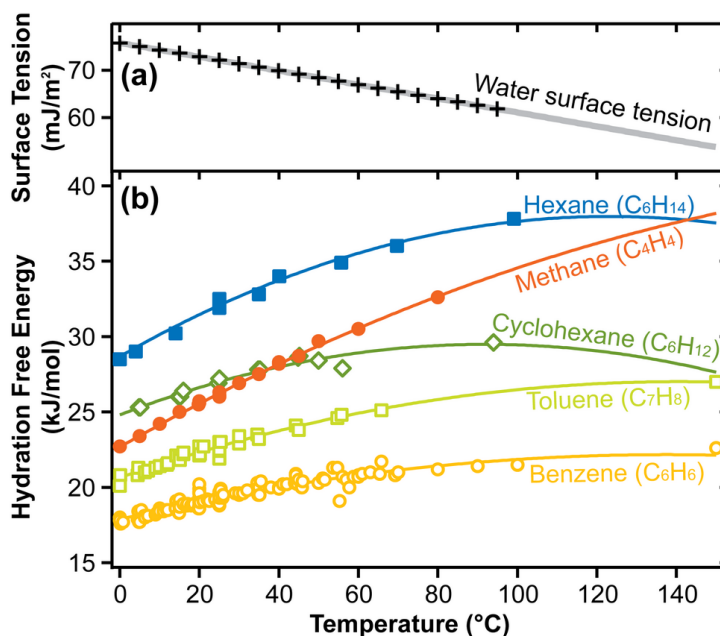


Figure 2.1: Temperature dependencies of (a) the surface tension of pure water and (b) the molar excess hydration  $\Delta G$  of small molecules calculated by  $\Delta G = -k_B T \ln(x)$ , where  $x$  is the solubility in mole fractions [182]. The small molecule data are color-coded by their relative molecular volume: methane < benzene < toluene  $\approx$  cyclohexane < hexane.

## 2.3 Hydrophobic size effect

Small molecule hydration anomalies have been the focus of significant theoretical efforts including information theory [87, 84], a revised scaled particle theory [5], and the Lum-Chandler-Weeks theory of hydrophobicity [112, 32, 74].

An early attempt to explain the lower hydration  $\Delta G$  of small molecules applied a size-dependent curvature correction to the surface tension of water, giving rise to the Tolman length [169]. However, it failed to explain the temperature dependence of hydration  $\Delta G$ . The classic, scaled particle theory (SPT) also failed to predict this temperature dependence because it incorporated few molecular details of water. A revised SPT [163] incorporating experimental water structural information was able to cover length scales from molecular surface tension to the macroscopic surface tension [5, 58] and reproduce the turn-over behavior of small molecule hydration  $\Delta G$  and its size dependence, as well as the entropy convergence in small molecule hydrophobic hydration [5]. The Tolman length in the revised SPT has a temperature dependence that decreases from positive to negative, making it difficult to assign its physical meaning. For a methane-sized spherical solute, the predicted negative hydration entropy agrees with experimental results while the largely positive hydration enthalpy is the opposite of negative experimental values. In addition, the turn-over temperature of an inserted particle is lower than found experimentally. These discrepancies were attributed to the lack of solvent-solute attractions in the model [5].

Hummer and coworkers calculated the excess chemical potential  $\mu^{ex}$  of cavitation using an information theory (IT) approach [87, 84]. The probability density of observing water-free volumes of different sizes was used to calculate  $\mu^{ex}$ . The authors showed that the prediction from IT matches the results from the test particle insertion method. Using this theory, Garde and coworkers predicted negative hydration entropies for small non-polar molecules and the temperature dependence of their hydration  $\Delta G$ . IT offered a molecular explanation for the experimentally observed convergence of entropy for small molecules. Furthermore, IT indicated that a Gaussian distribution of the density fluctuations of water is sufficient to describe hydration phenomenon [87], which supported a Gaussian field theory [112].

Lum, Chandler and Weeks (LCW) developed this quantitative Gaussian mean-field theory that describes the size dependence of hydrophobicity from microscopic to macroscopic scale [112]. The unit area hydration  $\Delta G$  increases linearly with solute size up to  $\sim 1$  nm and asymptotically approaches the macroscopic interfacial tension as the particle size continues to increase (Figure 2.2a). The linear increase below 1 nm indicates an apparent volume dependence of hydration  $\Delta G$ , in agreement with the lower than SASA-predicted hydration  $\Delta G$  of small non-polar solutes. The driving force behind microscopic hydration thermodynamics in the volume-dependent regime is mainly entropic, which gradually transitions into mainly enthalpic when solute size increases to the area-dependent macroscopic regime [146]. Furthermore, Huang et al. demonstrated that the

thermal signature of hydrophobic hydration can be reproduced using the LCW theory, which is also strongly size dependent (Figure 2.2b) [74]. The temperature at hydration  $\Delta G$  turn-over decreases as the particle size increases. For particles larger than 1 nm, a monotonically decreasing hydration  $\Delta G$  is observed, consistent with macroscopic surface tension. By studying the density fluctuations of water near hydrophobic particles using the LCW theory, the Garde group has made significant advances in understanding hydrophobicity in polymers [7] and at interfaces [91]. In particular, they showed that the hydration  $\Delta G$  of a homopolymer with 25 methane-sized repeats also exhibits turn-over behavior similar to that of small molecules [7].

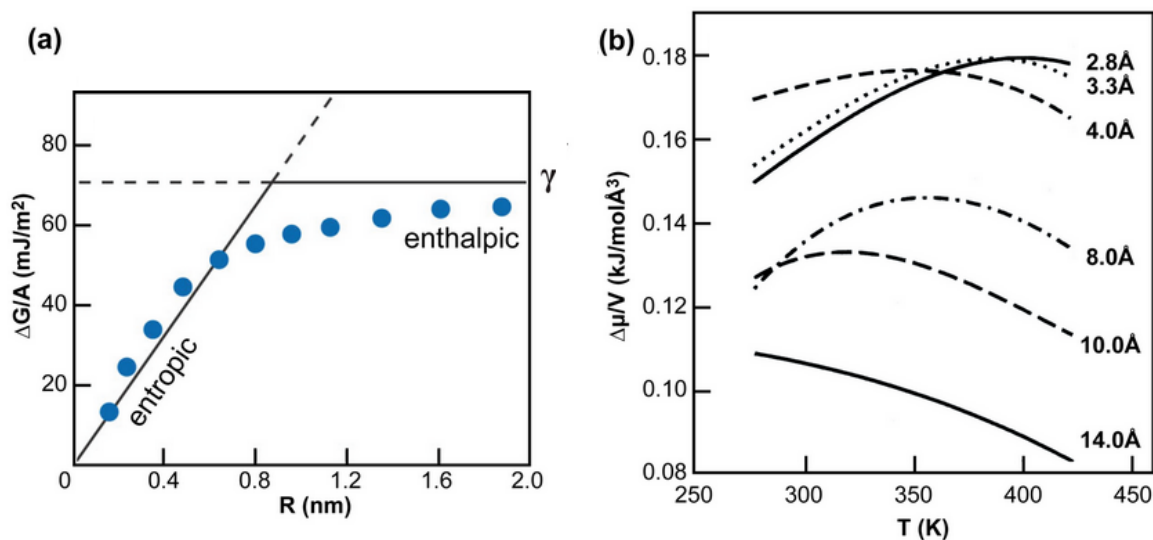


Figure 2.2: Theoretical predictions of free energy as a function of size and temperature. (a) LCW theory prediction of hydration  $\Delta G$  per unit area as a function of solute radius (adapted from Chandler [32].) (b) The temperature dependence of hydration  $\Delta G$  for various particle sizes (adapted from Huang et al. [74].)

Theories have assumed that the hydration  $\Delta G$  of small molecules computed from their solubility data can be used to calculate macromolecular thermodynamics. Furthermore, the view that the hydrophobic core of a folded protein behaves like a bath of non-polar molecules is challenged. Hydrophobic homopolymers with hundreds of repeating units are insoluble, which has previously necessitated these assumptions. Our understanding of hydrophobic interactions in polymer systems are limited by experimental evidence.

Therefore, experiments that directly probe the energy of hydrophobic collapse in a polymer are needed. In this thesis, the mechanical unfolding studies of a hydrophobic polymer in both theoretical and experimental aspects address the following questions:

- Experimental

- How can one perform experiments that unfolds a single hydrophobic polymer
- What is the signature to unfold a single hydrophobic polymer?
- How is  $\Delta G^{hyd}$  difference between collapsed and extended state calculated from experiments?
- Theoretical
  - How is the hydration behavior of a single polymer affected by solvent condition?
  - How is the hydration behavior of a single polymer affected by temperature?
  - How does the size of side-chains affect this temperature dependency?
  - Does polymer hydrophobic hydration follow macroscopic or microscopic hydration physics?

## Chapter 3

# Single Molecule Force Spectroscopy by Atomic Force Spectroscopy

Invented in 1986 by Binnig, Quate and Gerber [18], the Atomic Force Microscopy (AFM) (Figure 3.1) has become one of the most versatile tools for studying the structures and functions of nanoscopic systems. Improvements to the AFM and emerging techniques enable researchers to examine mechanical, chemical, electronic, and magnetic properties of materials.

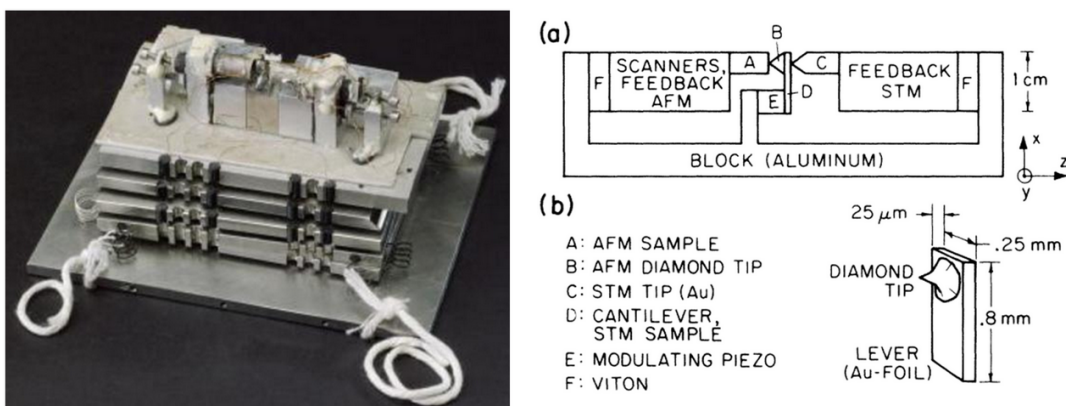


Figure 3.1: The first AFM invented by Binnig, Quate and Gerber in 1986. (Figure adapted from Binnig et al. [18].) Instead of using the laser as the position detector, it uses a STM for detecting the cantilever deflection.

One important AFM technique is the Single Molecule Force Spectroscopy (SMFS) [134, 129], which made it possible to study the conformational changes of a single molecule under mechanical perturbation. Studying the behavior of a single molecule allows one to see its dynamics rather than the ensemble average from bulk experiments. In addition, the conformation of single molecule can be individually manipulated beyond what bulk

experiments could achieve. This offers a unique opportunity to study macromolecules such as proteins, DNAs, RNAs and synthetic polymers.

With piconewton force sensitivity and sub-nanometer spatial accuracy, single molecule force spectroscopy has been widely used to study the mechanical unfolding of proteins [28, 73, 152, 97, 150] and RNAs [130, 70], the stretching and unzipping of DNAs [160, 113], the unbinding between receptor and ligand [107, 46, 119], interactions between proteins [124, 27, 95, 126], and the conformational changes of small molecules [127] and polymers [175, 151, 105, 106, 104, 103, 93, 108, 60, 168]. These experiments provide insights into the conformational changes of a single molecule and the energies associated with each conformational state [89, 63, 42]. This chapter begins by describing the working principle of the atomic force microscopy and how it is applied to single molecule force spectroscopy. Technical aspects that are necessary for accurate force measurements will be addressed, including the cantilever calibration, noise reduction, environment control, drift correction, and contamination control.

### 3.1 Principles of Atomic Force Microscopy

AFM works by sensing forces subjected to a microscopic cantilever (Figure 3.2), which deflects under load like an ideal spring. The spring constant of a cantilever can be tuned by its material and dimensions, depending on the application: longer, narrower and thinner cantilevers have lower spring constant and are good for sensing low forces such as those from a single molecule; other cantilevers may be tuned to be stiffer and have specific oscillatory resonances that can be used for tapping mode imaging for surface topography.

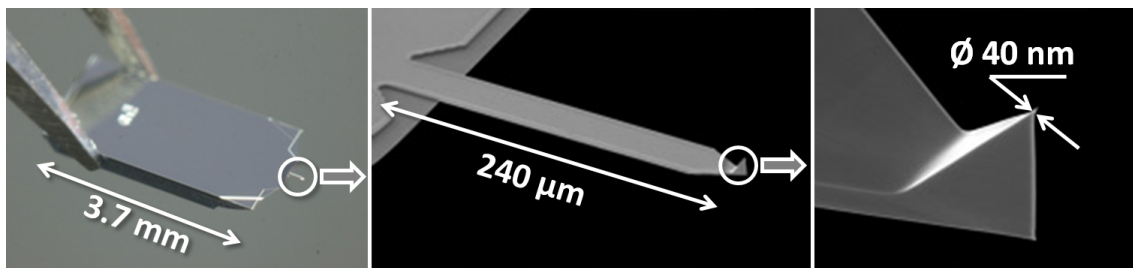


Figure 3.2: Zooming into the tip of an AFM cantilever. Left: an AFM cantilever mounted on a silicon chip being handled by tweezers. Middle: zooming into the cantilever. Right: zooming into the tip of the cantilever; the tip apex typical of tens of nanometers curvature is where the interactions occur. (Individual figures adapted from Olympus Micro Cantilever product sheet [136].)

In order to detect miniscule deflection from forces as low as a few pico-Newtons

(pN), the very first AFM used Scan Tunneling Microscopy (STM) on the backside of the cantilever to detect its movement (Figure 3.1). Such detection scheme has been replaced by a more versatile and reliable method using a laser. Modern AFM focuses a laser beam to the backside of the cantilever, where it is reflected onto a photodiode divided into quadrants (Figure 3.3). At resting position, the laser spot is calibrated to the center of the photodiode such that the voltages across the high speed photodiodes are identical (Figure 3.3A). Any deflection of the cantilever causes the reflected laser spot to deviate from the center, thus creating voltage differences across the photodiodes (Figure 3.3B). This voltage change can be calibrated to provide the cantilever deflection, and subsequently, the magnitude of the force causing such deflection.

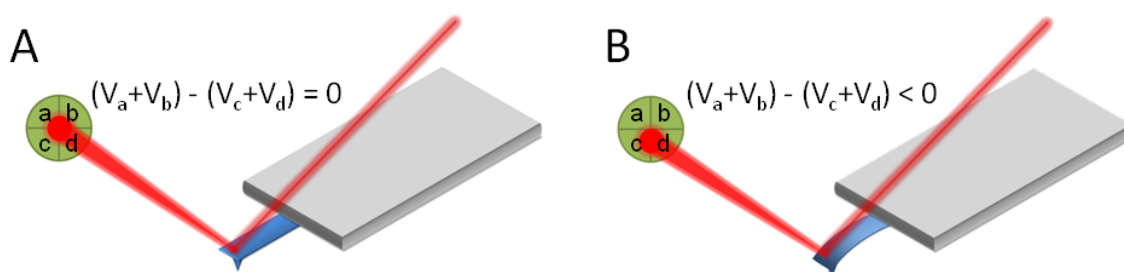


Figure 3.3: Cantilever deflection causing photodiode voltage differences. A. Cantilever in neutral position. B. Cantilever subjected to force.  $V_a$ ,  $V_b$ ,  $V_c$ , and  $V_d$  are the voltages from each quadrant of the photodiode.

AFMs achieve sub-nanometer spatial resolutions by piezoelectric actuators. The piezoelectric actuator linearly and reversibly deforms with an applied voltage, making it possible to precisely control linear displacements. With piezoelectric actuators in all three X, Y and Z axis, the AFM tip can move to an arbitrary location with respect to the substrate. This makes it possible to raster scan the surface and to obtain topographical information in both contact and tapping modes. The contact mode is achieved through a feedback mechanism that controls the Z-position of the tip such that a constant cantilever deflection is achieved (Figure 3.4). By raster-scanning the surface while keeping the cantilever deflection constant, the Z-position of the tip closely follows the topography of the surface. Alternatively, in tapping mode, the cantilever is mechanically excited to oscillate at its first harmonic resonance frequency. The amplitude of the oscillation is closely related to the proximity of the tip to the surface and the phase of the oscillation is related to the visco-elastic response of the local substrate. Hence, by keeping the amplitude constant via the feedback mechanism, the topography information can be obtained. At the same time, the phase image maps the visco-elastic response of the sample, providing additional information to complement the topography.

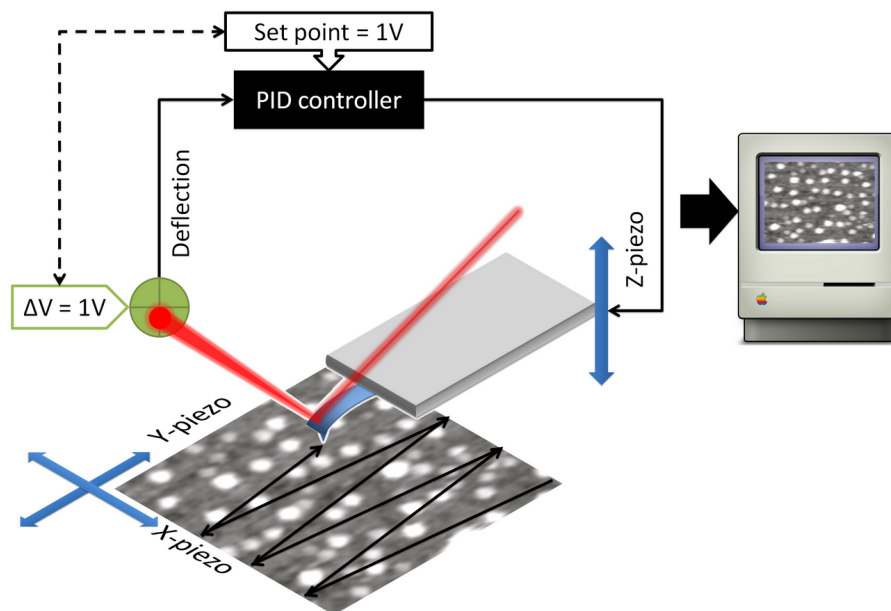


Figure 3.4: Surface-scanning mode of AFM. A proportional-integral-differential (PID) feedback controller adjusts the Z-position such that the cantilever deflection is constantly kept at the set point while raster scanning the surface.

## 3.2 Using AFM for single molecule force spectroscopy

Single molecule force spectroscopy is another major AFM technique. A macromolecule is tethered between the tip apex and the substrate via specific chemical interactions or non-specific physical adsorption (Figure 3.5). As the tip is pulled away from the surface, the tethered molecule exerts mechanical force on the AFM cantilever; the resisting force from the molecule is recorded as a function of the tip-surface distance, which correspond to the end-to-end extension of the tethered molecule (Figure 3.5). This force-extension curve is commonly referred to as a force curve. These force curves usually provide information on the mechanism and energy of the molecular events during the pulling process [89, 42, 67].

Different molecular events exhibit different force-curve signatures. For instance, the mechanical unfolding of multi-domain globular proteins show saw-tooth patterns with identical gaps [28, 150]; each rupture in the force-curve indicates the unfolding of one domain along the chain [28, 150]. The rupture of a single receptor-ligand bond is reflected from the single rupture events at the total contour length of the attaching tethers [46, 148]. The unraveling of a randomly structured hydrophobic polymer shows a plateau in the force-curve, indicating a hydrophobic hydration event (Figure 3.5) [105, 106, 60, 168].

One can learn more about the molecular processes by varying the conditions of these pulling experiments. In dynamic force spectroscopy, different pulling velocities were

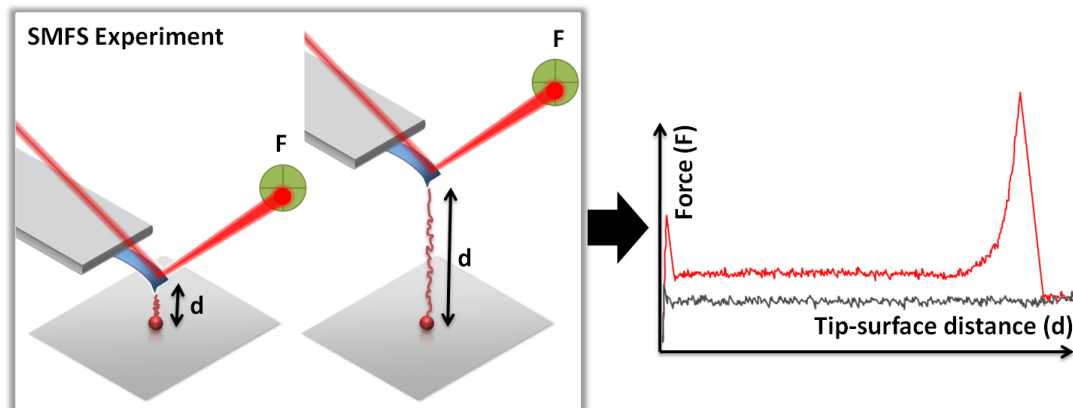


Figure 3.5: Single molecule force spectroscopy by AFM showing a single hydrophobic polymer pulled against its equilibrium, collapsed conformation. The force vs. tip-surface distance curves are recorded for such event. More details on the mechanism of this particular system will be provided in the subsequent chapters.

used to unfold the protein in non-equilibrium conditions. By applying the Jarzynski equality[94], these non-equilibrium measurements provide information to extract the thermodynamics properties of the protein in its equilibrium state [42, 67, 122]. By varying the environmental conditions such as solvent, osmolytes, temperature, one can dissect the molecular interaction energy to find contributions from electrostatics, hydrophobicity, and solvent reorganization entropy.

### 3.2.1 Strategies for tethering a single molecule

The ability to tether only one molecule between the AFM tip and the substrate is vital to single molecule force spectroscopy. To ensure that the AFM tip statistically interacts with at most maximal one molecule at a time, the target macromolecule must be sparsely deposited or tethered on the surface. This can be done by immersing the substrate in a solution of the target molecule and allowing target molecules to physically adsorb onto the substrate. A typical AFM tip has radius of curvature about 20 nm, therefore, the average distance separating any two surface bound molecules should be at least 40 nm. The sample preparation technique to achieve such sparseness varies from sample to sample, and is generally affected by the following factors:

- The surface charge, hydrophobicity, and specific chemical groups
- Concentration of the target molecule
- Method used and duration allowed for the adsorption

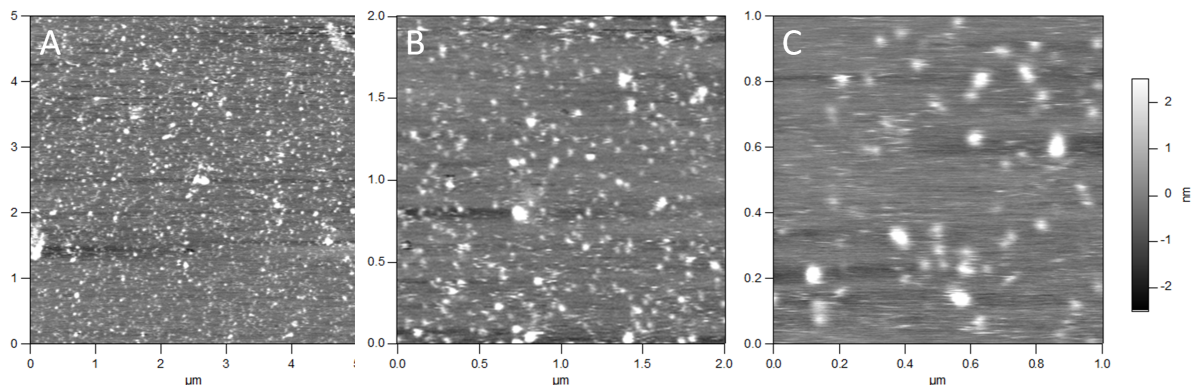


Figure 3.6: An AFM image of surface deposited fibronectin molecules in aqueous solution at A. 5  $\mu\text{m}$ , B. 2  $\mu\text{m}$ , and C. 1  $\mu\text{m}$  scan size. Individual bright dot may be a monomer, dimer, or aggregates of multiple fibronectin molecules.

The target molecule density after deposition can be checked by an AFM topography scan. Figure 3.6 shows a contact mode scan of the full-length human fibronectin protein (a fairly large multi-domain protein composed of 9 type I, 2 type II, and 15 type III domains) deposited on mica surface, each bright dot shows a monomer, a dimer, or an aggregate of multiple fibronectin molecules. Due to protein degradation and aggregation, the size of individual dot varies. When scanning with too much contact force, the tip can push around the un-tethered, physically adsorbed molecules to form aggregates. Figure 3.7 shows an area with tip-induced aggregation after a hard scan, the surrounding area is unaffected by a subsequent gentle scan.

Alternative to physisorption, one can graft the target molecule to gold surface via gold-thiol bond. The sparse grafting can be achieved either by carefully controlling the concentration and duration of the adsorption, or by only allowing the target molecules to attach to gold surface exposed by defect sites of a protective self-assembled monolayer [192]. The grafting density can be conveniently controlled by the number of defects on the substrate [192].

Single molecule experiments are performed by positioning the AFM tip to the location if a single molecule from a prior surface topography scan. Figure 3.8 shows that pulling events correlates to the locations of physically adsorbed molecules as seen from prior AFM scans.

Two general strategies to catch target molecules with the AFM tip are chemisorption and physisorption (Figure 3.9). Chemisorption (or chemical adsorption) utilizes the chemical interactions between molecules with high specificity and affinity, such as the biotin-streptavidin and the  $\text{Ni}^{2+}$ -histag systems. The AFM tip can be functionalized

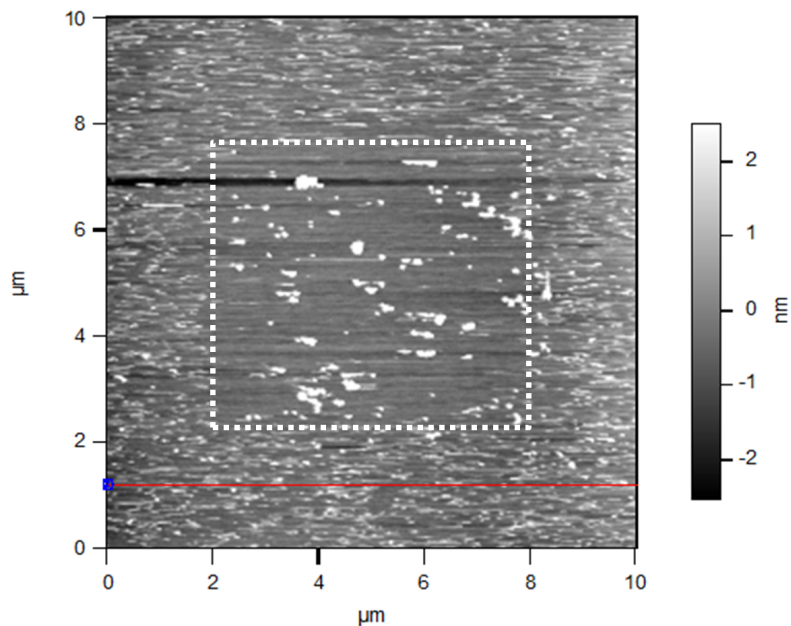


Figure 3.7: A contact mode scan with the tip pushing hard onto the surface inside the dotted square caused surface bound molecules to aggregate. The aggregates are generally much taller and larger than others. The current AFM image zooming out from the previous scan is scanned with a much lower force.

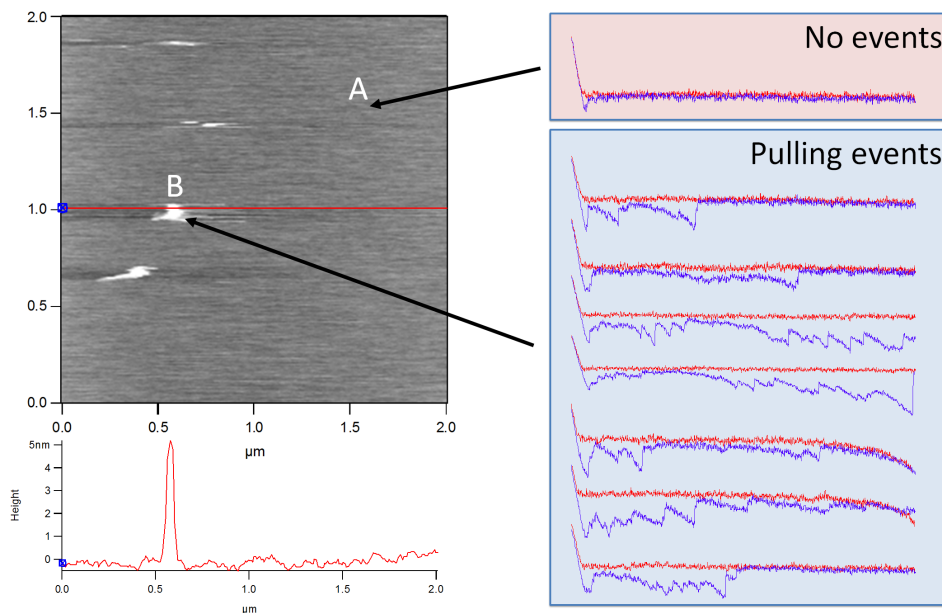


Figure 3.8: Pulling events are correlated to the locations of surface bound molecules. Where there is no surface bound molecule in the image (A), no molecular events were detected. On the other hand, pulling events are detected at location B, where there seems to be something on the surface. In this case, location B is most likely an aggregate of fibronectin molecules.

with streptavidin while the target molecule is labeled with biotin (Figure 3.9A). This allows the AFM tip to specifically attach to the labeled site of the target molecule, which improves the similarities between the pulling geometries of the target molecule. Physisorption utilizes the non-specific physical adsorption of target molecules onto the tip surface via van der Waals interaction (Figure 3.9B).

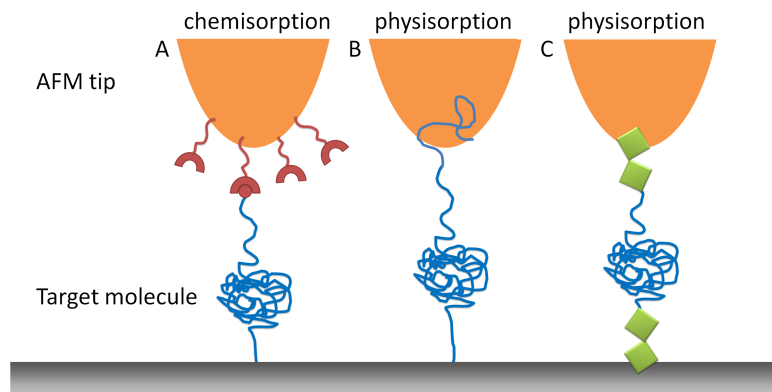


Figure 3.9: Strategies to attach a single molecule to the AFM tip. A, via specific ligand-receptor binding. B, via non-specific physisorption. C, via physisorption through tethering molecules.

The specificity and affinity of chemisorption allows one capture target molecules more easily and manage the location on the molecule where mechanical force is subjected to. However, the functionalized tip may introduce undesired additional interactions with the target molecule. In addition, the adding the affinity tag often requires modification of the target molecule that may have large effect on its structure and function. Physisorption, on the other hand, does not suffer from the above issues. However, the probability to capture the target molecule may be lower than chemisorption. To resolve the specificity issue with physisorption, multi-domain proteins have been used with the target protein sandwiched in the middle. In this case, only the flanking proteins will be non-specifically adsorbed onto the tip, serving both as a tether and as a single molecule marker [188] (Figure 3.9C). With this strategy, target protein does not need to be modified or labeled, placing it in a more native state.

### 3.2.2 Comparison between force spectroscopy techniques

A comparison of AFM and other force spectroscopy techniques is shown in Table 3.1. Due to the relatively small size of the AFM tip (on the order of tens of nanometers), the AFM can perform high resolution imaging as well as single molecule pulling, which adds spatial specificity to pulling experiments that other techniques lack. However, due to

the instrument arrangements, the AFM is only useful for pulling in one direction. In contrast, optical tweezer has the advantage of 3D manipulation and magnetic trap has the advantage to probe torsion [129]. The unfolding forces of polymers and proteins range from 10 to 500 pN; therefore, AFM is the best choice for this type of experiment. Other techniques such as optical / magnetic trap cannot easily reach such high forces. However, the high force limit comes at a cost of lower force sensitivity comparing to the other techniques. This comes from the relatively high spring constant and the relatively large size of the cantilever. An additional drawback of AFM is the relatively high cost of the micro cantilever. Furthermore, when a tip is contaminated, replacing it in the middle of an experiment is difficult. However, there are a number of techniques that can help decontaminate the AFM tip as we shall discuss in Section 3.8.

Parameters	AFM	Optical Tweezers	Magnetic Tweezers
Spatial resolution (nm)	0.5–1	0.1–2	5–10
Temporal resolution (ms)	1	0.1	10–100
Trap stiffness (pN/mm)	>5	0.005–1	$10^{-3}$ – $10^{-6}$
Force range (pN)	>10	0.1–100	$10^{-3}$ –100
Probe size (m)	100–250	0.25–5	0.5–5
Features	High force	3D manipulation	Torsion
Limitations	Low sensitivity	Photo damage	Hysteresis

Table 3.1: Comparison of single molecule force spectroscopy techniques (Table adapted from Neuman and Nagy [129].)

### 3.3 Cantilever calibrations

The calibration of the AFM cantilever is the most important step toward consistent and quantitative force spectroscopy measurements. Two parameters of the cantilever need to be calibrated: its optical sensitivity and its spring constant. Although the spring constant value of commercial cantilever is usually provided, they only reflect the average value of the batch; individual cantilevers may have spring constant variation as large as  $\pm 50\%$ . Therefore, the spring constant of each cantilever must be calibrated prior to experiment.

#### 3.3.1 Preparation of calibration substrate

In general, the requirement for tip cleanliness is much higher for single molecule force spectroscopy than for imaging. It is crucial to keep the tip free of organic materials

prior to the experiment. Freshly cleave a mica substrate by household Scotch tape gives a clean, stiff, and flat substrate, ideal for calibrating the cantilever. However, freshly cleaved mica is usually highly charged, which often makes it difficult to calibrate softer cantilevers as the electrostatic interactions bends the cantilever so much that the laser reflection is off scale. Alternatively, silicon (Si) wafer can be used for the substrate, which can be cleaned in “piranha” solution (3:1 of 98% sulfuric acid to 30% hydrogen peroxide) for approximately 30 minutes. This procedure removes organic materials on the Si surface from handling and prior exposure. After the piranha treatment, the substrate is washed with copious amount of deionized, filtered water and is blown dry with nitrogen gas. Si substrates prepared this way are free of surface charges, which make it much easier for soft AFM cantilevers to approach.

### 3.3.2 Calibration of cantilever sensitivity

The optical sensitivity of the cantilever (also known as inverse optical lever sensitivity, or *invOLS*) is the measure of the cantilever deflection ( $\Delta d$ ) over the photodiode voltage difference ( $\Delta V$ ), in the unit of nm/V:

$$invOLS = \frac{\Delta d}{\Delta V} \quad (3.1)$$

The value of  $\Delta V$  is directly measured from the photodiode; however, the value of  $\Delta d$  can only be indirectly measured. In AFM, the sensitivities of piezoelectric actuators (the distance it travels given an applied voltage) are usually well calibrated by the manufacture. In addition, the linear variable differential transformer (LVDT) sensors built inside these actuators provides additional calibration of the real translation distance. Therefore, the displacement of the z-piezoelectric actuator is used to measure the physical deflection of the cantilever  $\Delta d$ . This is achieved by pushing the cantilever onto a hard surface such that the deflection of the cantilever equals the distance travelled by the Z-piezoelectric actuator. By plotting the photodiode voltage as a function of the Z-piezo distance, the slope of the linear indentation portion of the curve gives the *invOLS* value (Figure 3.10A). Once the *invOLS* is obtained, the deflection of the cantilever can be directly calculated by Equation (3.1). More details on conditioning the data for *invOLS* correction is described in Section 6.2.

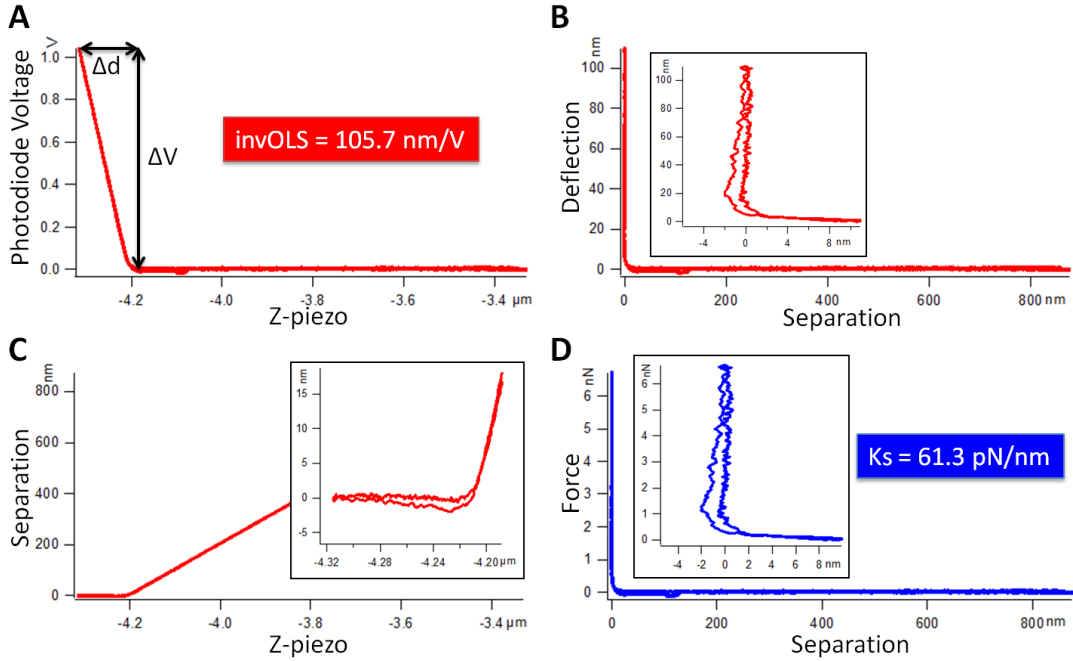


Figure 3.10: AFM cantilever calibration. A. Calibrating cantilever invOLS. B. Calculated cantilever deflection over tip-sample separation. C. Tip-sample separation vs.  $Z$ -piezo. D. Converting deflection to force gives the force-extension curve.

### 3.3.3 Calibration of cantilever spring constant

A thermal method developed by Hutter and Bechhoefer [90] was used to calibrate all cantilevers used in my studies. The AFM cantilever can be thought of as a one dimensional harmonic oscillator, which by the equipartition theorem would have energy of  $k_B T/2$ :

$$\frac{1}{2}k_s x^2 = \frac{1}{2}k_B T \quad (3.2)$$

where  $k_s$  is the cantilever's spring constant,  $x$  is the cantilever deflection,  $k_B$  is boltzman's constant, and  $T$  is temperature. Therefore, the spring constant of the cantilever is simply related to the expected value of the square of the deflection fluctuation:

$$k_s = k_B T / \langle x^2 \rangle \quad (3.3)$$

However, the signal fluctuation at the photodiode contains contributions from other noise sources including low frequency mechanical noise transmitted from the building, acoustic noise, electronic noise from the photodiode, and higher harmonics of the cantilever, which makes it inaccurate to assess the cantilever spring constant by directly using  $\langle x^2 \rangle$  at the photodiode. To solve this problem, one can take a Fourier transform of the signal arriving at the photodiode to obtain the power spectrum, which helps to

isolate cantilever's thermal fluctuation from other background noise (Figure 3.11A).

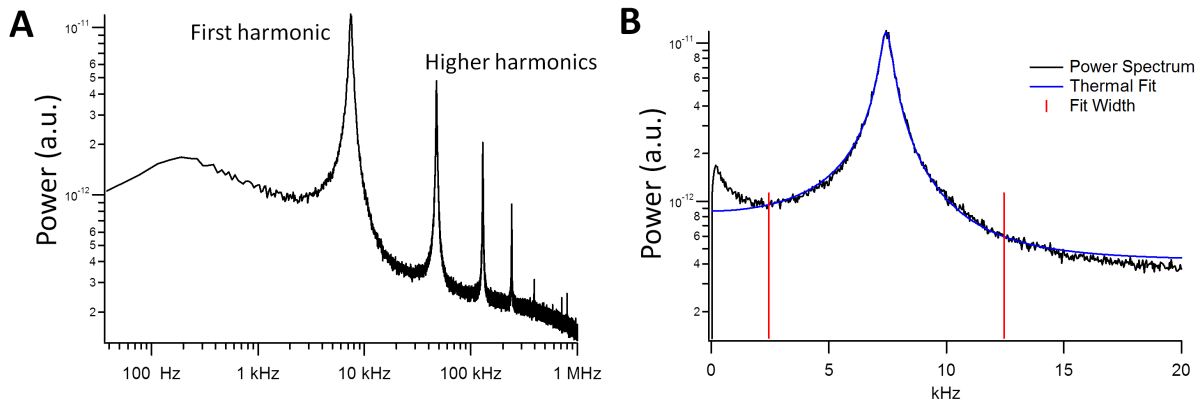


Figure 3.11: Power spectra of an AFM cantilever. A. Power spectrum showing the first and higher harmonic peaks on top of the  $1/f$  noise floor. B. Lorentzian fit (blue) to the first tip oscillation harmonic peak (black), the fit boundary is marked by the red markers.

The power spectrum of the resting cantilever shows a number of peaks corresponding to the first and higher harmonics of the cantilever's vibration modes. The largest and first harmonic mode corresponds to the bending mode of the cantilever where the harmonic potential is characterized by the spring constant. Therefore, the area under the first harmonic peak is the  $\langle x^2 \rangle$  due to only thermal excitation [90]. By first removing the  $1/f$  background noise, one can obtain the area under only the first harmonic peak by a Lorentzian fit.

### 3.4 Force-extension curves

With the cantilever's optical sensitivity and spring constant calibrated, all distance and force information can be related to each other (Figure 3.12). Of particular interest is the tip-surface distance, which equals the end-to-end extension of any tethered molecules between the tip and surface. The following relations are used to compute the time-series of each data stream.

$$\Delta d(t) = \text{invOLS} \times \Delta V(t) \quad (3.4)$$

$$F(t) = k_s \times \Delta d(t) \quad (3.5)$$

$$d_{ee}(t) = Z(t) - \Delta d(t) \quad (3.6)$$

where  $F(t)$  is the calculated force on the cantilever,  $d_{ee}(t)$  is the end-to-end extension,  $Z(t)$  is the distance Z-piezo traveled. Because all time-series data are sampled at identical intervals, they can be directly plotted against each other. Plotting  $F(t)$  against  $d_{ee}(t)$  gives the force-extension curves (Figure 3.10D). It is necessary to check after calibration, whether the indentation portion of the force curves are strictly vertical on a hard substrate. Any deviations from vertical indicate the invOLS has drifted and recalibration is required.

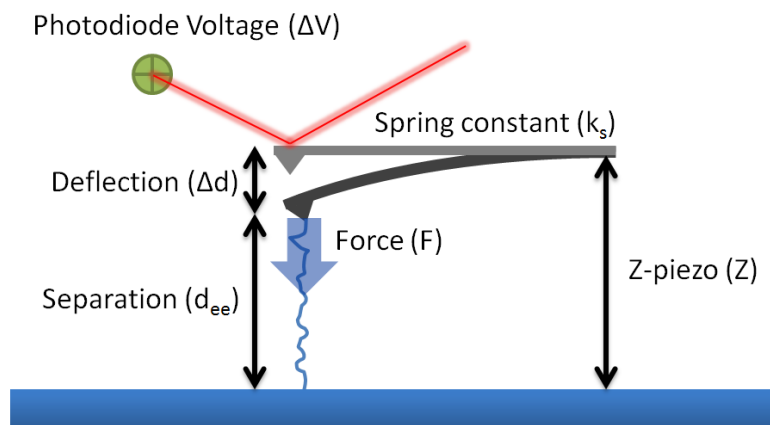


Figure 3.12: Relationships between various measured and calculated parameters in an AFM.

## 3.5 Mechanical noise control

As AFM is sensitive to forces as low as pN, external mechanical noise can be easily picked up by the cantilever. Therefore, mechanical decoupling the AFM from its environment is critical. Sources of noise and strategies for improvements are discussed here.

### 3.5.1 Acoustic noise

Sound waves travel in media as pressure waves, which can couple to the AFM cantilever. Acoustic noise is especially problematic for single molecule force spectroscopy experiments because the softer cantilevers pick up acoustic noise more easily. An acoustic enclosure with noise reduction of at least 30 to 40 db is necessary to improve signal-to-noise ratio of single molecule force spectroscopy experiments [69] (Figure 3.13).

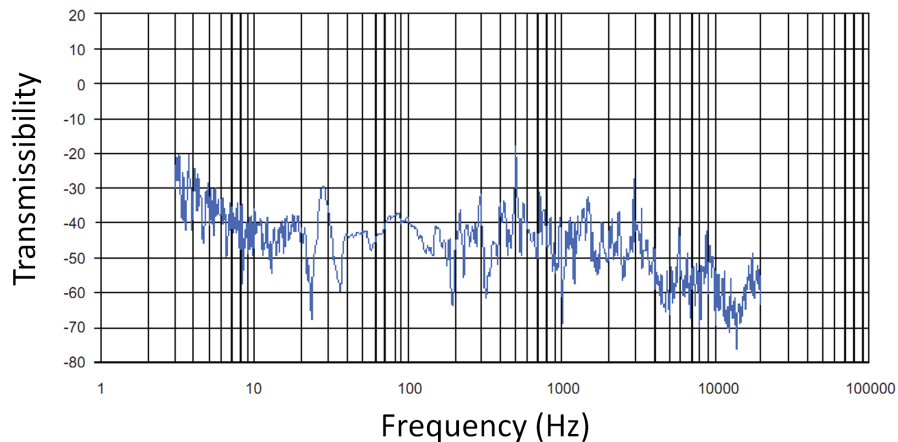


Figure 3.13: Transmissibility spectrum of the AFM acoustic isolation enclosure (Figure adapted from Herzan AEK-2002 acoustic enclosure datasheet [69]).

### 3.5.2 Floor vibration noise

The most prominent source of noise is the mechanical vibration transmitted through the floor. Vibrations from walking, door opening and closing, outside construction, air conditioning, computer fan, and building's intrinsic vibrations can all couple to the floor and be detected by the AFM. Vibration isolation table was used to decouple the microscope from the floor vibration. Figure 3.14 shows the transmissibility of a passive vibration isolation table, where floor vibration above 10 Hz is virtually eliminated from the microscope with over  $-50$  db transmissibility. The lower frequency vibrations can be reduced by active vibration isolation. Similar to the noise-cancelling headphones, the vibration isolation table detects vibrations and immediately counteracts by generating a reversed waveform, cancelling the effect of the incoming vibration.

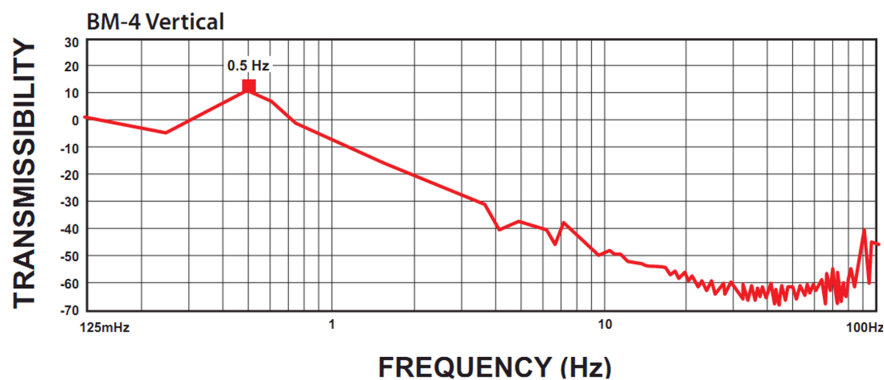


Figure 3.14: Transmissibility spectrum of a passive vibration isolation table. (Figure adapted from Minus K Technology BM-4 bench top vibration isolation platform datasheet [123].)

One can add another stage of damping to further reduce the transmitted vibration by placing the vibration isolation table above a heavy countertop; at the same time, place heavy duty rubber damping pads under the feet of the table (Figure 3.15). Given the same floor vibration, the large inertia of the countertop reduces the amplitude of the transmitted vibration. Floor vibration at various locations in the lab was surveyed, and the microscope was placed at the site with the minimal floor vibration level.

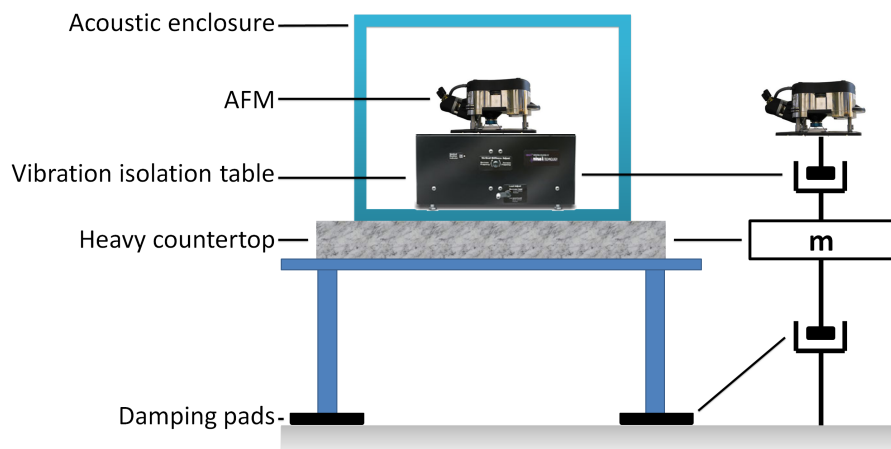


Figure 3.15: Two stage vibration isolation strategy. The first stage composes of a heavy mass such as a granite block and passive damping pads. The second stage is a commercial vibration isolation table, providing further noise reduction.

In addition to vibration transmitted through the floor, the data cable that connects the microscope directly to the controller also transmit significant amount of vibration. Gentle taps on the controller box can cause excessive noise clearly visible in both force curves and surface scans. For this reason, the controller was supported on sponges to minimize transmission of floor vibration to the controller. Vibration through the data cable can be damped by clamping it to something heavy but decoupled to any enclosure. A heavy cable clamp ( $\sim 10$  kg) with rubber footing was used for this purpose. Other non-essential cables (such as camera power and signal cable) connected to the microscope should be removed during force spectroscopy experiments.

### 3.5.3 Evaluation

The effectiveness of the vibration isolation methods were evaluated by engaging the microscope cantilever onto a substrate and detecting transmitted vibrations. The deflection of the cantilever is recorded over time, and the standard deviation of the deflection is used to evaluate the vibration isolation of the system (Figure 3.16). All experiments were done in air. The vibration levels were detected with the following setups:

- Open, no isolation: the acoustic enclosure was kept open to see the effect of acoustic noise and air turbulence on the system. In addition, the vibration isolation table is locked, meaning that it is letting floor vibration to come through.
- Closed, no isolation: the acoustic enclosure is closed but vibration isolation table is still locked.
- Closed, passive isolation: the acoustic enclosure is closed, and the vibration isolation table is passively damping higher frequency vibration.
- Closed, passive+active isolation: the acoustic enclosure is closed, and the active vibration isolation is turned on to remove low frequency vibrations.

The result shows that the combination of all vibration isolation strategies reduces mechanical vibration transmitted to the substrate by 80%.

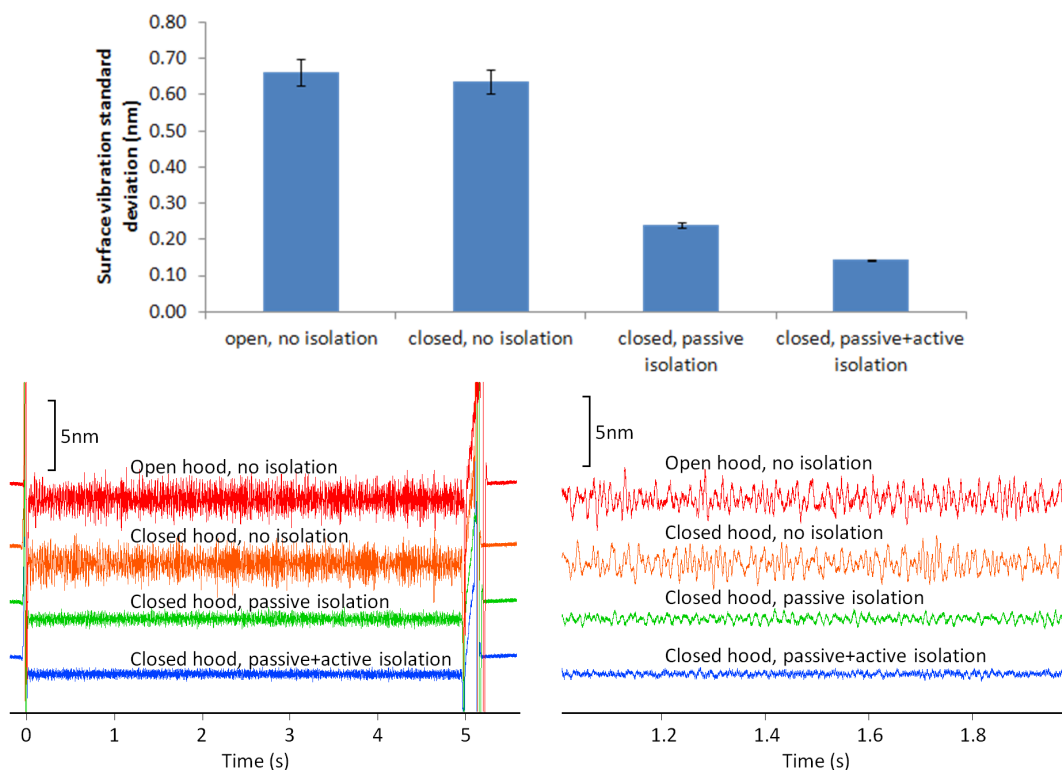


Figure 3.16: Effectiveness evaluation of acoustic hood, passive vibration isolation and active vibration isolation. Top graph shows the standard deviations of the vibration time trajectories in the bottom graphs.

## 3.6 Environment control

Aqueous environment were controlled by a closed fluid cell, which is mainly composed of a flexible membrane that seals the AFM cantilever inside the closed fluid cell dish where the sample and the AFM tip are immersed in aqueous solution (Figure 3.17). A circular heating element and a thermal couple tightly control the fluid temperature to  $0.05^{\circ}\text{C}$  accuracy through a feedback mechanism. Because the temperature control lacks cooling function, the controlled temperature ranges from  $\sim 5^{\circ}\text{C}$  above room temperature to  $80^{\circ}\text{C}$ . The additional  $5^{\circ}\text{C}$  above room temperature is due to heat released from the electronics within the AFM head. The maximal controlled temperature is set to  $80^{\circ}\text{C}$  as excessive bubble formation, convection current, and uneven heating that would severely affect the stability of the AFM above this temperature. The fluid inlet/outlet ports allow solvents and buffers to be exchanged without disengaging the AFM. The closed fluid cell also prevents solvent evaporation during long experiments, ensuring same solution concentration throughout the experiment.

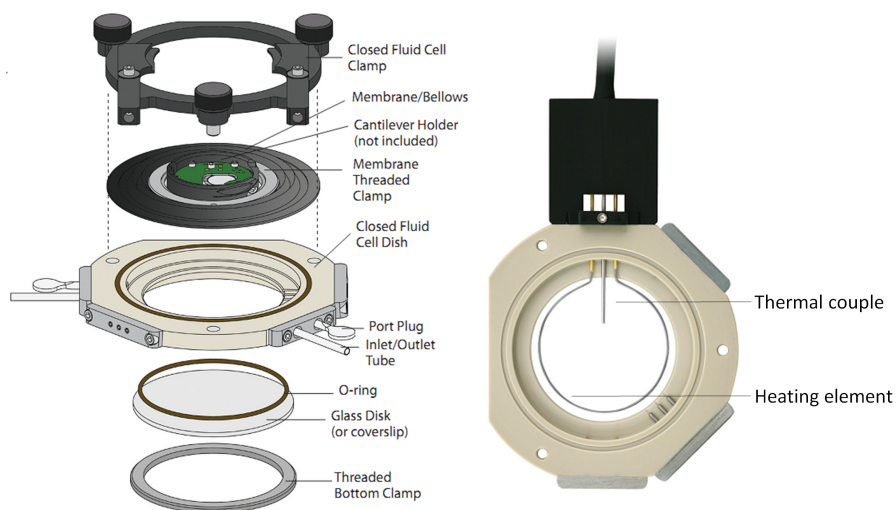


Figure 3.17: Closed fluid cell assembly. (Figure adapted from the closed fluid cell data sheet [6].)

## 3.7 Drift control

Mechanical and optical stability of the AFM is critical for consistent single molecule measurements. As single molecule events are rare, gathering enough statistics could take hours to complete. During the measurement, the system parameters such as cantilever

position and optical sensitivity will drift from their initial calibration values. Strategies were developed to minimize the impact of such drift on quantitative measurements.

### 3.7.1 Thermal drift

AFM cantilevers are usually made of Si or  $\text{Si}_3\text{N}_4$  with a backside coating of a thin layer of gold or aluminum to reflect the laser. Because the reflective layer and the cantilever itself have different thermal expansion coefficient, the composite structure bends in response to temperature changes. In general, the metallic layer has greater thermal expansion coefficient than the cantilever, hence the cantilever bends towards from the surface with raising temperature (Figure 3.18). Since the AFM can detect deflections of the cantilever in the nanometer range, it makes the AFM cantilever extremely sensitive to temperature. The temperature sensitivity also depends on the dimension and ultimately the spring constant of the cantilever. Softer cantilevers are more prone to thermal-induced instability than stiffer cantilevers. However, the intrinsic spring constant is relatively insensitive (approximately 0.3–0.5% [23, 173]) to temperature from 0 to 100°C (see Section 8.5.2). Cantilever's deflection drift causes shift in the baseline reference where the force should be zero (Figure 3.19), therefore, this drift is bad for long experiments such as a surface scan, force-clamp, fly-fishing, and even slow pulling experiments. Controlling the deflection drift is utmost important during an experiment.

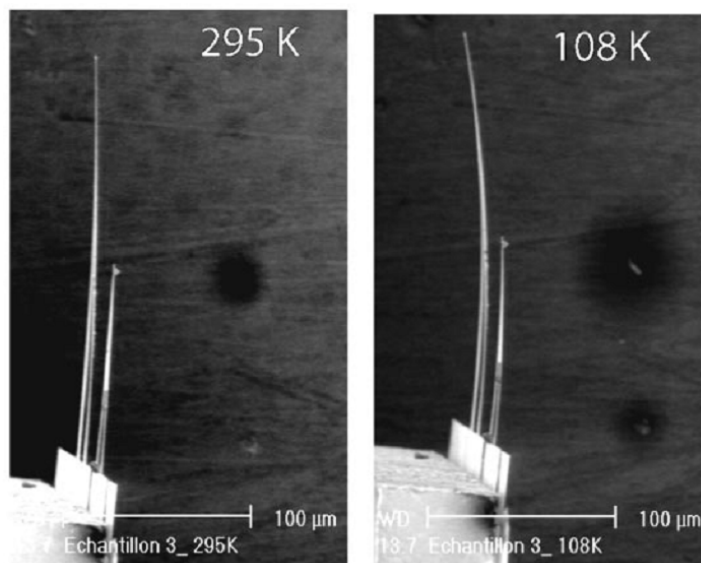


Figure 3.18: Temperature induced bending of the AFM cantilever. (Figure adapted from Radenovic et al. [145].)

Since the slow drifting environment temperature is the culprit for deflection drift,

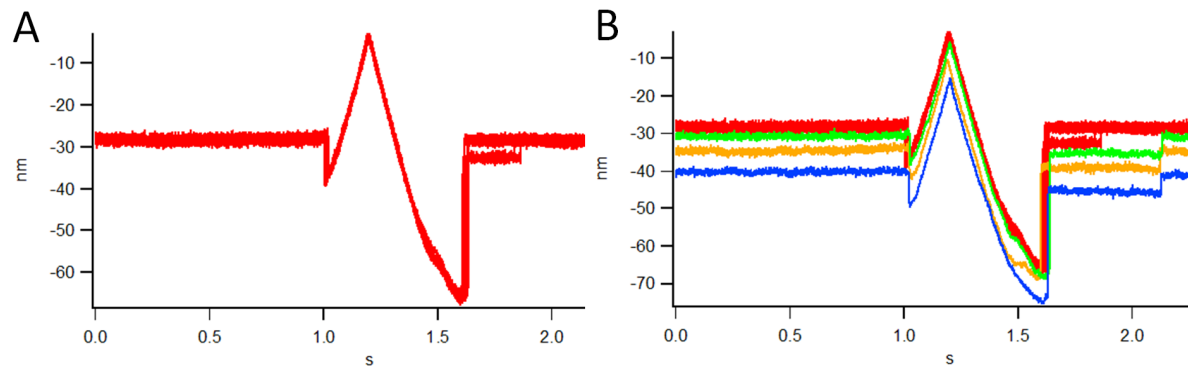


Figure 3.19: Cantilever deflection drift. The deflection vs. time graphs are shown. A. Overlapping of 5 adjacent deflection traces show relatively good overlap. B. Each color indicates a force curve collected 5 minutes apart, the deflection drifts to lower value over long period of time.

methods to minimize temperature changes can be adopted. Several sources of environment temperature instability include: variations in the room temperature (even in an environment controlled room), heat from electronics, evaporation of solvents, and the opening/closing of the acoustic enclosure. Therefore, allowing the system enough time (usually 30–60 minutes) to equilibrate before taking measurement is quite crucial. Although slow drifting temperature such as temperature differences throughout a day also influences the equilibrium temperature by up to  $0.5^{\circ}\text{C}$ , they do not affect individual force curves as much as the time scales differ significantly. To better control the environment temperature, the fluid cell can be used to actively maintain the temperature of the experiment via a temperature feedback mechanism (Section 3.6).

In addition to cantilever deflection drift, the relative position of the AFM cantilever to the substrate also drifts due to temperature variation in the system. Take the supporting legs of the AFM head for example: the 10 cm stainless steel legs have a thermal expansion coefficient of  $\sim 15 \times 10^{-6} \text{ 1/K}$ , meaning that every  $1^{\circ}\text{C}$  change in temperature will result in drift of  $1.5 \mu\text{m}$  in the vertical direction. This could impose a critical problem when performing slow pulling experiments where it takes minutes to complete one force curve. Therefore, again, it is crucial to give the system sufficient time to equilibrate before starting experiments.

### 3.7.2 Optical sensitivity drift

The sum value of the photodiode usually drops slightly over time, possible due to lower reflectivity of the cantilever. This affects the cantilever's optical sensitivity (invOLS). It is therefore a good practice to constantly check, and if necessary, recalibrate the invOLS

value during the experiment. The invOLS value could change as much as 20% in 24 hours, which would severely affect quantitative measurements of force if not corrected. Programs were made (Section 6.2) to automatically re-calibrate the invOLS value for individual force curves. For this reason, it is important that all force curves contain an indentation portion. In the case when fly-fishing mode is needed – i.e. cannot have hard indentations, one must frequently check the invOLS value of the cantilever.

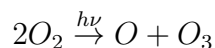
### 3.8 Contamination control

Contamination in single molecule experiments can cause unexpected results and lower the yield of useful force curves. Minimizing contamination at the sample preparation stage is crucial. Both the sample and the AFM tip should be thoroughly cleaned and kept clean at all time.

All materials from polymer to solvents used in single molecule experiments should be the highest purity grade from manufactures. All solvents should be filtered such that no particles interact with the sample. In addition, the chemical compatibility should be checked to ensure that containers are not dissolved by the solvent and thereby transferring unwanted polymers into the solvents.

Organic material is the main concern for our studies because the contaminants usually contain macromolecules, and could be confused with our target polymers and proteins. Flat surface produced from freshly cleaved mica is inherently clean and does not require further cleaning procedures. However, others such as silicon wafer and ultra-flat gold requires cleaning. In general, chemical cleaning using piranha solution (see Section 5.3.1) gets rid of all organic macromolecules on the surface. Surfaces prepared this way has no single molecule pulling signature at all, indicating they are generally clean enough for deposition of target macromolecules. Clean surfaces can be easily contaminated if left uncovered on the bench. To preserve a clean substrate, it is usually placed inside a clean Petri dish to avoid dust. In addition, the Petri dish is placed in a vacuum in a desiccator to minimize airborne molecules from adsorbing onto the surface.

The AFM tip is cleaned by shortwave UV light (100–280 nm wavelength) via the photosensitized oxidation process [99] for approximately 1 hour. The cantilever is placed with the tip-side facing up on a clean glass substrate under a UV light source. Organic molecules on the surface become excited after UV absorption and react with atomic oxygen created by the following reaction:



The products of such reaction are usually simpler gas molecules such as CO<sub>2</sub>, H<sub>2</sub>O and N<sub>2</sub> [99]. AFM tips cleaned with this protocol should be free of organic molecules and should be used as soon as possible.

Foreign contamination is undesirable. However, the AFM tip is considered contaminated when too many target molecules adsorb onto it. The following evidence may indicate tip contamination:

- Higher than normal frequency to see force curves with pulling events
- Force curves look similar regardless to the surface location
- Large surface adhesion force
- Breakthrough events during indentation
- Non-linear indentation curve
- Double-tip artifacts during surface scanning

A number of strategies to remove contamination without switching the tip have shown various degree of success:

- Surface scratching: First scan the surface and find an area of bare surface. Zoom into this area and rapidly scan the surface with contact mode at high set-point (or scan force) may scratch the contaminants off the surface.
- Water flow: Move the tip away from the surface and flush the fluid cell with buffer may sometimes wash off attached molecules due to shear flow.
- Vibration: It has been suggested that driving the tip at its resonance frequency with large oscillation amplitude may also help wash the attached molecule off from the tip. This method may work with tips for tapping mode in fluid, but may not work for soft cantilevers used in pulling experiments; these cantilevers are over-damped by water and may not show a strong first harmonic resonance peak.

### 3.9 Conclusion

AFM's sensitivity to force and distance enables manipulation and detection of a single molecule under mechanical perturbation. In particular, mechanical pulling experiments allow one to directly study the energies responsible for the folding and interactions of macromolecules. Although commercial AFMs are widely available, critical issues still

need to be resolved for accurate force-spectroscopy measurements. This chapter described the theory and methods to calibrate the spring constant of the cantilever as well as several other critical factors that needs to be controlled, including mechanical noise, the environment condition, drift, and contamination.

# Chapter 4

## Theories of Single Polymer Pulling

Biopolymers such as DNAs, RNAs, and proteins are important structural and functional molecules in the cell. In order for these biopolymers to perform their designated functions, they often need to fold into specific conformations. The mechanism of the folding from initially random conformation is crucial towards understanding the enzymatic mechanisms and biological roles of these biopolymers. Like any chemical processes, protein folding is driven by free energy minimization. Therefore, precise measurement of the free energy of a protein in different conformations is a key step to understand the driving force of its folding. One of the most important driving forces in the assembly is the hydrophobic collapse, driven by the association of hydrophobic residues along the protein backbone. Due to complex interactions among amino acids in a protein and the all-or-none unfolding transition, it is difficult to assess of the free energy of hydrophobic collapse in a protein.

In this thesis, a simplified system of homopolymers is used to study hydrophobic collapse. Using single molecule force spectroscopy, the conformational state of a single polymer can be directly manipulated and its mechanical response provides vital clues to help decipher how the polymer unfolds. As a result, the hydration free energy ( $\Delta G^{hyd}$ ) difference between collapsed and extended conformations can be directly measured (Figure 1.1). The mechanical responses of polymers differ significantly depending on the solvent condition. A solvent is good for a polymer when the polymer-solvent interaction is more favorable than the polymer-polymer interaction, and vice versa for a poor solvent. In this chapter, the mechanical responses of polymers in good solvents (Section 4.1) and poor solvents (Section 4.2) are discussed from a theoretical perspective, with emphasis on the latter case.

## 4.1 Polymers in good solvents

The freely-jointed chain and the worm-like chain are two commonly used polymer models in single molecule force spectroscopy. Their construction and physical properties, in particular, their responses to mechanical stretches are introduced here.

### 4.1.1 Freely jointed chain (FJC) model

An ideal polymer in a good solution can be modeled as a freely jointed chain (Figure 4.1). In this model, the polymer is constructed from connected segments with identical lengths. Adjacent segments can rotate freely about their joint. The volume exclusive effect of the polymer is neglected in this model. Although highly idealized, this model captures essential polymer physical properties and can be expressed by analytical equations.

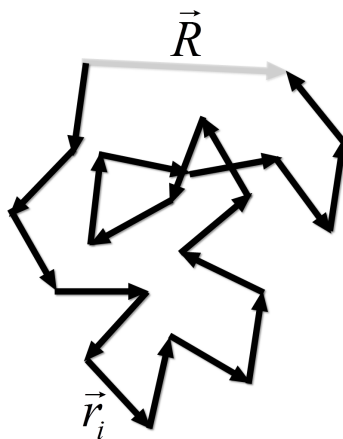


Figure 4.1: A freely jointed chain

The conformation of a freely jointed chain is equivalent to a random walk with steps sizes identical to the bond length of the polymer. Let  $\vec{R}$  be the end-to-end vector of the polymer, and  $\vec{r}_i$  be the vector of each segment, we have:

$$\vec{R} = \sum_i \vec{r}_i \quad (4.1)$$

$$|\vec{r}_i| = l \quad (4.2)$$

The length  $l$  of each segment is also known as the Kuhn length. Because the direction vectors are uncorrelated, the expected dot product between any two distinct segments is zero:

$$\langle r_i \cdot r_j \rangle = 0 \quad (4.3)$$

for  $i \neq j$ . Since the polymer conformation can be modeled as the trajectory of a three dimensional random walk, the properties of a one dimensional walk is first studied. For a one dimensional random walk of a total of  $N$  unit steps, in order that the last step ends at position  $n$ , the number of forward  $n_f$  and backward  $n_b$  steps must satisfy the following relation:

$$n_f + n_b = N \quad (4.4)$$

$$n_f - n_b = n \quad (4.5)$$

Hence,

$$n_f = \frac{1}{2}(N + n) \quad (4.6)$$

$$n_b = \frac{1}{2}(N - n) \quad (4.7)$$

The total number of combinations for such configuration is:

$$\binom{N}{n_f} = \frac{N!}{n_f!n_b!} = \frac{N!}{\left(\frac{1}{2}(N + n)\right)! \left(\frac{1}{2}(N - n)\right)!} \quad (4.8)$$

Assuming the probability to take a step forward is  $p$  and backward is  $1 - p$ , the probability of landing at position  $n$  is then:

$$P(n) = \frac{N!}{\left(\frac{1}{2}(N + n)\right)! \left(\frac{1}{2}(N - n)\right)!} \cdot \frac{1}{p^n(1 - p)^{N-n}} \quad (4.9)$$

For an unbiased random walk, the forward and backward probabilities are  $1/2$ . We take natural log on both side of the equation to obtain:

$$\ln P(n) = \ln N! - \ln \left(\frac{1}{2}(N + n)\right)! - \ln \left(\frac{1}{2}(N - n)\right)! - N \ln 2 \quad (4.10)$$

The natural log of factorials can be analytically expressed by the Stirling's approximation:

$$\ln n! = \left(n + \frac{1}{2}\right) \ln n - n + \frac{1}{2} \ln 2\pi \quad (4.11)$$

such that:

$$\begin{aligned}
\ln P(n) &= \left(N + \frac{1}{2}\right) \ln N \\
&\quad - \left(\frac{1}{2}(N+n) + \frac{1}{2}\right) \ln \frac{1}{2}(N+n) \\
&\quad - \left(\frac{1}{2}(N-n) + \frac{1}{2}\right) \ln \frac{1}{2}(N-n) - \frac{1}{2} \ln 2\pi - N \ln 2
\end{aligned} \tag{4.12}$$

Apply second order Taylor's expansion to approximate  $\ln(N-n)$ :

$$\begin{aligned}
\ln(N-n) &= \ln N + \ln\left(1 - \frac{n}{N}\right) \\
&\quad \ln N - \frac{n}{N} - \frac{1}{2}\left(\frac{n}{N}\right)^2
\end{aligned} \tag{4.13}$$

therefore Equation (4.12) can be simplified to:

$$\ln P(n) = -\frac{1}{2} \ln N - \frac{n^2}{N} + \frac{1}{2} \left(\frac{n}{N}\right)^2 (N+1) + (N+1) \ln 2 - \frac{1}{2} \ln 2\pi - N \ln 2 \tag{4.14}$$

Assuming  $N \gg 1$  the above equation simplifies to:

$$P(n) = \left(\frac{1}{2\pi N}\right)^{1/2} \exp\left(-\frac{n^2}{2N}\right) \tag{4.15}$$

Therefore, given a step size of  $l$ , the normalized probability to land at 1D location  $\vec{R}$  in a 1D random walk is:

$$P(\vec{R}) = \left(\frac{1}{2\pi N l^2}\right)^{1/2} \exp\left(-\frac{\vec{R}^2}{2N l^2}\right) \tag{4.16}$$

Generalizing this to three dimensions, the normalized probability distribution function becomes:

$$P(\vec{R}) = \left(\frac{3}{2\pi N l^2}\right)^{3/2} \exp\left(-\frac{3\vec{R}^2}{2N l^2}\right) \tag{4.17}$$

Because the probability distribution function is Gaussian, this model is also referred to as the Gaussian chain model. With the probability distribution function, observable physical properties can be computed. The expected end-to-end distance of a polymer scales to the square root of the number of segment and the segment length (See Ap-

pendix B for derivation):

$$\langle \vec{R}^2 \rangle = \iiint P(\vec{R}) \vec{R}^2 d\vec{R} = Nl^2 \quad (4.18)$$

Applying this scaling relation to calculate the expected distance between any two segments in the polymer,

$$\langle (\vec{r}_i - \vec{r}_j)^2 \rangle = |i - j| l^2 \quad (4.19)$$

using this, one can derive the radius of gyration of the polymer according to the definition:

$$R_g^2 = \frac{1}{N} \left\langle \sum_{j=1}^N (\vec{r}_j - \bar{r})^2 \right\rangle = \frac{1}{2N^2} \left\langle \sum_{i,j} (\vec{r}_i - \vec{r}_j)^2 \right\rangle \quad (4.20)$$

where  $r_i$  and  $r_j$  are the positional vectors of polymer segment  $i$  and  $j$ . Solving this equation gives the radius of gyration of a freely-jointed chain at rest:

$$R_g^2 = \frac{Nl^2}{6} \quad (4.21)$$

The entropic elasticity of the Gaussian chain can be calculated by assuming the probability distribution function is proportional to the conformational states with a given end-to-end distance.

$$S = k_B \ln P(\vec{R}) \quad (4.22)$$

Considering no enthalpic contribution during the mechanical distortion, the work done to the polymer balances the entropic loss:

$$\langle f \rangle = -\frac{dW}{dR} = T \frac{dS}{dR} \quad (4.23)$$

Evaluation of this with Equation (4.12) and Equation (4.17) gives:

$$\begin{aligned} \langle f \rangle &= k_B T \frac{1}{P(R)} \frac{dP(R)}{dR} \\ &= k_B T \frac{3R}{Nl^2} \end{aligned} \quad (4.24)$$

This is the ensemble average of force given a constant end-to-end distance, which shows a Hookean linear spring response. The Gaussian chain approximation is good when the

polymer is only slightly distorted.

Lastly, the end-to-end response of a polymer to a constant force  $f$  acting on its ends is examined. Because there are no interactions between the chain or constraints to the bending of the chain, the only contribution to the energy due to the external force gives the following partition function:

$$Q = \int_V \mathbf{r}^N \exp\left(\frac{\vec{f} \cdot \vec{R}}{k_B T}\right) \quad (4.25)$$

where the integration is over the entire phase space  $V$  of the direction vector  $\vec{r}_i$ . The total length of the polymer,  $R$ , is:

$$\vec{R} = \sum_{i=1}^N \vec{r}_i \quad (4.26)$$

and the dot product of force and an arbitrary segment  $i$  is:

$$\vec{f} \cdot \vec{r}_i = fl \cos \theta_i \quad (4.27)$$

The partition function (Equation (4.25)) can then be simplified to:

$$\begin{aligned} Q &= \left[ \int_0^{2\pi} d\phi \int_0^\pi d\theta \exp\left(\frac{fl \cos \theta}{k_B T}\right) \right]^N \\ &= \left[ \frac{2\pi k_B T \sinh(fl/k_B T)}{fl} \right]^N \end{aligned} \quad (4.28)$$

The expected value of  $R$  is then:

$$\langle \vec{R} \rangle = \frac{1}{Q} \int_V d\mathbf{r}^N \vec{R} \exp\left(\frac{\vec{f} \cdot \vec{R}}{k_B T}\right) \quad (4.29)$$

This is equivalent to:

$$\langle \vec{R} \rangle = \left( k_B T \frac{\partial}{\partial \vec{f}} \ln Q \right) \hat{f} \quad (4.30)$$

An exact solution to the force-response of the FJC can be obtained:

$$\langle \vec{R} \rangle = Nl \left[ \coth \frac{fl}{k_B T} - \frac{k_B T}{fl} \right] \hat{f} \quad (4.31)$$

where  $Nl$  gives the contour length of the chain and all force response curves can be normalized with respect to  $Nl$  (Figure 4.2).

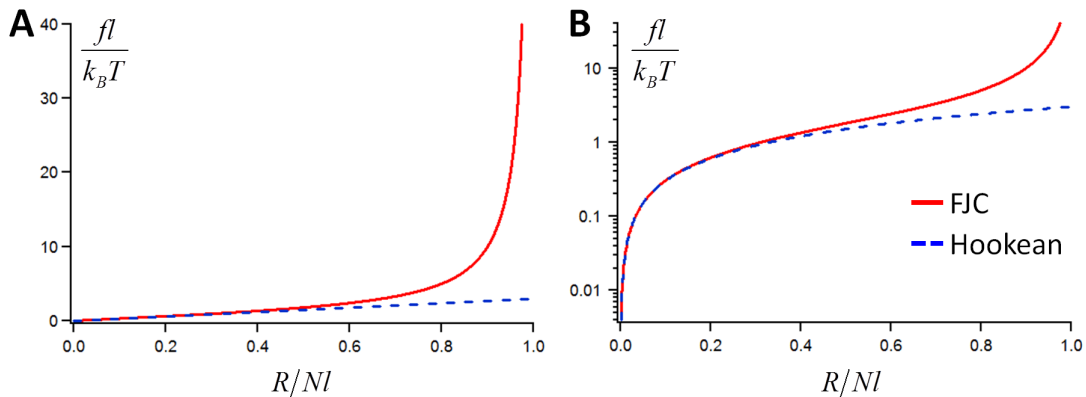


Figure 4.2: FJC force-distance response curves in A. linear and B. log vertical scales. The red curve shows the FJC force-distance curve according to Equation (4.31), the blue dotted line is the Hookean response for a Gaussian chain at the low force limit, according to Equation (4.24).

A freely-jointed chain does not have stiffness, which may be insufficiently realistic for many biological polymers. The following section describes the worm-like chain model where the stiffness of the polymer chain is incorporated.

### 4.1.2 Worm-like chain (WLC) model

The worm-like chain (WLC) is able to model chain stiffness. A number of key differences distinguish the WLC from FJC. First, the WLC models a continuous chain without segments where one does not need to specify a unit segment length (Figure 4.3). Secondly, bending elasticity is incorporated in the model such that the free energy is related to local curvature. Lastly, unlike the FJC where adjacent segments have uncorrelated direction vectors, the direction vector has a coherence length along the chain, characterized by the persistence length  $L_p$ :

$$\langle \hat{t}(s) \cdot \hat{t}(s + \Delta s) \rangle = \exp\left(-\frac{|\Delta s|}{L_p}\right) \quad (4.32)$$

The force-displacement responses of the WLC have been investigated [135, 174, 115, 160]. Although an exact analytical solution to mechanical response of the worm-like chain does not exist, an interpolated form has been described by Marko and Siggia [115] (Figure 4.4), which best fit experimental DNA pulling data at lower than 5 pN forces [173]:

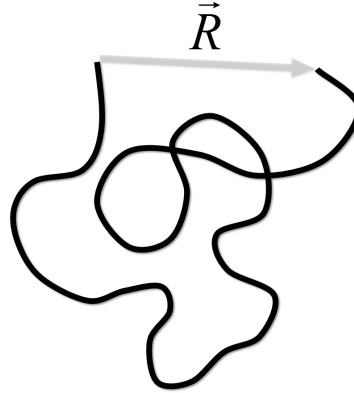


Figure 4.3: The worm-like chain.

$$F = \frac{k_B T}{L_p} \left[ \frac{1}{4(1 - x/L_0)^2} - \frac{1}{4} + \frac{x}{L_0} \right] \quad (4.33)$$

where  $k_B$  is the Boltzmann's constant,  $T$  is temperature in Kelvin,  $L_0$  is the contour length of the polymer, and  $x$  is the actual end-to-end distance. The deviation between experimental data and the fit originate from the enthalpic contribution when the chemical bonds are stretched at forces greater than 9 pN [173]. Odijk phenomenologically incorporated enthalpic bond stretching modulus  $K_0$  into the WLC model and gave the following interpolated force response [135]:

$$x = L_0 \left[ 1 - \frac{1}{2} \left( \frac{k_B T}{F L_p} \right)^{1/2} + \frac{F}{K_0} \right] \quad (4.34)$$

This empirical formula fits the experimental DNA pulling data at relatively higher force ranges, requiring the fitting curve to begin above 2 pN and to end above 15 pN. Wang et al. [173] provided a more generalized formula modified from the Marko-Siggia formula:

$$F = \frac{k_B T}{L_p} \left[ \frac{1}{4(1 - x/L_0)^2} - \frac{1}{4} + \frac{x}{L_0} - \frac{F}{K_0} \right] \quad (4.35)$$

This modified Marko-Siggia model fits experimental data well over a large range of force. At high force limit, it reduces to the Odijk [135] formula. With this analytical formula, one can estimate the persistence length of a polymer by fitting the force-distance curve (Figure 4.5) [21].

Figure 4.4 compares the force-extension curves between the WLC, FJC and Gaussian chain models. The low force responses of both WLC and FJC converge to the Hookean response of the Gaussian chain. At higher forces, the WLC exerts greater restoring force than the FJC at a fixed extension and fits better to more rigid biological polymers.

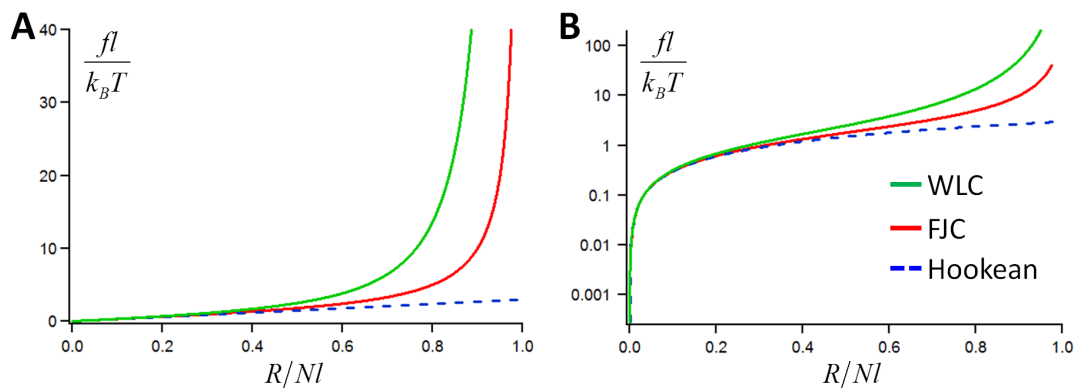


Figure 4.4: Comparison of WLC, FJC and Gaussian chain force-distance response curves in A. linear and B. log scales. The green curve shows the WLC force curve according to Equation (4.33), the red curve shows the FJC force curve according to Equation (4.31), the blue dotted line is the Hookean response at the low force limit according to Equation (4.24). The persistence length for the WLC is chosen to be half of the Kuhn length for the FJC in the plot.

Figure 4.5 shows that WLC fits well to the force-extension curve of polystyrene in toluene, a good solvent for polystyrene.

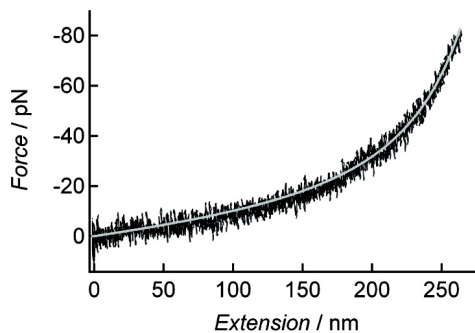


Figure 4.5: Force extension curve of polystyrene in toluene, a good solvent. The grey line is the WLC fit, giving a persistence length of  $0.25 \pm 0.05$  nm, consistent with literature [60]. (Figure adapted from Gunari et al. [60])

## 4.2 Polymers in poor solvents

A polymer undergoes a coil-globule phase transition from random coil in a good solvent to compact globule in a poor solvent. In a poor solvent such as water, the polymer-polymer interaction is preferred over polymer-solvent interaction, causing the chain to collapse into a compact globule. Due to their simplicity, hydrophobic homopolymers have been used for theoretical investigation of hydrophobic collapse [7, 167, 35, 57, 65, 114, 140].

In the presence of an external force, three stages during the pulling of a hydrophobic homopolymers in poor solvent were predicted by theory [65]. In the first stage, a force below a threshold value distorts the spherical collapsed globule into an ellipsoidal shape. As pulling continues, the threshold force is reached and the polymer undergoes a first-order phase transition that dissolves the collapsed globule into an extended coil until the chain is fully exposed to the solvent. The force curve during this stage exhibits a plateau where the collapsed and extended states co-exist in a dynamic equilibrium. The last stage is marked by an entropic elastic response of the chain similar to pulling a polymer in good solvent, which can be described by the WLC model. The mechanical pulling of polymers in poor solvent has been extensively investigated using scaling theory [65], self-consistent field theory [140], lattice models [114] and molecular dynamics simulations [35, 57] (Figure 4.6).

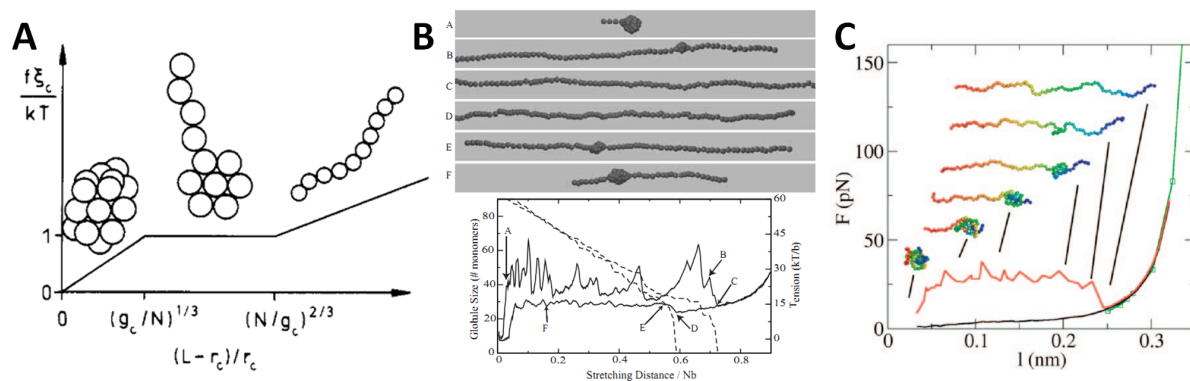


Figure 4.6: Theoretical and simulation models show that unfolding of homopolymers in poor solvent condition gives a force plateau in the force-extension curve. A. Zhulina-Halperin scaling model [65, 190, 191] B. molecular dynamics simulation from Cooke et al. [35], C. Molecular dynamics simulation from Grater et al [57]. (Figures adapted from their references [35, 65, 57].)

### 4.2.1 Analytical model of pulling a single chain from collapsed state

A simple analytical model that captures most of the physics in pulling a polymer in poor solvent from a collapsed to an extended state is described here. This model is built upon the model of Halperin and Zhulina [65, 66] that yields a collapsed-extended coexistence state before reaching the fully solvent exposed state. Several modifications were made to suit this model to our systems (see Figure 4.7a). Instead of assuming the extended state is composed of smaller sized collapsed blobs on a Gaussian chain, here we model

the extended state as a single worm-like-chain with a constant diameter. The collapsed state is modeled as a sphere with size at least 10 times greater than the diameter of the chain. The total volume of the sphere and the flexible rod is conserved:

$$V = \frac{4}{3}\pi R^3 + \pi r^2 L \quad (4.36)$$

where  $R$  is the radius of the collapsed sphere,  $r$  is the radius of the rod modeling the single chain, and  $L$  is the contour length of the extended component of the chain. While holding the end of the extended component at a fixed distance, an intricate balance of forces at the interface occurs between the collapsed and extended component of the chain. At the interface, the entropic elastic force from the extended single chain component balances the force that pushes the extended component back into the collapsed component due to the solvophobic effect. The WLC model (Equation (4.33)) [115, 26] was used to obtain the force from the entropic elasticity of the extended component of the chain. Similar to the Halperin-Zhulina model [65, 66], we assume the change in total  $\Delta G^{hyd}$  is proportional to the change in area and interfacial tension between the polymer and solvent. Assuming the first derivative of force-extension curve is continuous, the change in  $\Delta G^{hyd}$  of the system should equal to the work done by the entropic elasticity if the end-to-end distance  $x$  changes by an infinitesimal amount  $dx$ :

$$Fdx = \gamma_i dA \quad (4.37)$$

where

$$A = 4\pi R^2 + 2\pi r L \quad (4.38)$$

where  $\gamma_i$  is the interfacial tension between the polymer chain and the solvent,  $A$  is the total surface area of the polymer including the collapsed and extended components. This is then simplified to:

$$F \frac{x}{L} = 2\pi r \gamma_i \left(1 - \frac{r}{R}\right) \quad (4.39)$$

By parameterizing  $x$  and  $F$  with  $\phi = x/L$  (see Appendix A), the numerical solutions to this equation can be obtained with the parameters listed in Table 4.1.

$$x(\phi) = \frac{V}{\pi r^2} \phi - \frac{4r}{3 \left(1 - \frac{F(\phi)\phi}{2\pi r \gamma_i}\right)^3} \phi \quad (4.40)$$

Using parameters from Table 4.1, the force-extension profile from this model (See Ap-

Parameters	Value
$\gamma_i$	40.0 mJ/m <sup>2</sup>
$V$	$4.7 \times 10^{-26}$ m <sup>3</sup>
$r^\dagger$	0.25 nm
# monomers	1000
Monomer length	0.24 nm
$L_p$	0.92 nm
$T$	300 K

<sup>†</sup> The radius of the cylinder is a crude estimate based on the size of a styrene molecule using bond lengths and simple geometry. This is only meant to give the approximate order of magnitude and not the exact value for the force opposing polystyrene extension.

Table 4.1: List of parameters used in the analytical model

pendix A for derivation) shows a well-defined plateau with slight negative slope towards higher extension at roughly 1.8 pN per 100 nm of extension (Figure 4.7c). The assumption that the collapsed sphere is much greater in size than the diameter of the extended worm-like chain begins to fail towards higher extension length when the number of monomers in the collapsed state is on the order of 10s; this model cannot accurately predict the force-extension response in the transition from the collapsed-extended coexistence state to the fully extended state (indicated as the “uncertain” region in Figure 4.7c&d). Beyond the transition region, the chain has no collapsed component and shows only the entropic elastic response. The plateau force region is where the collapsed and extended components coexist within the polymer chain. The magnitude of the constant force in the plateau region is nearly entirely contributed by the solvation of chain from collapsed to extended state, and is therefore proportional to solvent exposed area and the interfacial tension between the polymer and the solvent. As shown in Figure 4.7b, the force plateau magnitude  $F_{plateau}$  can be linearly related to the interfacial tension by:

$$F_{plateau} = (1.53 \pm 0.04)\gamma_i + (2 \pm 1) \quad (4.41)$$

where  $F_{plateau}$  is in the unit of pN and  $\gamma_i$  is in the unit of mJ/m<sup>2</sup>.

As will be discussed below, the AFM experiment provides similar linear correlation between the plateau force magnitude and the polystyrene-solvent interfacial tension. The

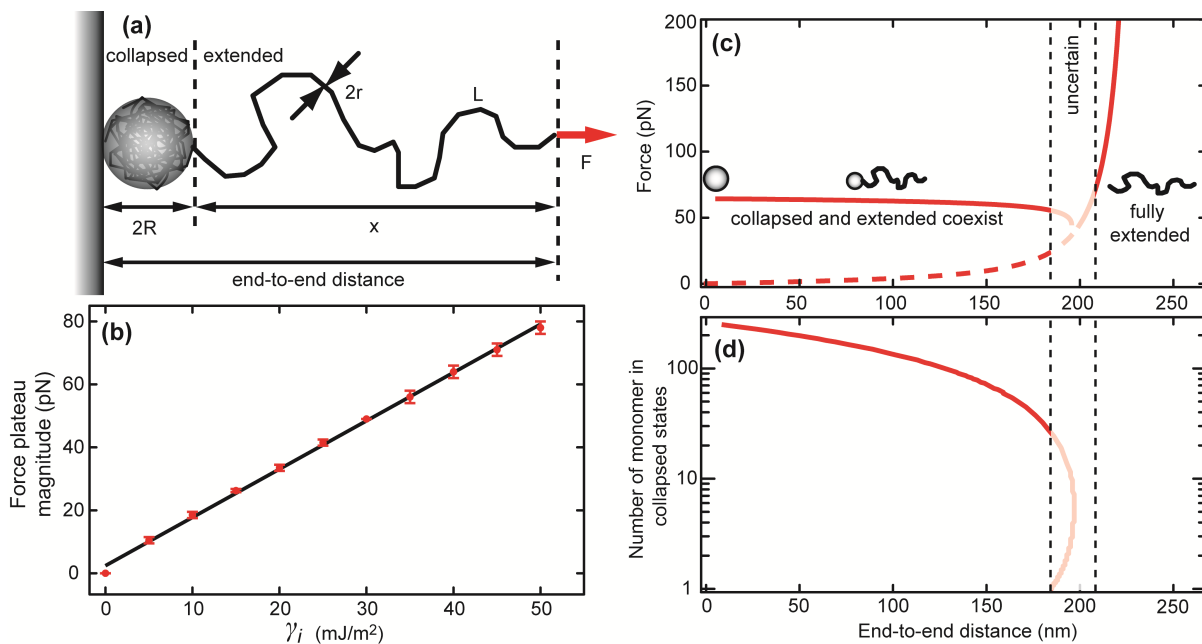


Figure 4.7: Simple analytical model and results: (a) Illustration of the pulling experiment, the coexistence of collapsed and extended state in the same polymer as well as the entropic elastic response of the extended state.  $R$  is the radius of the collapsed sphere,  $r$  is the radius of the single chain modeled as a flexible rod,  $L$  is the contour length of the extended single chain,  $x$  is the end-to-end distance of the extended single chain, and  $F$  is the force applied to the single chain. (b) illustrates the plateau force calculated from the analytical model against the interfacial tension used in the calculation. (c) and (d) are predictions of the analytical model: (c) shows the force-extension profile using the model, (d) shows the number of monomers in the collapsed sphere in log scale. The grayed-out uncertain area indicates regions where there will be a failure of the assumption that the collapsed state will remain spherical when there are only a small number of monomers in the collapsed state.

model would produce similar results if there were more than one collapsed component along a single chain, for example one adsorbed onto the AFM tip and another one adsorbed onto the surface or more than one suspended between the tips. However, more realistically, many smaller collapsed components are not as favored energetically as few, larger ones on a single chain. Therefore, it is expected that the smaller collapsed components will dissolve and contribute to create a single, larger, collapsed state.

This model does not take into account the elastic response from the collapsed component of the chain because it is assumed the collapsed state is much larger in size compared to the worm-like-chain. If a very large collapsed component size is assumed, the change in surface area caused by the external force is relatively small compared to the total area of the collapsed state, and hence can still be approximated by a sphere. The deformation of the collapsed component modeled by Halperin and Zhulina is limited only to the region before the extended-collapsed coexistence state. Since the initial deformation is not the focus of the current discussion, this was neglected from our model. However, we are interested in the effect of the collapsed component deformation in our finite sized system at the coexistence stage of the extension. One can imagine that, under tension, the collapsed component would be elongated to an ellipsoidal shape rather than a perfectly spherical shape. This ellipsoidal geometry increases the surface area of the collapsed component which would have an impact on the force-extension profile. At the same distortion force, the degree of distortion would be greater on a smaller collapsed component than on a larger one due to less inter-chain interactions. Therefore, this model's assumption of a spherical collapsed component at all stages of the extension has underestimated the surface area of collapsed component, and therefore the total solvent exposed area of the whole polymer. Toward higher extension the increase of solvent exposed area is further underestimated as the solvent exposed area of the collapsed component is increased due to higher degree of deformation. Hence, the force is also underestimated at higher extension in the collapse-extended coexistence state. Therefore, the elastic distortion of the collapsed component could ease the negative slope of the force-extension plateau if it were incorporated in the model. Here we do not include this effect for two reasons: 1, we cannot estimate the elastic response of the collapsed component in a simple way and 2, the current model captures the main behavior.

Another aspect to consider, given recent developments of hydrophobic theory, is the size effect of the hydrophobic solute [112, 74]. It has been shown that  $\Delta G^{hyd}$  of small hydrophobic particles on the order of several Angstroms do not scale with a particle's surface area, but rather with its volume. This lowers  $\Delta G^{hyd}$  of small solutes when comparing to what one would expect if it were to scale with the former. If this indeed applies

to the solvation of each monomer along the polymer chain, a scaling factor could be added to Equation (4.41), which would influence the magnitude of the plateau force, but not the overall shape of the force-extension profile. This is because  $\Delta G^{hyd}$  per monomer is identical; therefore, the total  $\Delta G^{hyd}$  of  $N$  monomer units would be proportional to  $N$ , which in the case of the linear polymer is also directly proportional to the length of the extended chain. Thus, the size effect is applicable to the individual monomers along the chain and hence does not alter the key features of the model. To illustrate this more clearly, we consider this simple equation:

$$\Delta G_{total}^{hyd} = \alpha(R)N\gamma_i \quad (4.42)$$

where  $\Delta G_{total}^{hyd}$  is the total  $\Delta G^{hyd}$  of the extended chain,  $N$  is the length of the extended chain in number of monomers,  $\alpha(R)$  is a size-dependent, effective surface area per monomer, and  $\gamma_i$  is the polymer-solvent interfacial tension. The force plateau in experiment force-curves confirms that  $\Delta G_{total}^{hyd}$  of the extended chain is proportional to length:

$$\Delta G_{total}^{hyd} \propto N \quad (4.43)$$

By varying solvent conditions, as seen in Chapter 7, the  $\Delta G_{total}^{hyd}$  is linearly dependent on the polymer-solvent interfacial tension:

$$\frac{\Delta G_{total}^{hyd}}{N} \propto \gamma_i \quad (4.44)$$

The value of  $\alpha(R)$  can be obtained from the slope from plotting  $\Delta G_{total}^{hyd}/N$  against  $\gamma_i$  as will be shown in Chapter 7.

Whether the solvation of individual monomers on a polymer chain is strongly size dependent is still debated: when extended, a polymer is a macroscopic object in the dimension along the chain, and obeys a surface area dependent scaling law, but it is microscopic in the radial direction, where a hydrophobic size effect might play a role. Therefore,  $\Delta G^{hyd}$  per monomer on the polymer may not be simply equated to  $\Delta G^{hyd}$  of the monomer alone in the solvent.

### 4.2.2 Ising model simulations

A simple 3D square-lattice Ising model was developed to simulate the behavior of a single hydrophobic polymer under tension. Water as the solvent is modeled by a 3D Cartesian lattice following the methods from ten Wolde et al. [167] (Figure 4.8 illustrates the 2D

variation of the lattice). Periodic boundary condition was applied and a lattice size of 0.24 nm was used.

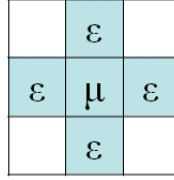


Figure 4.8: Illustration of the solvent model on a 2D lattice showing the solvent chemical potential and the nearest neighbor coupling energy.

To model the solvent, the energy for a given lattice site  $i$  is:

$$E_i = -\mu n_i - \varepsilon \sum_{\langle j \rangle} n_i n_j \quad (4.45)$$

where  $n_i$  is the occupancy of each lattice site, which takes the value of 1 if it is occupied by water, and 0 if it is a cavity; no intermediate values are allowed. The solvent chemical potential  $\mu$  can be expressed as:

$$\begin{aligned} \mu &= \mu_{coex} + \Delta\mu \\ &\approx -3\varepsilon + \Delta P l^3 \end{aligned} \quad (4.46)$$

where  $\Delta\mu$  is the reversible work due to volume expansion of the lattice site, and  $\mu_{coex}$  is the chemical potential for water liquid vapor coexistence, and is roughly 3 times the nearest neighbor coupling energy  $\varepsilon$ , which is calculated based on the surface tension of water:

$$\varepsilon = 2\gamma l^2 \quad (4.47)$$

Given all of the above, the energy of the  $i^{th}$  lattice site can be expressed as:

$$E_i = -(-6\gamma l^2 + \Delta P l^3) n_i - 2\gamma l^2 \sum_{\langle i,j \rangle} n_i n_j \quad (4.48)$$

Each polymer unit is modeled as a cubic bead that occupies a  $3 \times 3 \times 3$  lattice space and can only move on the solvent lattice with discrete steps. This greatly simplifies the conformational degree of freedom of the polymer, thereby speeding up the simulation. At the same time, the essential polymer behaviors are preserved as will be shown later. Special considerations were given to the connectivity between adjacent units. If all

connected configurations between two adjacent units are allowed with volume exclusion (Figure 4.9), there is a large variation in the total surface area and the center-to-center distance (Table 4.2). Energetic penalty that favors the more constant center-to-center length can restrict the available conformation mode to only the top 3 in Table 4.2 such that transition from one conformation to another has a large energetic barrier. In addition, in a model that counts on exposed surface area, modes close to the bottom of Table 4.2 change the surface area by approximately 20%.

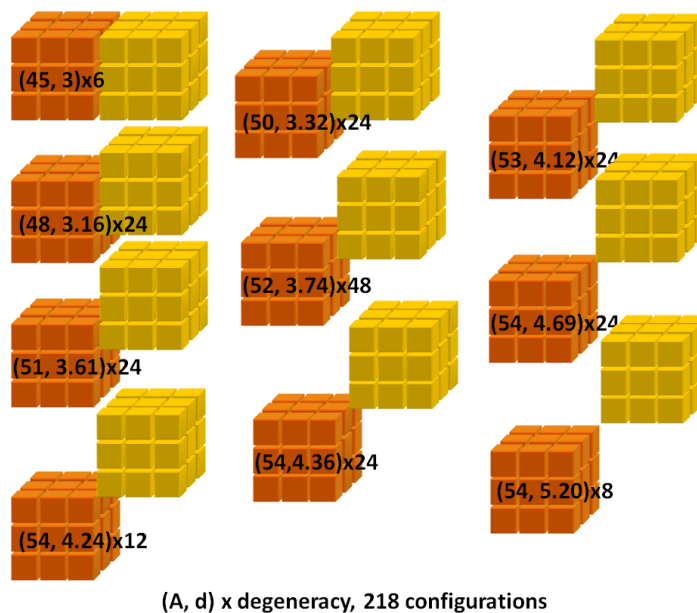


Figure 4.9: Configurations between two adjacent polymer units. Total surface area  $A$ , center-to-center distance  $d$ , and the degeneracy of each mode are listed on the graph.  $(A, d) \times$  degeneracy, all in the unit of grid.

To solve this problem three alternative modes were allowed (bottom 3 of Figure 4.10) with maximal 3 overlapping lattice sites. These allows for a total of 98 configurations between adjacent monomers (Table 4.3). With this configuration, the difference in total surface area differ by up to 10%. In addition, the transition energy barrier between any two allowed connection configurations is minimized. A fast algorithm looks up the relative positions of the two adjacent units and returns the number of overlapping lattice sites.

The total energy of the system is the sum of the following factors:

- **Neighboring polymer-polymer unit interactions:** contains repulsive and attractive potentials to keep the polymer chain connected and volume excluded.

Surface area ( $A$ )	Distance ( $d$ )	Degeneracy
45	3.00	6
48	3.16	24
50	3.32	24
51	3.61	24
52	3.74	48
53	4.12	24
54	4.24	12
54	4.36	24
54	4.69	24
54	5.20	8

Table 4.2: Table listing the total surface area  $A$  (grid<sup>2</sup>), center-to-center distance  $d$  (grid), and the degeneracy of each mode.

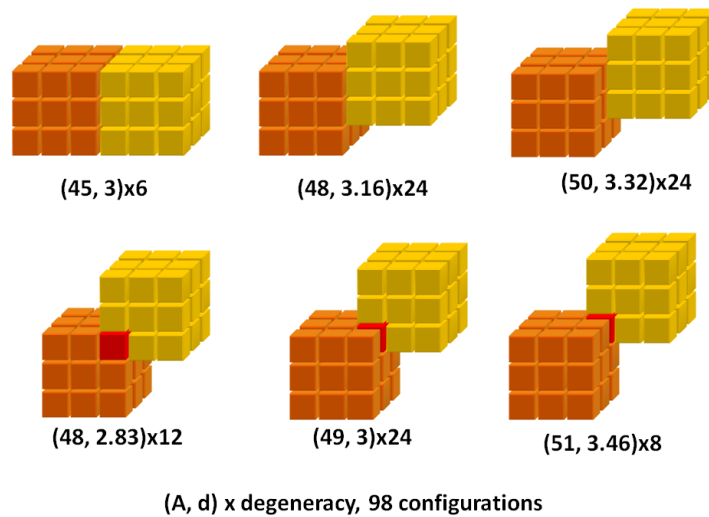


Figure 4.10: The modified model has 6 allowed modes for adjacent units. The total surface area  $A$ , center-to-center distance  $d$ , and the degeneracy of each mode are listed on the graph.  $(A, d) \times$  degeneracy, all in the unit of grid. Red grids indicate overlapping polymer units. These modes are only allowed for adjacent polymer units.

Surface area ( $A$ )	Distance ( $d$ )	Degeneracy
48	2.83	12
45	3.00	6
49	3.00	24
48	3.16	24
50	3.32	24
51	3.46	8

Table 4.3: List of surface area  $A$ , distance  $d$  and degeneracy of the modified model.

- **Non-neighboring polymer-polymer interactions:** contains electrostatic and dispersive terms, which is effectively the surface tension of the polymer.
- **Polymer-water interactions:** essentially work of adhesion between polymer chain and water
- **Water-water interactions:** essentially the cavitation free energy.

In each simulation step, one polymer unit is randomly chosen and the equilibrium free energy of the local polymer-solvent system is calculated for each position the chosen could move to. The minimal energy movement is then chosen to move this polymer unit. We first tested this model by allowing an initially linear hydrophobic polymer to relax in water. Figure 4.11 shows the polymer collapse in water as the radius of gyration ( $R_g$ ) decreases as the simulation progresses.

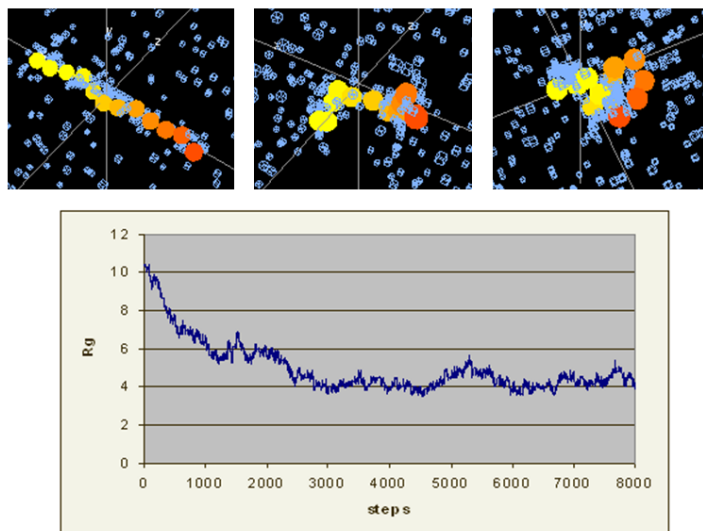


Figure 4.11: The collapse of a hydrophobic 12-mer in water. The polymer is colored based on the sequence of the units. Blue cubes in the solvent indicate a water lattice site is vacant.

To study the effect of solvent condition on the polymer mechanical response, different polymer-water interaction strengths were used. Figure 4.12 shows a hydrophilic (in this case, the polymer-water interaction has 90% strength as water-water interaction) 20-mer in water has large conformational fluctuation throughout the duration of the simulation, which indicates that it is just a random coil adapting various conformations in water (Figure 4.12). As the hydrophobicity of the polymer increases, they adapt a collapsed conformation as the  $R_g$  stays constant; the  $R_g$  of the collapsed hydrophobic polymer is also much smaller than the average of hydrophilic polymer (Figure 4.12).

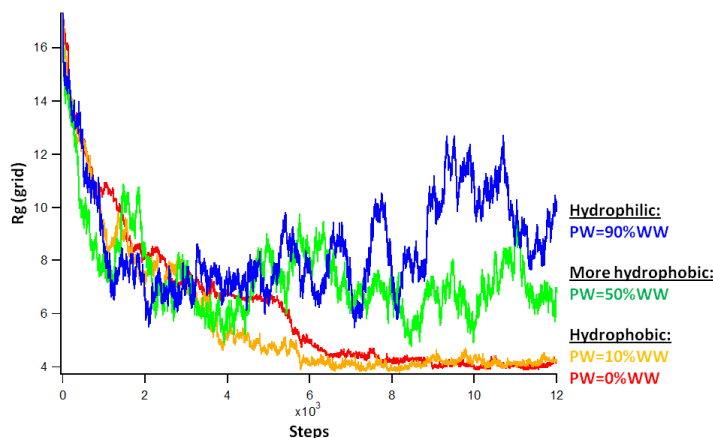


Figure 4.12: The trajectory of radius of gyration ( $R_g$ ) of a 20-mer, ranging from hydrophilic (blue) to more hydrophobic (green), to completely hydrophobic (orange and red). Each monomer occupies 3 lattice grids; therefore the starting linear conformation has a  $R_g$  of 17.3 grids.

Opposing constant forces to the terminal units of the polymer is achieved by applying a biasing potential to their equilibrium free energy. The equilibrium end-to-end distance of the polymer is recorded as a function of force. A 20-mer hydrophilic polymer exhibits an entropic elastic response as shown in Figure 4.13. Given the 2.4 Å lattice spacing, the polymer should have a contour length of 14.4 nm. A worm-like-chain was used to fit the simulation result, giving a persistence length of  $1.3 \pm 0.4$  Å and contour length of  $15.1 \pm 0.2$  nm, similar to their expected values.

Similarly, a 20-mer hydrophobic polymer in water was simulated at various pulling forces. The fully extended initial state was used in all simulations where the chain was allowed to relax to equilibrium. It was shown that the choice of initial state does not alter the equilibrium properties of this model.

At forces below 100 pN, the polymer remains stably collapsed with small end-to-end distances (Figure 4.14). When the applied force reaches above 120 pN, the polymer assumes an extended conformation (Figure 4.14) with most of the chain exposed to solvent. In the force region between 100 pN and 120 pN, the equilibrium end-to-end distance undergoes a phase-like transition from a collapsed state to an extended phase with the applied force as the reaction coordinate (Figure 4.15A). The phase transition is marked by the large magnitude end-to-end distance fluctuation (Figure 4.15B) as the polymer conformation fluctuates between an extended and collapsed state, forming transient locally collapsed blobs along the chain (Figure 4.14).

The Ising simulation shows force induced phase transition between the extended and

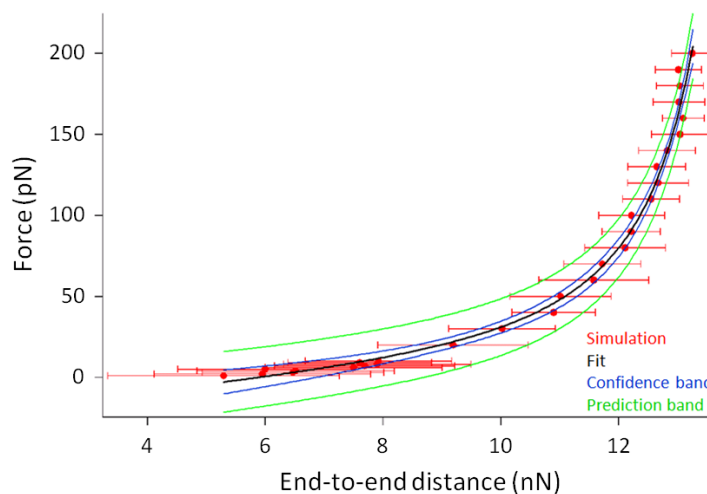


Figure 4.13: The WLC fit to the force-extension response curve of a 20-mer hydrophilic polymer. The average end-to-end distance is shown as red dots, the error bars reflect the standard deviation of the end-to-end distance fluctuation at a particular force value. The WLC fit is shown as black line. The confidence and prediction bands are blue and green.

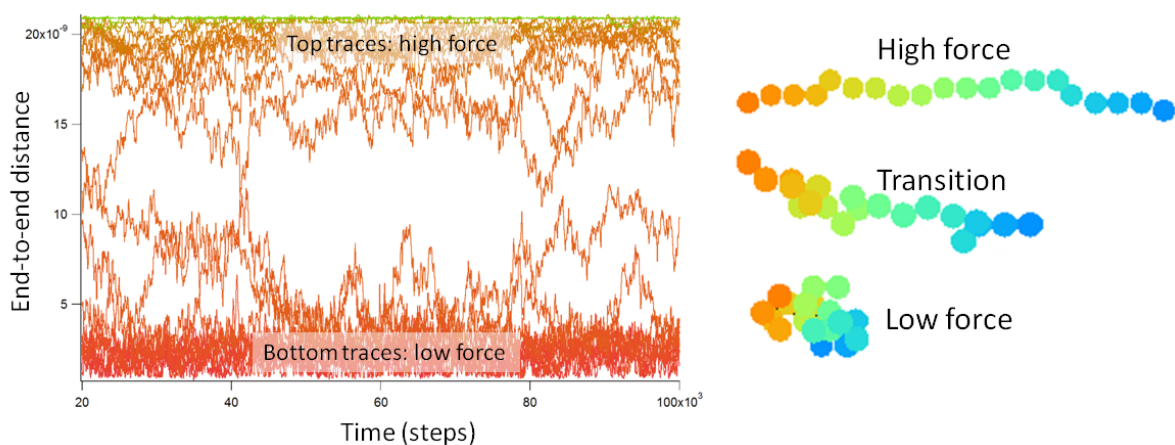


Figure 4.14: Simulation of polymer collapse under tension. Left, equilibrium end-to-end distance trajectories of polymers under different tension. Right, from bottom to top: a collapsed conformation under low force, under force in the transition regime, and an extended polymer under high force.

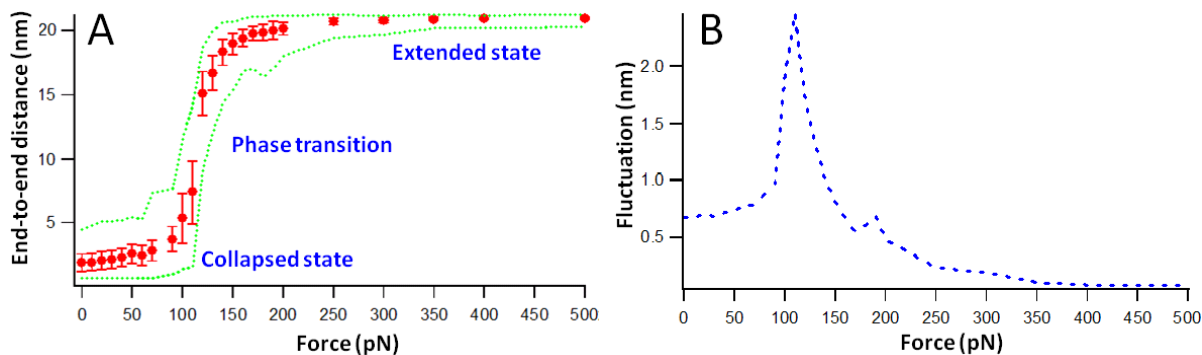


Figure 4.15: A. Equilibrium end-to-end distance (red dots) vs. external tension. Error bars indicate the standard deviation of the end-to-end distance. The green dotted lines show the maximum and minimum of the end-to-end distance in each recorded end-to-end distance trajectory. B. The fluctuation amplitude (as standard deviation) of the end-to-end distance vs. external tension.

collapsed conformation of a hydrophobic polymer in water, evident in the plateau behavior in the force-extension curve. The results here, both in profile and magnitude are comparable to the analytical model in Section 4.2.1 and other theoretical work.

### 4.3 Conclusion

This chapter reviewed and investigated how solvent conditions affect the mechanical response of a single polymer from a theoretical perspective. In a good solvent, the polymer responds to external force as a non-linear spring, as a result of entropic elasticity. The entropic elasticity arises from the reduction of conformational degree of freedom as the chain is pulled beyond its equilibrium conformation. The mechanical responses of two commonly used models, namely the freely-jointed chain (FJC) and worm-like chain (WLC), were described in detail. When the solvent condition is no longer favorable for the polymer to adopt randomly coiled conformations, the polymer collapses into a compact globule. The collapse of a hydrophobic homopolymer in water is such an example. The forced unfolding of a collapsed hydrophobic polymer in water drives the polymer through a coil-to-globule phase transition, where the work done by the external force counteracts on the driving force for the coil-to-globule collapse. The force-extension curve for such coil-to-globule transition is marked by a constant force profile, which we call the force plateau. This force plateau is followed by the entropic elastic response similar to that when the polymer is in good solvent condition after all collapsed globules are forced to solvate, and that there are no collapsed globules anywhere along the chain. This phenomenon has been studied here by means of an analytical model and an Ising

simulation. Experimental evidence of the unfolding of a single hydrophobic polymer in water will be discussed in the following chapter.

# Chapter 5

## Experiments of Hydrophobic Polymer Pulling

Given theoretical studies on the mechanical unfolding behavior of hydrophobic polymers, Figure 5.1 illustrates what one may expect to happen in a single molecule pulling experiment. A collapsed hydrophobic polymer in water can be forced to unravel with the AFM tip where a single chain is forced to hydrate as it is pulled out of the collapsed globule. From the force-extension curves during this process, the hydration free energy ( $\Delta G^{hyd}$ ) per monomer can be extracted. This chapter provides experiment evidence for single chain pulling events and for the hydration nature of these pulling events. In addition, the sample preparation and experimental procedures are detailed.

### 5.1 Typical force curve of hydrophobic homopolymer unfolding

Figure 5.2 shows an example of single molecule force-curve of polystyrene in water. The shape of the force curve closely resembles what was expected from theoretical and simulation studies (Section 4.2). The plateau region of the force curve corresponds to the unfolding of a hydrophobic homopolymer, where the polymer in the collapsed state coexists with extended state. As the plateau continues, the work done by the cantilever on the collapsed polymer provides it energy to hydrate, thereby converting more chains in the collapsed state into extended state until the entire chain is hydrated. At this point, any further stretching of the polymer follows the entropic elasticity as if the polymer is in a good solvent (Section 4.1). This is shown by a rapid rise of the force towards the end of the pull.

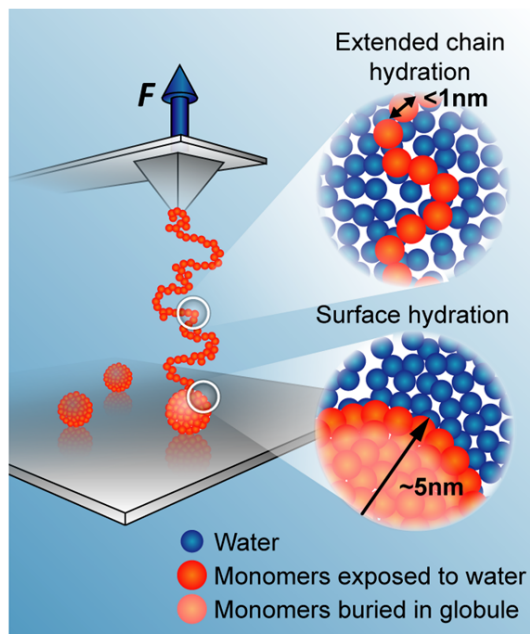


Figure 5.1: Single molecule pulling experiment of a hydrophobic polymer as it transitions from a collapsed to an extended state. AFM forces the hydration of a single hydrophobic polymer chain in water by pulling it from a collapsed state. The top magnified inset illustrates that the individual monomers on the sub nanometer length scale along the extended chain are hydrated. The bottom magnified inset illustrates that hydration of the collapsed globule follows a surface area controlled hydration process.

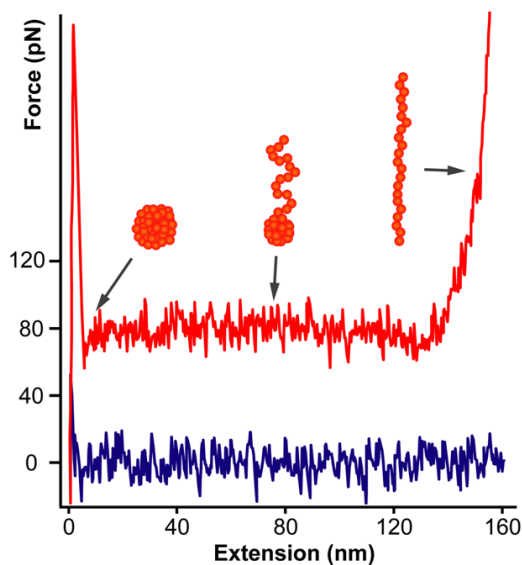


Figure 5.2: Typical AFM force-extension curve of a hydrophobic polymer in water or poor solvents. Data showing PS stretching in water. Blue curve is the approach curve where the force is zero. Red curve is the retracing force curve when a single chain is attached to the tip. The schematic shows the different stages of the single molecule pull.

## 5.2 Extract hydration free energy from force curves

As Figure 5.3 illustrates, the upper left portion shows a single molecule extension experiment that converts the collapsed conformation to the extended conformation through a coil-globule transition. In a thought experiment, relaxing the force while maintaining the extended conformation without inducing any collapsed structure leads to a fully hydrated random coil that maximizes chain entropy. The collapse of this fully hydrated random coil back to the collapsed conformation is the hydrophobic collapse identified in this work, and the free energy is associated with  $-\Delta G^{hyd}$ . Dispersed free monomers can be converted to the collapsed or random coil state through either aggregation or polymerization, respectively, preventing the free monomer  $\Delta G^{hyd}$  from being used directly in calculations of polymer hydration.

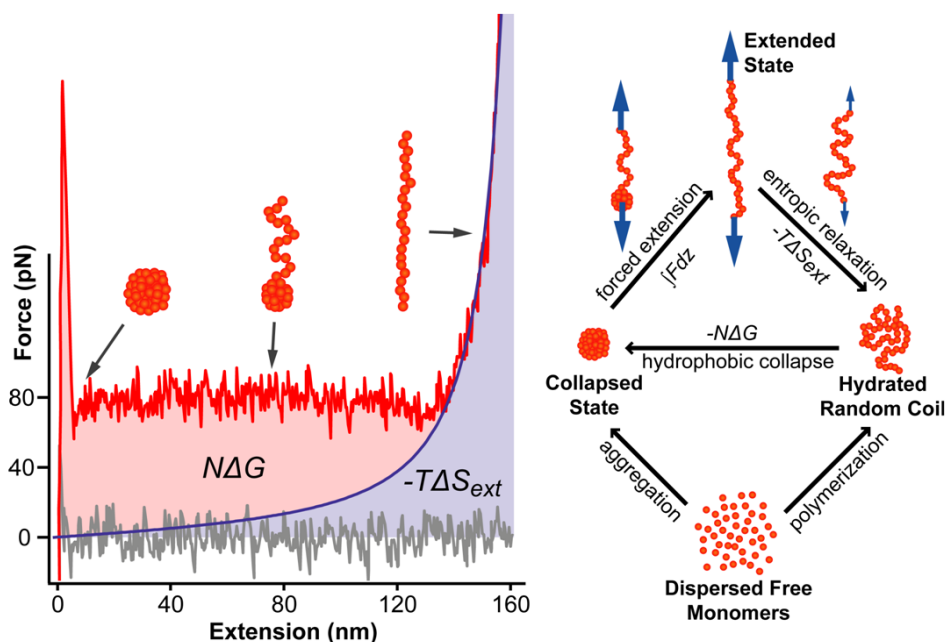


Figure 5.3: Single molecule pulling experiment are used to obtain  $\Delta G^{hyd}$  of a hydrophobic polymer as it transitions from a collapsed to an extended state. Left, a single molecule force-extension curve showing a force plateau followed by elastic stretching (red) and a baseline with no polymer attachment (grey). The force plateau corresponds to hydration of a single chain; the entropic elastic stretching occurs when the chain extension force is governed by entropy reduction, which is fit closely by the worm-like chain (WLC) model (blue). The area under the WLC fit (blue shade) contains the entropic contribution to the free energy extending the polymer from a collapsed globule. The area between the force plateau and the WLC fit (red shade) is due to hydration only. Right, free energy differences between polymers and free monomers in various conformational states.

The experimental procedure extending the polymer from a collapsed to an extended

state involves hydrating the chain and lowering the entropy of the chain (Figure 5.3). To separate  $\Delta G^{hyd}$ , the contribution associated with chain entropy must be subtracted from the total work done to stretch the chain (Figure 5.3):

$$\Delta G^{hyd}(T) = \frac{\int F(T)dz + T\Delta S_{ext}(T)}{N} \quad (5.1)$$

where  $\Delta G_{hyd}(T)$  is the temperature dependent hydration free energy per monomer on the chain,  $F(T)$  is the experimentally measured pulling force integrated over the plateau region of the force curve,  $\Delta S_{ext}(T)$  is the difference in entropy of a solvent exposed chain from random coil to elastically extended states,  $N$  is the number of monomers in the extended portion of the chain and  $T$  is temperature. Therefore, the contribution from  $\Delta G^{hyd}$  is calculated as the area between the force plateau and the entropic elastic response of the chain (Figure 5.3).

Given the known persistence length of a single polymer chain, the constant force ensures the percentage extension to the contour length of the extended chain also remains constant in the force plateau region. This is because the entropic elastic response of the extended chain can be normalized to a function of the percentage extension  $x/L_0$  by the worm-like chain response (Section 4.1.2):

$$F = \frac{k_B T}{L_p} \left[ \frac{1}{4(1 - x/L_0)^2} - \frac{1}{4} + \frac{x}{L_0} \right] \quad (5.2)$$

Therefore, even for force curves that do not show entropic elastic stretching (the chain breaks off from the tip before reaching the entropic elastic stretching region), we know exactly how to subtract the chain entropic elastic contribution from the total work. Furthermore, the entire force-curve is scalable as we will show in Section 5.4.5, therefore the plateau force is unaffected by the length of the pull.

## 5.3 Methods and materials

### 5.3.1 Substrate preparation

Silicon substrate was cut from a silicon wafer into 1 cm<sup>2</sup> squares. These substrates are subsequently cleaned by ‘‘piranha’’ solution (3:1 of 98% sulfuric acid to 30% hydrogen peroxide) for approximately 30 minutes. The piranha solution may be boiled to speed up the cleaning. This procedure removes organic materials on the substrate. The substrate is then rinsed and then kept in filtered (0.2  $\mu$ m cellulose) and deionized (18.2 M $\Omega$ ) water prior to sample deposition to minimize contamination. When taken out of the solution,

Si substrates were blow-dried with nitrogen gas. The direction of gas flow goes towards the tweezers, such that contaminants from the tweezers will not be carried onto the substrate.

Atomically flat gold (111) substrate was prepared from ultra-flat gold purchased from Ssens and Arrandee. The gold substrate was flame annealed by hydrogen flame for approximately 15 minutes to produce gold (111) surface. A well annealed gold substrate has a duller and whitish appearance. As the result of the annealing, single crystalline grains of gold approximately 500 nm in size can be seen under AFM scan. In addition, the gold (111) surface displays a signature triangular pattern due to atomic terraces. The flame annealed gold should be used as soon as possible to avoid contamination.

### 5.3.2 Polymer preparation

Polystyrene (PS) and Poly(4-*t*-butyl styrene) (PtBS) with molecular weight of 130 kDa and 145 kDa, and polydispersity index of 1.05 and 1.08 were purchased from Polymer Source (P5157-S, P8213-4tBuS). Poly(4-vinylbiphenyl) (PVBP) was purchased from Sigma Aldrich (CAS No. 25232-08-0, 182540-1G) with molecular weight of 115 kDa and unknown polydispersity index. The polymers were dissolved in distilled tetrahydrofuran (Sigma Aldrich) or toluene (Sigma Aldrich) at 1 mg/mL concentration for 6 hours and subsequently diluted to 1  $\mu\text{g}/\text{mL}$  and left to further dissolve for 24 hours. This procedure ensures polystyrene molecules are untangled and individually dissolved in the above solvents. The diluted solution was then spin-coated on piranha-cleaned silicon substrate or flame-annealed gold at 2000 rpm and one drop. The sample was then thoroughly dried in vacuum chamber before use. All solvents used in sample preparations are filtered with 0.2  $\mu\text{m}$  filters. For organic solvents, polytetrafluoroethylene (PTFE) filters were used; for aqueous solutions, cellulose filters were used. All organic solvents used in the experiments are checked to be compatible with the plastic used in the filter and syringe. For use in the fluid cell, the substrates are attached to the glass bottom of the fluid cell with slow dry epoxy glue. The epoxy is allowed to cure for 12 hours in a desiccator that is constantly vacuumed to get rid of evaporated solvents in the glue.

To verify that the hydrophobic polymer is indeed deposited on to the substrate, the contact angles of water on the substrate with different amount of polymer spin-coated were measured (Figure 5.4). Higher contact angle indicates greater hydrophobicity, as water tries to minimize the expensive interfacial area. Spin-coating with 1, 2, and 3 drops of PS solution in THF on gold substrate revealed an increasing contact angle. This indicates that polymer material is deposited onto the surface with each additional drop

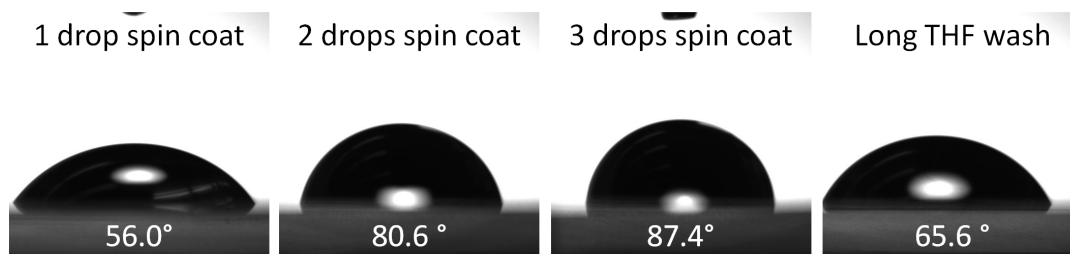


Figure 5.4: Contact angle change with different number of drops PS solution on Au surface, followed by a wash with solvent THF. The numbers at the bottom are the contact angle.

of PS solution, as additional drops increase the surface coverage of PS. A subsequent washing step with pure THF, removes loosely bounded polymers on the surface, thereby dropping the contact angle. This contact angle change from deposition and washing steps is strong evidence that the surface hydrophobicity change is due to PS deposition, rather than surface modification by THF.

## 5.4 Evidence of single chain unfolding due to hydrophobic hydration

The most important aspect of single molecule force spectroscopy experiment is to determine the signature of the single molecule events. In the case of multiple-domain protein unfolding experiments, the regularly spaced force rupture events is the signature that one such protein being pulled, as each rupture corresponds to the unfolding of one domain (Figure 5.5). However, the force curves for the unfolding of a hydrophobic polymer does not exhibit regular patterns that directly suggest single chain pulling.

To complicate the problem, plateaus in force-extension curves have been observed in a number of polymer-pulling experiments. Depending on the polymer, two mechanisms could lead to force plateaus [155, 168, 36, 80, 81, 108, 43, 2, 158]. The first mechanism is due to mechanically induced polymer solvation in poor solvents, which is the mechanism discussed in previous chapters [155, 168]. The second mechanism is due to polymer-surface interaction (Figure 5.6): an extended polymer can be adsorbed onto a surface and form a train-like structure [36, 80, 81, 108, 43, 2]. The force plateau arises from peeling the polymer away from the surface, as the total adhesion energy is proportional to the polymer length. The adsorbed polymer can only retain an extended conformation on the surface in good solvent [36]. Reports on such train-like structures usually comes from charged polymers, hence the desorption force is sensitive (change up to two orders

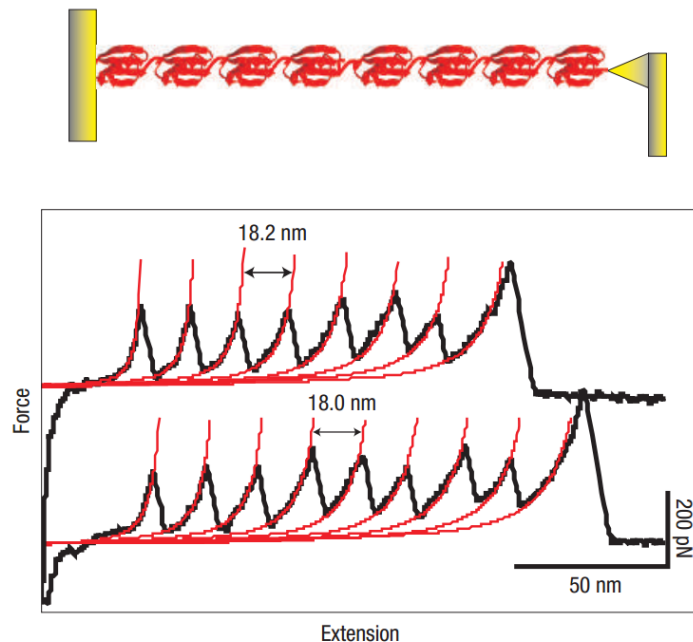


Figure 5.5: Mechanical unfolding of a multiple-domain protein reveals equally spaced unfolding peaks. (Figure adapted from Cao and Li [28].)

of magnitude) to small changes in the ionic concentration (in 5 to 100 mM range) as well as surface type [80, 81, 43, 158]. The following sections provide evidence for hydrophobic hydration as the mechanism for the plateau seen in this study. In addition, the evidence for single molecule events are identified.

#### 5.4.1 Surface topography of a single polymer

The polystyrene we studied are in poor solvents, therefore, it is unlikely that polystyrene assumes an extended state on the surface. A surface topography scan of sparsely deposited polystyrene (Figure 5.7a&c) confirms that individual polystyrene molecules are indeed in their collapsed state with an average height of roughly 4–5 nm (Figure 5.7b&d), which is similar to the diameter of a single collapsed polystyrene at 7.3 nm as calculated from the specific volume of polystyrene below its glass transition temperature  $T_g$  [51, 109]:

$$v = v_g - 2.5 \times 10^{-4}(T_g - T) \quad (5.3)$$

$$v_g = 0.943 + 2.4 \times 10^{-4}T_g \quad (5.4)$$

$$T_g = 100 - 1.7 \times 10^5/M \quad (5.5)$$

where  $v$  (mL/g) is the specific volume of the polymer at temperature  $T$  ( $^{\circ}\text{C}$ ),  $v_g$  (mL/g)

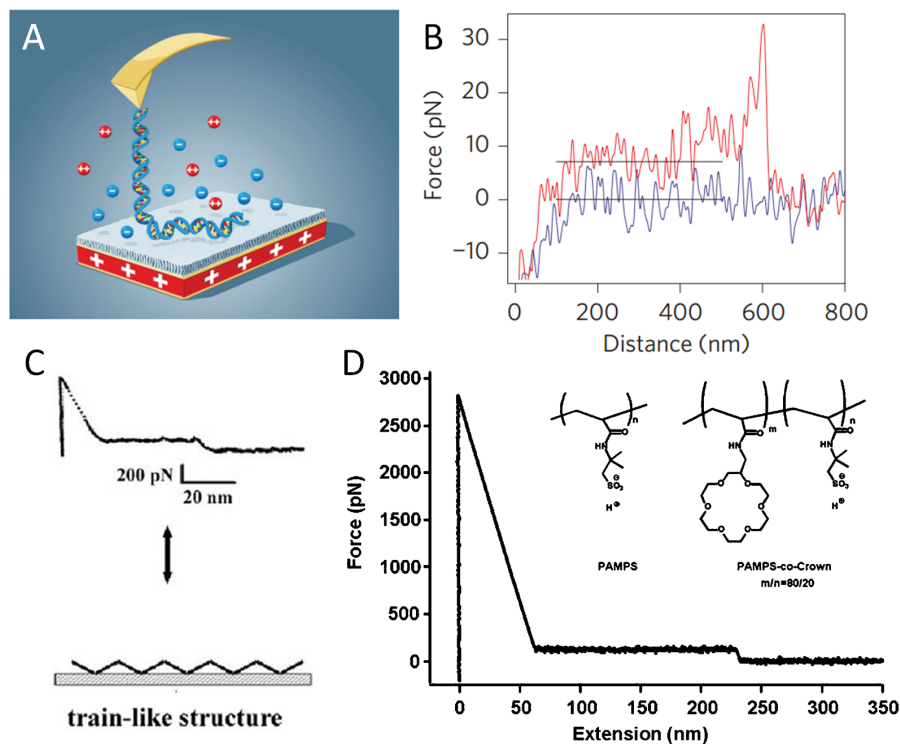


Figure 5.6: The alternative mechanism that can give rise to force plateau profiles. A. Surface adsorbed DNA being peeled off by AFM. B. A force curve showing  $\sim 7$  pN force plateau as a result of DNA desorption from OH-SAM. C. A polymer can form “train-like” extended conformations on the surface, the force is due to adhesion energy between the polymer and the surface. B. An example of a force curve from PAMPS. (Figure adapted from Erdmann et al. [43], Liu et al. [108], and Zhang et al. [185].)

is the specific volume at glass transition temperature  $T_g$  ( $^{\circ}\text{C}$ ), and  $M$  is the molecular weight. The width of each dot is roughly 20 nm (Figure 5.7d) due to surface features convoluted with tip radius (average of 13 nm according to manufacture specification); the width after deconvolution is on the order of 5–10 nm, consistent with the height measurement. The uniformity in height and the size of the dots suggests that these are single polystyrene molecules in their collapse states on the Si surface.

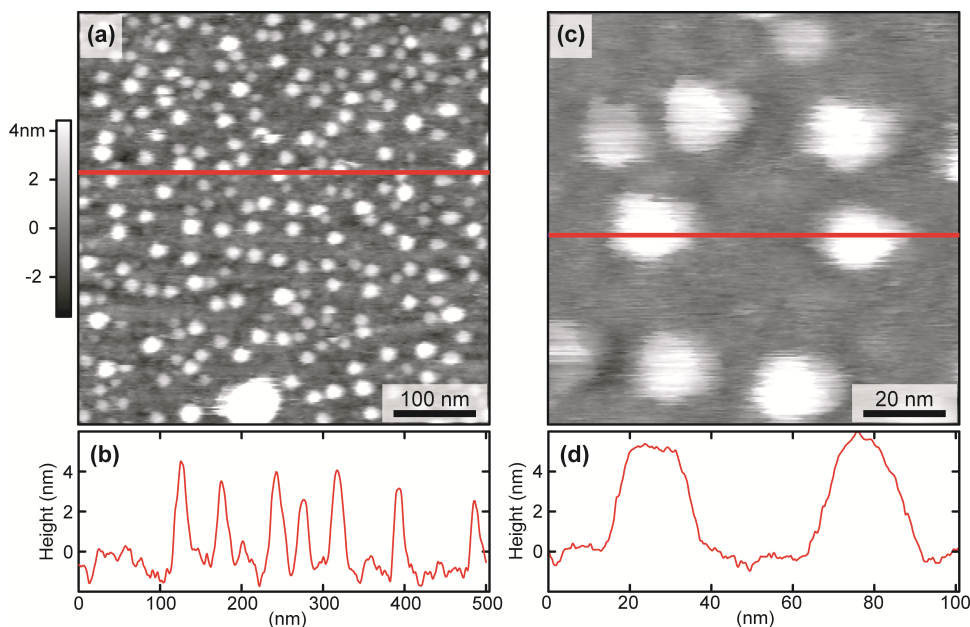


Figure 5.7: Surface topography of polystyrene deposited on Si surface. (a) Surface topography of a  $500 \times 500$  nm area. (b) Cross section profile of the white dashed line in (a). (c) Surface topography of a  $100 \times 100$  nm area. (d) Cross section profile of the white dashed line in (c).

All hydrophobic homopolymers in this study, such as polystyrene, are not charged; therefore, they should not respond directly to the ionic strength of the solvent as charged polymers do. The increase in plateau force at higher salt concentration (See Section 7.4) is therefore, a result of the increased solvent-solvent interaction, in line with the mechanism of solvating hydrophobic polymer in poor solvents.

Polymers that do not collapse in solvent can form train-like structures when adsorbed onto the surface. In this case, polymer-surface adhesion force immobilizes extended polymer, such as DNA molecules on a mica surface (Figure 5.8), thereby preserving the extended conformation [164]. Pulling surface adsorbed DNA molecules also produce plateau forces<sup>8</sup>, however the mechanism is evidently due to peeling the molecule from the surface. The initial collapsed conformation of hydrophobic polymers on hydrophilic Si surface is significantly different from a train-like structure. Hence the force plateaus

is more likely to be a solvent induced effect rather than polymer-surface interaction.

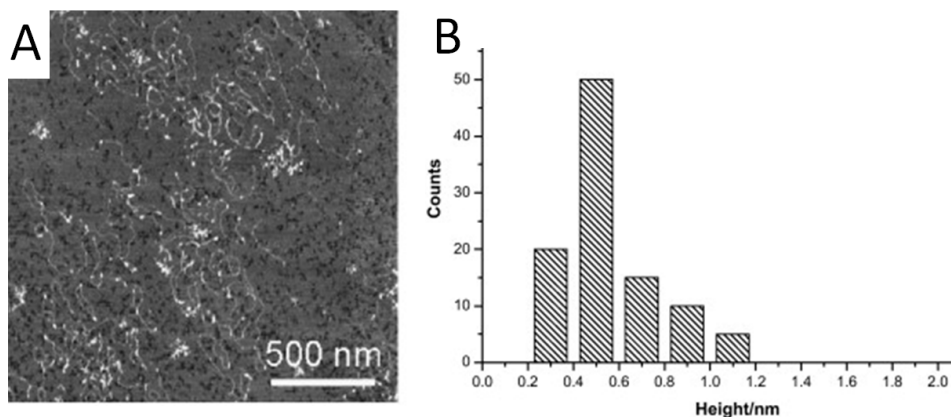


Figure 5.8: DNA adsorbed on mica surface. A. AFM topography scan. B. histogram of DNA height on surface. (Figures reproduced from Sun et al. [164].)

### 5.4.2 Surface independence of plateau force

The plateau force observed in this report was found to be insensitive to the surface properties. Experiments performed on silicon (Si) and gold (Au) surfaces using silicon nitride ( $\text{Si}_3\text{N}_4$ ) and gold-coated AFM tips showed no differences in the magnitude of the force plateau (see Table 5.1). Similarly, Thormann et al. showed in an experiment that pulling polystyrene beads from hydrophilic and hydrophobic surfaces [168] does not produce any differences in the plateau force, which further confirms that the plateau force is surface independent and is due to polymer-solvent interactions only. The force plateau magnitude in our study is dependent only on the solvent condition, which further confirmed the force plateau is the result of solvating polymer in poor solvents.

Tip-surface	Force plateau (pN)
Au-Au	$76 \pm 10$
$\text{Si}_3\text{N}_4$ -Au	$81 \pm 16$
$\text{Si}_3\text{N}_4$ -Si	$81 \pm 13$

Table 5.1: Force plateau magnitude using different tip-surface combinations

### 5.4.3 Step size distribution of multiple force plateaus

Depending on the tip curvature and the single molecule density on the surface, multiple polymers can adsorb onto the AFM tip. The step-by-step detachment of the polymers as

the AFM tip pulls away from the surface gives rise to multiple force plateaus (Figure 5.9, Figure 5.10).

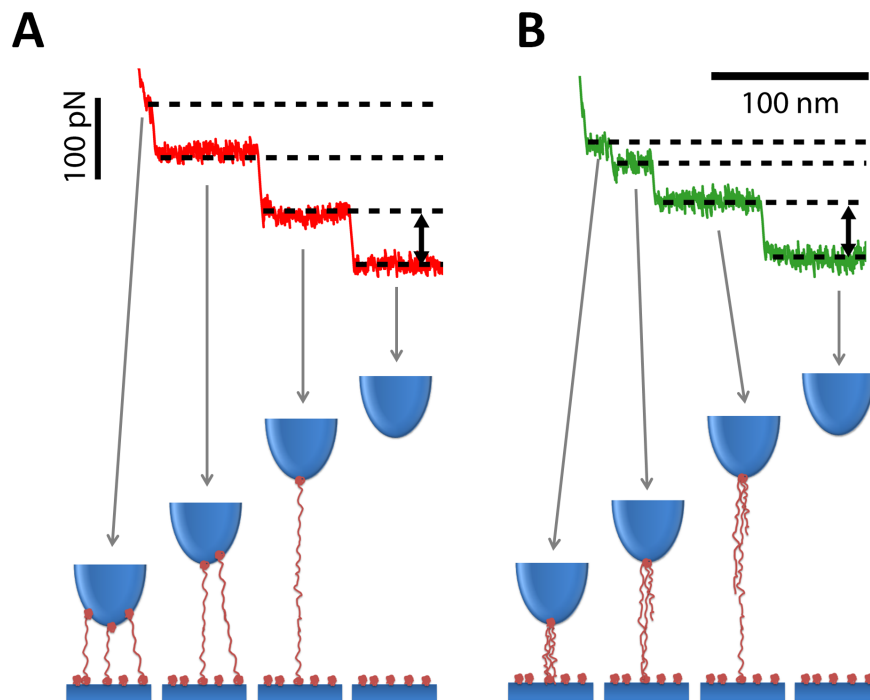


Figure 5.9: Step size distribution showing A. uniform and B. non-uniform plateau step height distributions. The mechanism behind the uniform distribution is simultaneously pulling on multiple non-interacting chains; whereas the mechanism behind the non-uniform distribution is pulling interacting chains.

In unfolding experiments of hydrophobic polymers used in this study, multiple plateau force curves exhibit two step height distributions. The first type shows plateaus with uniform step height, which is indicative of multiple non-interacting chains are being pulled simultaneously [168] (Figure 5.9). When the chains do not interact, the total force exerted on the cantilever is proportional to the number of chains (Figure 5.9 & Figure 5.10D), giving rise to identical step sizes between multiple plateaus (Figure 5.10B) [168]. The second type shows force plateaus with non-uniform step heights, which can be described by a model where multiple polymer chains interact to form a bundle while being pulled into the solvent [155] (Figure 5.9 & Figure 5.10A, C). The interacting hydrophobic chains bundle together, resulting in smaller solvent accessible surface area than the sum of the individual chains (Figure 5.10C) [155]. Therefore, as more chains bundle together, the effect of each additional chain added to the bundle exerts less and less force (Figure 5.10A).

Although force plateaus can be generated from either the hydrophobic hydration mechanism or the polymer-surface interaction mechanism, the latter mechanism can only

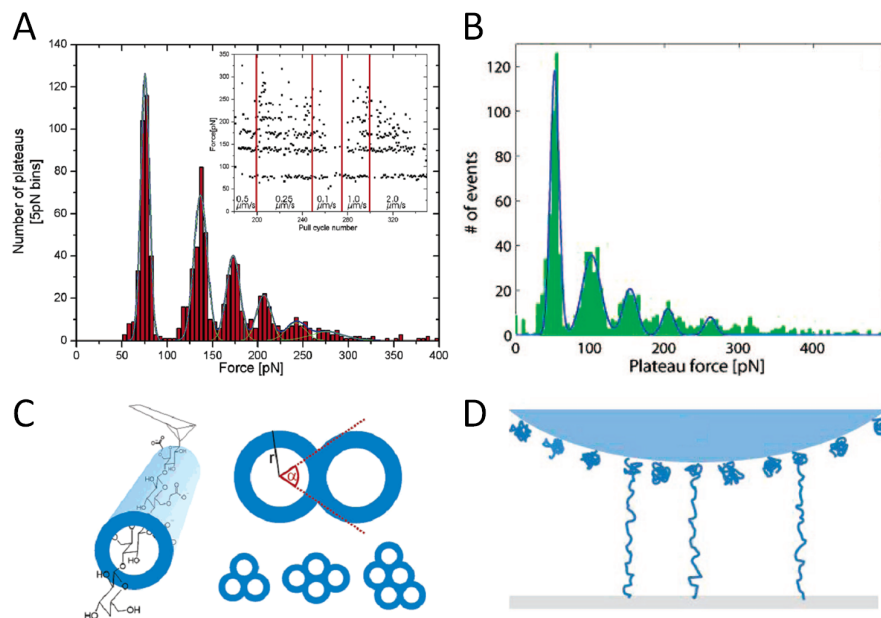


Figure 5.10: Mechanism behind non-uniform (A, C) and uniform (B, D) step size distributions. Non-uniform step sizes are the result of inter-chain interactions, while non-interacting chains are responsible for uniform steppings. (Figures adapted from Thormann et al. [155, 168].)

produce multiple plateaus of identical height differences. The non-uniform step size is a signature reserved only for the mechanism of polymer bundle hydration. Therefore, the coexistence of uniform and non-uniform plateau steps suggests that the force plateaus in this study are solely due to the hydration of hydrophobic chains (Figure 5.10) [155, 168].

#### 5.4.4 Consistent last force plateau marks unfolding of a single chain

Under the same condition, all force curves showing polymer pulling events (either uniform or non-uniform step heights), one common feature emerges: the height of the last force plateau from the force baseline are identical. Overlapping hundreds of force curves show the last force plateau separated from the baseline force (Figure 5.11 and Figure 6.10). The absence of force curves between the force plateau and the baseline suggests the force plateau corresponds to single chain pulling events. Such discrete distribution of force plateau is typical for all hydrophobic homopolymers under all conditions in this study. The distributions of both the last plateau and the baseline are Gaussian (Figure 5.11); the Gaussian peak-to-peak difference is the value of plateau force quoted in later chapters.

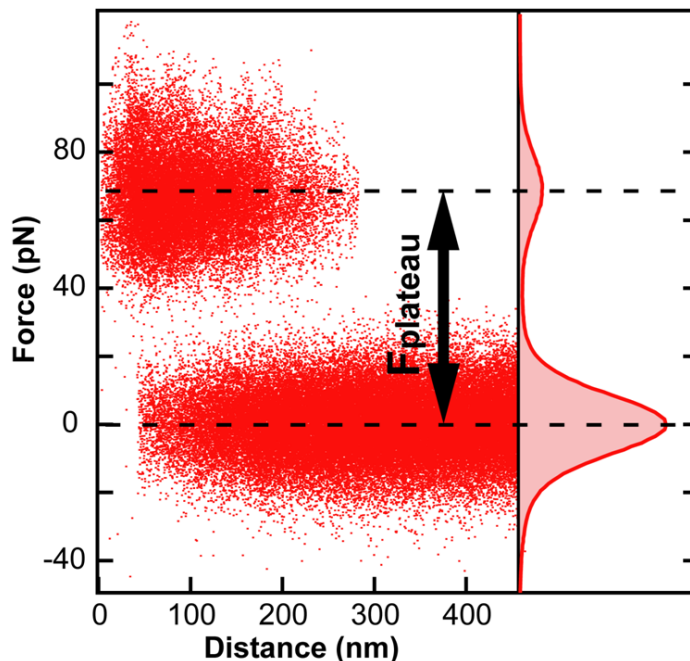


Figure 5.11: Superposition of 100 independent PVBP force curves with single chain pulling events at 25°C. The lower and upper traces correspond to baseline and force plateau from single chain pulling events, respectively.

### 5.4.5 Normalization of contour length

For the force curves that exhibit an entropic elastic response before rupture, their contour length can be extracted from a WLC fit (Section 4.1.2). Each force curve can then be normalized by their contour length and plot force against the percentile extension. After such normalization, all force curves can be superimposed on top of one another (Figure 5.12). This is an indication of two things: one, regardless to the length, all chains have the same persistence length; and two, the physics behind the forced hydration is length independent within the range of polymer sizes accessible to our experiment (hundreds of nm). The identical persistence length is an evidence for single chain pulling events.

### 5.4.6 Length distribution of the last force plateau

In multiple-domain protein unfolding experiments, the increased contour length of each unfolding event is precisely the length of the protein because each domain is pulled by its ends (Figure 5.5). Even though the AFM tip may not pull on the exact ends of the chain, the multiple protein domains between the tip and the surface provides the single molecule pulling data. However, it is experimentally difficult to pull at the ends

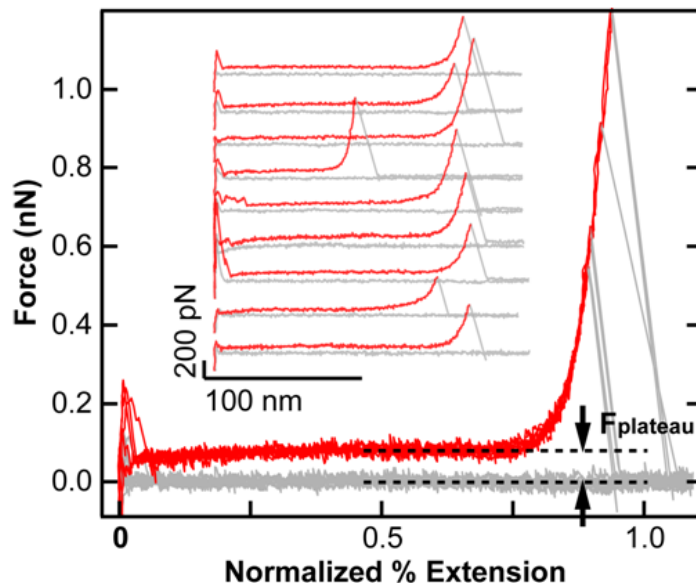


Figure 5.12: Contour length normalized force-extension curves are well superimposed, showing that globule-coil transition phenomenon probed here is independent of polymer length in the regime accessible to these experiments.

of a single unstructured polymer globule. Even with chemical modifications, only one end of the polymer can be tethered to either the surface or the AFM tip. Furthermore, physisorption cannot be avoided; its effect may be indistinguishable from the effects due to chemical modification. The experiments in this study relied on physisorption for polymer attachment. Therefore, the adsorption point is randomly distributed along the chain. The distribution of the rupture length (Figure 5.13) shows a decay of towards the expected polymer length. Only few force curves show total force curve length greater than the expected polymer length, likely due to polydispersity of this polymer sample ( $M_w/M_n = 1.08$ ). The sharp drop-off towards lower molecular length is due to tip-surface snap off events and software cut offs (See Section 6.4), where shorter molecular lengths are systematically removed from the analysis. This distribution is evidence that the polymer being pulled is indeed the polymer that was deposited onto the surface.

#### 5.4.7 Reversibility and velocity independence of plateau force

To see whether the force plateau exhibits any sort of energy barrier crossing process, constant velocity pulling experiments at different pulling velocities were accomplished. Hundreds of force-extension curves for each pulling velocity were recorded. The force curves are then overlapped to generate a histogram of forces through the entire force-curve trajectory. By multiple peak fits with Gaussians, three major force populations

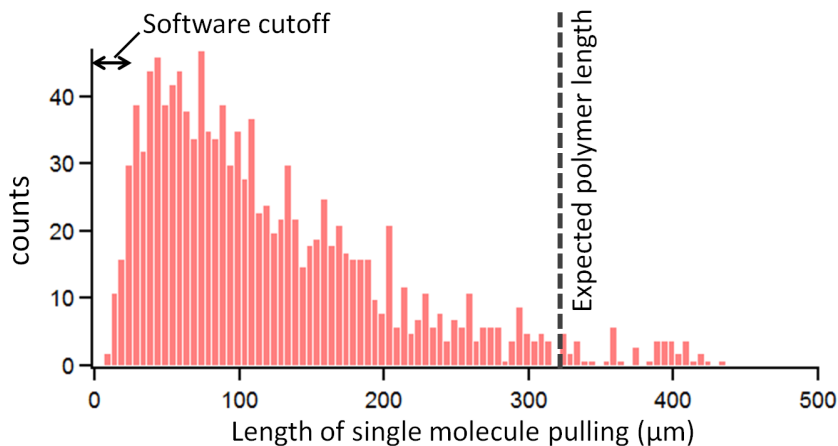


Figure 5.13: Single molecule pull length distribution of polystyrene with  $M_w = 131$  kDa, which is expected to be 321 nm in contour length.

were identified, coming from: 1. cantilever approaching the surface, 2. pulling on a single chain, and 3. retraction of the tip after the polymer desorbs from the tip. The first and third force populations are forces due to the hydrodynamic drag of the AFM cantilever. The force difference between the approach and retraction increases linearly with the pulling velocity. The linear dependence of the two also indicates that the water flow around the cantilever is laminar, giving minimal turbulence to the system. When a single chain is pulled, because a force plateau region is reached, the velocity of the cantilever is the same as after the polymer desorbs from the cantilever. Hence, the hydrodynamic contribution in this region of the force curve is equal to that during the free retraction. To see whether there is a pulling velocity dependency, the free retraction was chosen as the reference force and plotted the magnitude of the forces against pulling velocity. Figure 5.14 shows that both force populations that correlate to single and double chain pulling are constant through the range of velocity.

Activated barrier crossing processes were not observed in these experiments performed at constant room temperature (300 K). If the process were to involve cantilever force driven barrier crossing events, a larger plateau force, or even random sawtooth pattern, would be expected as the pulling velocity is increased. This has been well explored and documented in protein unfolding and dissociation of binding partners [119, 186, 45]. Unlike protein unfolding where a significant energy barrier is crossed going from folded to unfolded state, the free energy landscape of extending polystyrene in poor solvents seems to be monotonically increasing. However, one could imagine that it is possible that the free energy landscape is rugged due to the hydration energy of each polymer unit as each is being pulled out of the collapsed globule. This barrier does not exist

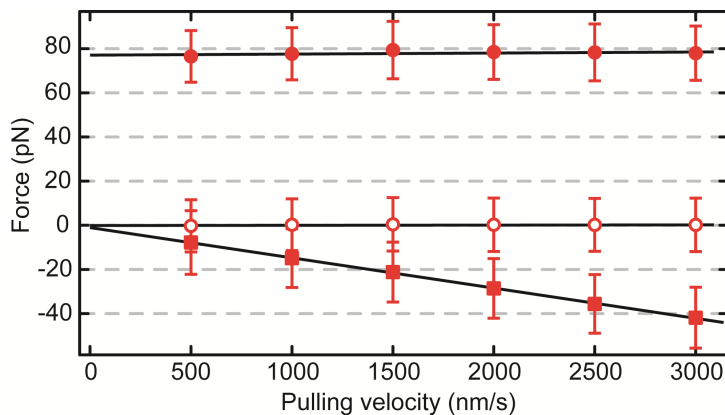


Figure 5.14: The force plateau magnitude (solid circles) is velocity independent from 500 to 3000 nm/s. The retraction portion (hollow circles) of the force curves are zeroed as the reference because the cantilever is moving at the same velocity in the same direction in this region as the force plateau region. The hydrodynamic drag of the cantilever can be clearly seen from the surface approaching portion (solid squares) of the force curve. Solid lines are linear fits to each of the three data sets. There is no apparent velocity dependency of the force plateau magnitude within the margin of error. Also note the linear dependency of hydrodynamic drag to velocity, indicating the flow of solvent around the cantilever is laminar.

in the continuum model for polymer that looks like spaghetti. However, if one were to consider the polymer made of finite size beads and each bead were exposed to the solvent in an on/off fashion, then a small finite barrier would exist per monomer. These small barriers contribute to a staircase-like roughness on the overall monotonically increasing energy landscape as the grey line illustrated in Figure 5.15. The linear spring constant of the AFM cantilever gives rise to a parabolic energy landscape (Figure 5.15, dashed line). When the polymer system is coupled to the AFM cantilever, the energy landscape of the system is the sum of the previous two (Figure 5.15, black line). This shifts the systems energy minimum to a lower end-to-end distance from the cantilever's intrinsic equilibrium position, which is interpreted as the deflection of the cantilever. Due to the roughness on the polymer's own energy landscape, there will be roughness at the bottom of system's energy landscape, which is populated according to Boltzmann's distribution. Therefore, as long as the lowest energy states are populated much faster than the rate at which the cantilever pulls on the polymer, i.e.  $v_{hop} \gg v_{pull}$  (Figure 5.15) there will be no observable force dependency on the pulling velocity that is caused by the roughness of the energy landscape. The barrier height is roughly  $1.1 k_B T$ , which is close enough to the thermal noise floor, and allows a fast hopping rate from one minimum in the energy landscape to an adjacent one.

The pulling velocities ranging from 500 to 3000 nm/s in these experiments are prob-

ably too slow to accelerate barrier crossing events. The time scale required to see the dependence of force on velocity would depend on the diffusion constant of the polystyrene in solvent as well as the barrier height (in this case, the solvation free energy per monomer).

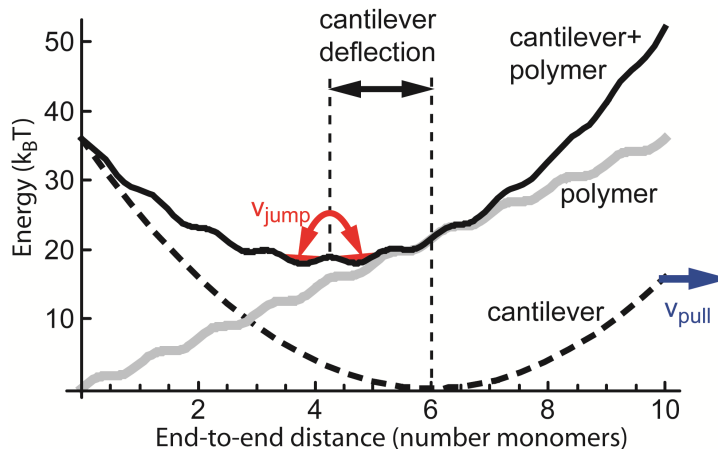


Figure 5.15: Schematic of the energy landscape of the polymer, the AFM cantilever and the polymer-cantilever system along the coordinate of end-to-end distance of the polymer. The end-to-end distance of the polymer equals the surface-tip distance of the AFM cantilever when the polymer is attached to the tip.

The time scale of the pulling experiment is slower than the self-organization time scale of the collapsed state. The portion of the polystyrene in the collapsed state has enough time to rearrange itself to avoid self-entanglement or is initially not entangled. Supposing that the collapsed state of polystyrene could not rearrange fast enough compared to configurational changes induced by the pulling, we would unavoidably pull entangled polystyrene out of the collapsed state. The force-extension profile of such events would neither have a constant force profile due to trapped states, nor be velocity independent due to friction between polymer chains. The behavior of such a scenario would be similar to plastic deformation. Lastly, the velocity independence also excludes the possibility that the force plateau is due to hydrodynamic friction between the polymer and the solvent. Any friction between polymer and solvent is due to hydrodynamic drag, which would exhibit a pulling rate dependency. All the above evidence further suggests that the behavior of the polymer system is due to a conformation transition from collapsed state to extended state in poor solvent and that the magnitude of the extension force is a result of the solvent condition.

To test the reversibility of the pulling, “fly-fishing” method was used. In fly-fishing, the AFM tip cycles back and forth without touching the surface or breaking contact with the molecule. Many systems show hysteresis such as protein unfolding and refolding. However, the force curves for hydrophobic polymer unfolding do not show any hysteresis,

indicating that the process is reversible. Furthermore, it indicates that the experimental time scale is much greater than the dynamics of the chain; hence the system is constantly in equilibrium with its surroundings.

## 5.5 Conclusion

In this chapter, the experimental basis for studying the hydrophobic hydration of a single hydrophobic polymer was established. Two critically important experimental aspects were examined. One is the test for the signature of single molecule event. The other is to verify the nature of the single molecule event, that is, whether it is caused by hydrophobic hydration of a single chain. The following three evidences suggest that a force plateau around 70–80 pN corresponds to the stretching of a single chain. First, the last force plateaus before the final rupture events always have the same height, the existence of a Gaussian distributed minimal force well separated from the baseline indicates that it is from a single chain. Second, force curves that show multiple uniform steps have step sizes equal to the height of the last force plateau, indicating the lowest force quantization comes from a single chain. Three, all entropic elastic stretching shows identical persistence length, possible only with a single chain.

Two mechanisms, namely single chain hydration and polymer-surface interaction can give rise to the force plateau. The following evidences suggest that the force plateau is the result of polymer chain hydration rather than polymer-surface adhesion: First, the hydrophobic polymers form globular structures rather than extended chain-like structures, which can give rise to plateau forces due to polymer-surface adhesion. Secondly, studies on different surfaces (gold, silicon, and mica) show identical forces, indicating the process is surface independent, and cannot be polymer-surface interaction. Lastly, the step size distribution of multiple step plateaus showed two distributions, and only the hydration mechanism can explain the coexistence of both uniform and non-uniform spacing of plateau forces.

These evidences are true for all hydrophobic homopolymers used in this study as the only difference between these polymers is the size of the hydrophobic side chain.

# Chapter 6

## Single Molecule Data Analysis

In single molecule experiments, analyzing single molecule data is as important as collecting these data. Single molecule events in force spectroscopy do not occur frequently; often less than 1% of the collected data contains single molecule events. Therefore, force curves containing high quality single molecule events need to be filtered from the vast amount majority of raw data that contain no single molecule events. For instance, a statistically significant data set should contain a few hundred single molecule force curves, which would require the number of raw force curves to be on the order of tens of thousands. Automated programs can replace laborious manual filtering of such large dataset. In addition, automated programs based on a set of selection criteria are far more objective than human eyes and could bypass bias due to human subjectivity.

Besides automated filtering, force curves often need to be conditioned before analysis. The AFM system is prone to interferences from the detection laser and drifts from thermal / mechanical sources, which can severely bias subsequent analysis. This chapter describes methods to automatically detect and correct for such imperfections in the force curves. Force curves after data conditioning are ready for further statistical analysis. Lastly, methods to analyze force curves with both force plateau and entropic elasticity responses are described in detail.

### 6.1 Automated data analysis program design

All programs are written in Igor Pro 6.1 (Wavemetrics Inc.), the native operating environment of the Asylum Research AFMs. This efficiently integrates data collection and analysis, giving immediate feedback on the data collection. In addition, settings and environment parameters recorded in the native Igor Binary Wave (.ibw) files can be easily extracted without file conversion. The programming environment in Igor Pro is simi-

lar to C language and is equipped with extensive mathematical and statistical analysis libraries, making it an ideal development environment for analysis.

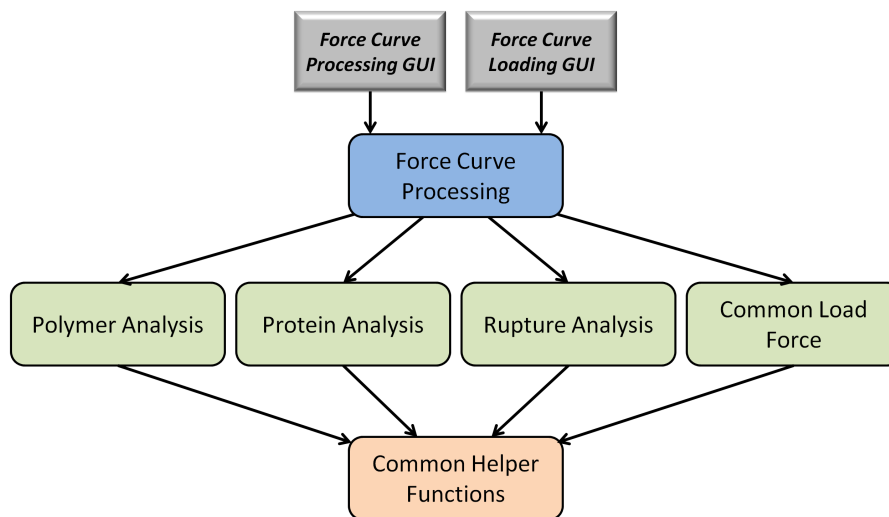


Figure 6.1: Program structure. An arrow pointing from module A to B indicates that module A uses resources from module B.

The program contains 6 modules (Figure 6.1), each containing functions for a specific type of analysis. Two graphical user interfaces (GUI) rely on higher level control functions in the force curve processing module, which oversees the loading (common load force module), conditioning (common load force module) and analysis (polymer, protein and rupture analysis modules) of force curves. All of the above modules then rely on a set of common mathematics, string processing and curve-fitting functions in the common helper functions module. The modular design ensures that future improvements and modifications on each module do not affect the rest of the program. In addition, individual modules can be loaded to specific applications, which is generally a good programming practice.

The flow program can be divided into three phases, responsible for force curve conditioning, filtering, and analysis (Figure 6.2). The force curve conditioning phase corrects for any imperfections in force curves caused by optical, thermal and mechanical drifts and instabilities. Each force curve is loaded into the memory from an .ibw file with force, deflection and z-sensor data split into separate waves (a wave is an array of data in Igor Pro). The loaded force curve is first pre-conditioned to correct for invOLS, the force offset, and the tip-surface distance offset. Then, the rupture points along the retraction portion of the force curve are detected, which partitions the force curve into segments containing individual force plateaus or entropic elastic curves. At this stage, the baseline from both approach and retraction are also isolated, any tilt caused by laser

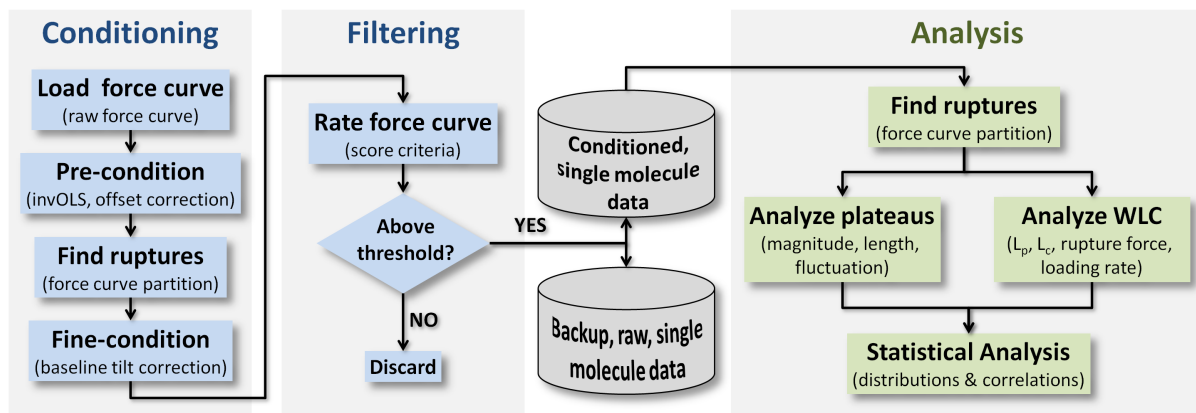


Figure 6.2: Program flow diagram. The force curve fitting procedures on the left intakes raw, unfiltered force curves to be conditioned and scored to determine the ones that contain single molecule events. The resulting conditioned force curves are stored in memory to be further analyzed. The corresponding original force curves are stored separately for backup. The force curve analysis procedures takes conditioned single molecule force curves to process as either force plateaus or entropic elastic pulls. Statistics from the analysis of each force curve are collected.

interference with the surface and long-range tip-surface interactions are corrected in the fine-conditioning step.

Once a force curve is thoroughly conditioned, a score is assigned to indicate its quality. Depending on the study, different scoring systems are used. Take hydrophobic polymer unfolding for example, if we specifically want force curves that contain only one plateau, the scoring system would be designed by summing up the following conditions:

- Presence of any molecular events:
  - Yes: 1
  - No:  $-100$
- Molecular event length (this score favors longer events over short pulls, it is more accurate to determine the shape and statistics of longer events)
  - $< 15$  nm: 0
  - 15–30 nm: 0.5
  - 30 nm: 1
- Absolute plateau height (the standard deviation of the last plateau force does not exceed  $75 \pm 15$  pN)

- 50-100 pN: 1
- $> 100$  pN or  $< 50$  pN: 0
- Force standard deviation of the plateau (in events of contaminations, the molecular event may not be a plateau, a plateau has the lowest force standard deviation among any force profiles)
  - Force standard deviation  $< 1.2$  baseline standard deviation: 1
  - Force standard deviation  $< 1.5$  baseline standard deviation: 0.5
  - Force standard deviation  $> 1.5$  baseline standard deviation: 0
- Number of force plateaus (in the event multiple chains are pulled at once)
  - 1 plateau: 1
  - 2–3 plateaus: 0.5
  - $> 3$  plateaus: 0

Any molecular events satisfying the most desirable conditions in all 5 criteria would have a score of 5; missing in one less crucial condition gives 4.5, etc. Therefore, a threshold value can be placed to filter out desirable force curves. One can assign even more elaborate scoring schemes to bin force curves with different characteristics into different categories. The same idea can be applied to sift through multiple-domain unfolding force curves where scores of unfolding domain size and the number of domains can be assigned. The automated filtering process is monitored using a GUI where force curves and the scores are displayed. This provides a live evaluation of how well the filtering process works and whether it is introducing any systematic bias. Once a good force curve is found, its conditioned copy is saved in an Igor Pro experiment file (.pxp); another copy of the original .ibw file is copied to a separate folder as backup.

At this stage, the number of filtered force curves is manageable and can be individually analyzed. The analysis code detects the precise location of each rupture segments and fit each force curve segment with the appropriate model. Information of each force curve segment is collected and statistical analyzed.

## 6.2 InvOLS correction

As shown in Section 3.3, invOLS is among the most critical values for force spectroscopy experiments as it dictates the measured force values. Figure 6.3 shows a force curve before

and after invOLS correction. The magnitudes of force before and after the correction are clearly different. Although invOLS is prone to drift over time (Section 3.7.2), the LVDT sensor built in the z-piezo provides a standard to calibrate the invOLS in every force curve, given that an indentation onto a hard surface is performed.

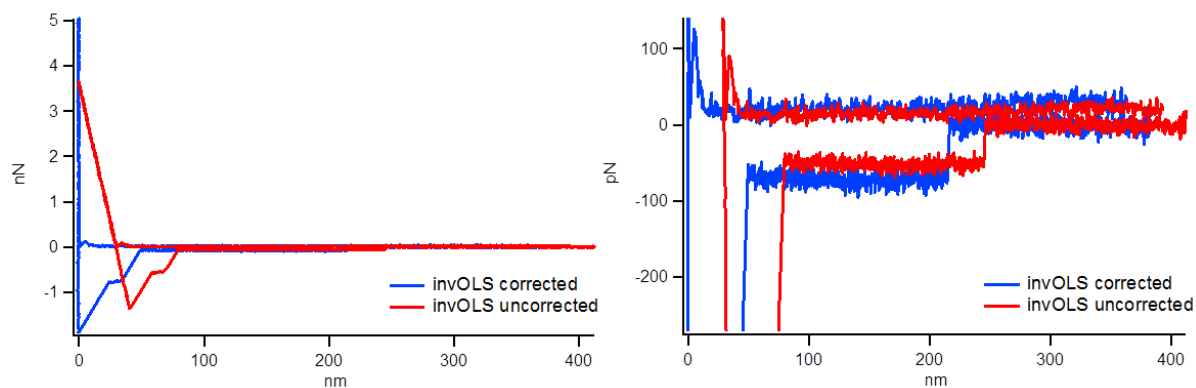


Figure 6.3: invOLS corrected (blue) and uncorrected (red) force curves, plotting force against tip-surface separation.

The first step to correct for invOLS is to determine the indentation portion of the force curve. The beginning of the indentation in the retraction portion of the force curve is marked by the point with maximal cantilever deflection. The end of the indentation is marked by the first point following the max indentation where the deflection drops to zero (Figure 6.4B). The corresponding portion of the z-piezo sensor curve provides the exact distance the tip deflects. A correction factor can be applied to the deflection such that deflection matches z-piezo sensor readings during the indentation. A tip-surface separation that remains zero during indentation indicates that invOLS and deflection are properly calibrated (Figure 6.4A).

### 6.3 Baseline tilt correction

A number of causes contribute to the linear tilt in the force curve baseline include electrostatic interactions and optical interference. Long-range electrostatic force from a charged surface can be felt by the cantilever many microns away. The electrostatic force is distance dependent and linear in most cases. The effect is strongest in air, and is greatly reduced when experiments are performed in aqueous solutions. However, in the majority of cases, the baseline tilt is caused by optical interference, as changing the detection laser alignment affects the slope of the tilt. This happens when the AFM cantilever is too small to contain the laser spot such that part of the laser can reflect off the substrate

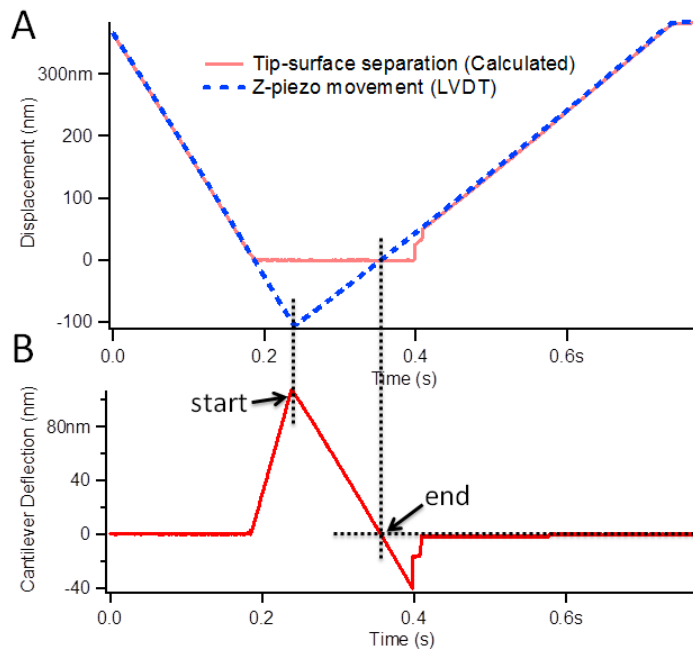


Figure 6.4: Identifying the indentation portion of force curve. Individual trajectories (data vs. time) of A. Z-piezo movement, tip-sample separation, and B. cantilever deflection. The dotted lines mark the start and end of the retraction portion of the indentation curve. The tip-surface separation remains at 0 during the indentation.

onto the photo diode and interfere with the cantilever reflected signal. The result of this is a nearly linear tilt in the cantilever's deflection as a function of distance from the surface (Figure 6.5A). Although this can often be corrected by adjusting the position of the laser spot or the angle of the AFM cantilever with respect to the surface, any slightest tilt may cause systematic errors to the magnitude of the AFM measurement, especially when high precision is required. Because the tilt is superimposed onto all other force features, i.e. a force plateau would have the same tilt (Figure 6.5A). We can recover the real force curve by subtracting the tilt from all force curves:

$$F_{real}(d) = F_{obs}(d) - \alpha d \quad (6.1)$$

where  $F_{real}(d)$  is the real force curve profile,  $F_{obs}(d)$  is the observed force curve,  $\alpha$  is the slope of the baseline tilt, and  $d$  is the tip-surface distance. Both the approach curve and the baseline of the retract curve can provide the tilt slope. The recovered real force curve is shown in Figure 6.5B.

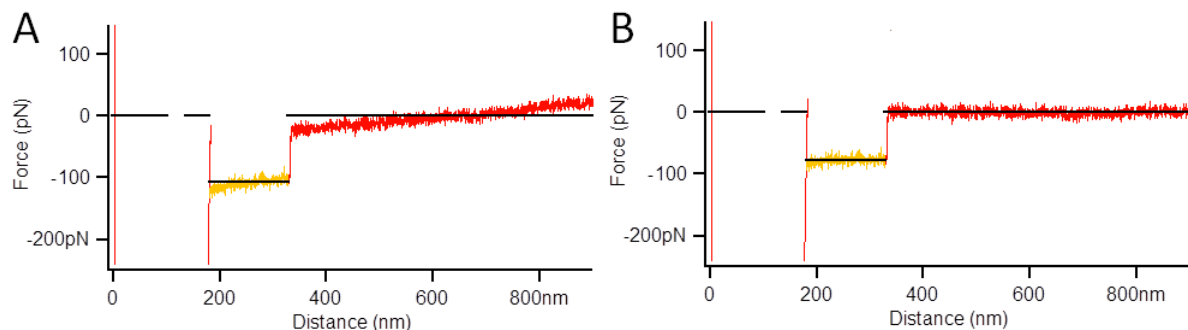


Figure 6.5: Force curves before baseline correction. Before (A) and after (B) baseline correction. Retraction force baseline is colored in red, the plateau force for a single molecule event is colored in yellow. The black curves show the mean value of each portion, which also shows as a horizontal guideline. The tilt correction fixes tilts in both the force plateau and the baseline.

## 6.4 Rupture point detection

The separation (unbinding) of a single molecule from the tip results in a rapid relaxation of the deflected cantilever, shown in a force curve as a sudden drop in force (Figure 6.6). Detecting such event is critical to determine the force curve segment containing the single molecule pulling event. Two detection schemes: the differential detection and the hypothesis test detection are outlined here.

### 6.4.1 Differential detection

By taking the differential of the force trajectory over time, an edge in the force trajectory corresponds to a peak in its derivative (Figure 6.6). These peaks above the noise floor can be found by scanning through the force derivative and detecting values above a threshold. This simple method works well for large and rapid force transitions. For typical pulling experiment with 1m/s pulling speed and 5 kHz sampling rate, the rupture from 80 pN to 0 pN is clearly visible to the naked eye (Figure 6.6B). The force derivative at the rupture point is approximately 6 times greater than the baseline derivative standard deviation, but only 2 times greater than a handful of points at the extrema of the Gaussian distributed force derivative (Figure 6.6B). As the rupture force decreases, one would expect a higher rate of false positive detections simply because the true event lies closer to the edge of the Gaussian distribution. At approximately 40 pN, a reasonable rupture force for many molecular events, there could be as many as 10 false positive rupture detections within 0.1 s of force trajectory. To make the matter worse, at higher pulling velocities, the cantilever cannot snap back to equilibrium position fast enough, which

will further decrease the sensitivity and specificity of this detection scheme. Therefore, the experimental conditions most suitable for this detection scheme are low pulling speed (less than  $\sim 2 \mu\text{m/s}$ , depending on the cantilever drag) and high rupture force (greater than 100 pN).

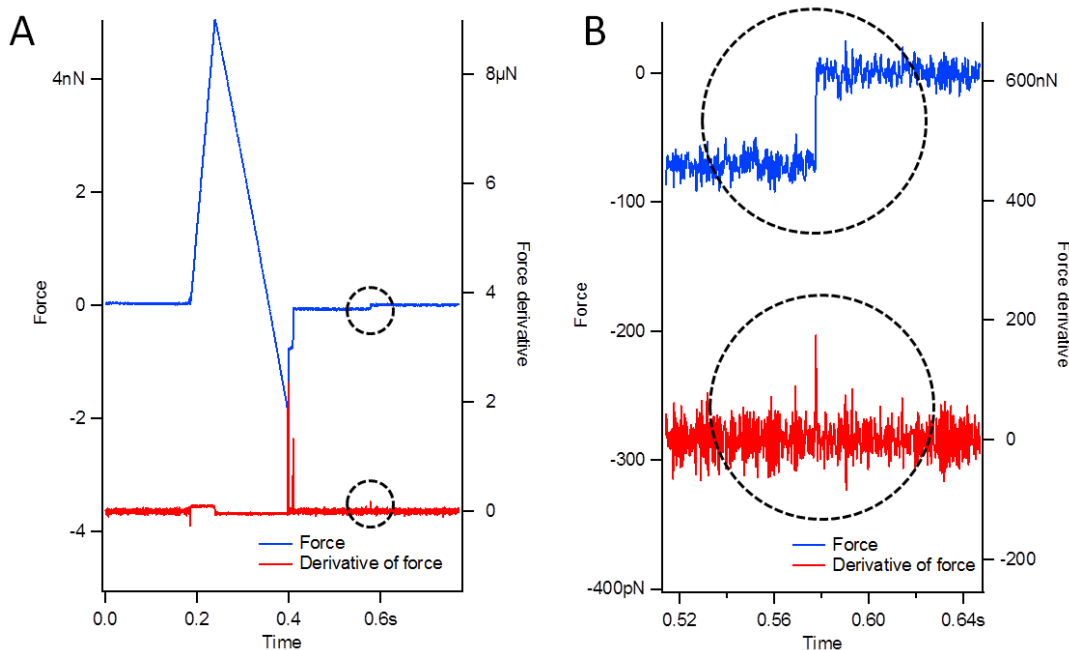


Figure 6.6: Force trajectory (blue) over time and its derivative (red). A. of the whole force curve, B. zooming into the single molecule rupture event. The condition of the experiment is:  $1 \mu\text{m/s}$  pulling speed and 5 kHz sampling rate.

## 6.4.2 Hypothesis test detection

The drawback of the differential detection includes lack of sensitivity and specificity, resulting in high false positive rate. This is because the differential detection only considers the local shape of the force curve (effectively, the two adjacent data points). In order to enhance the detection sensitivity and specificity, a hypothesis test detection scheme was used. The basic idea of this scheme is to assume there is one force transition within a force trajectory, and find the most probable location of this transition. The hypothesis is that a force transition occurs at time  $t$  on a force trajectory  $F(t)$  from  $t_1$  to  $t_2$ ; furthermore, before and after  $t$ ,  $F(t)$  have constant force profiles. The mean square score of the hypothesis is:

$$\delta = \sum_{t_1}^t \left[ F(t) - \frac{1}{t-t_1} \sum_{t_1}^t F(t) \right]^2 + \sum_t^{t_2} \left[ F(t) - \frac{1}{t_2-t} \sum_t^{t_2} F(t) \right]^2 \quad (6.2)$$

A lower  $\delta$  value indicates a better hypothesis. A test case was constructed where 3 plateaus were convoluted with Gaussian noise with a standard deviation of 1 (arbitrary unit). The step sizes are 0.5 and 0.7 respectively (Figure 6.7A). This is equivalent to a normal force curve measurement where the thermal noise has a standard deviation of 10 pN and the events are 5 to 7 pN. Such small transition events in the trajectory cannot be picked up by the previous differential method as Figure 6.7B shows the differential signal do not have any visible peaks around the transition points. Plotting  $1/\delta$  over the entire range, Figure 6.7C shows an unambiguous sharp peak at the 0.7 transition point. Recursively applying this algorithm to two segments it divides the trajectory into, the 0.5 transition point was identified (Figure 6.7D). Even though the value of  $1/\delta$  rises around the transition point, they never exceed the value at the transition point. More importantly, there is no false detection far away from the supposed transition point. Because of this property, the detection signal can be amplified to provide better signal to noise ratio. Taking the inverse exponential  $\exp(-\delta)$  provides an excellent amplification of the signal (Figure 6.7E, F). The locations of each transition point is pointed to by a single sharp peak from  $\exp(-\delta)$ .

The hypothesis test detection scheme requires knowledge of the expected force curves, in this case, force plateaus. Therefore, properly filtered and conditioned force curves are critical to this step. Tilts in the force plateau and baseline void the hypothesized curve shape. In a way, this method is similar to curve fitting to a step function with the transition point as a fitting parameter. The algorithm implemented in this study is able to detect multiple rupture events by recursively scan force segments partitioned by each transition until the transition threshold drops below a preset threshold. Due to the advantages of this detection scheme and the low false-positive rate, all force curves were analyzed using this algorithm.

## 6.5 Drag correction

Due to the viscosity of the solvent, the measured force ( $F_{measured}$ ) is the sum of force from molecular events ( $F_{molecule}$ ) and a linear velocity-dependent drag force:

$$F_{measured} = F_{molecule} + \frac{dz}{dt} \eta \quad (6.3)$$

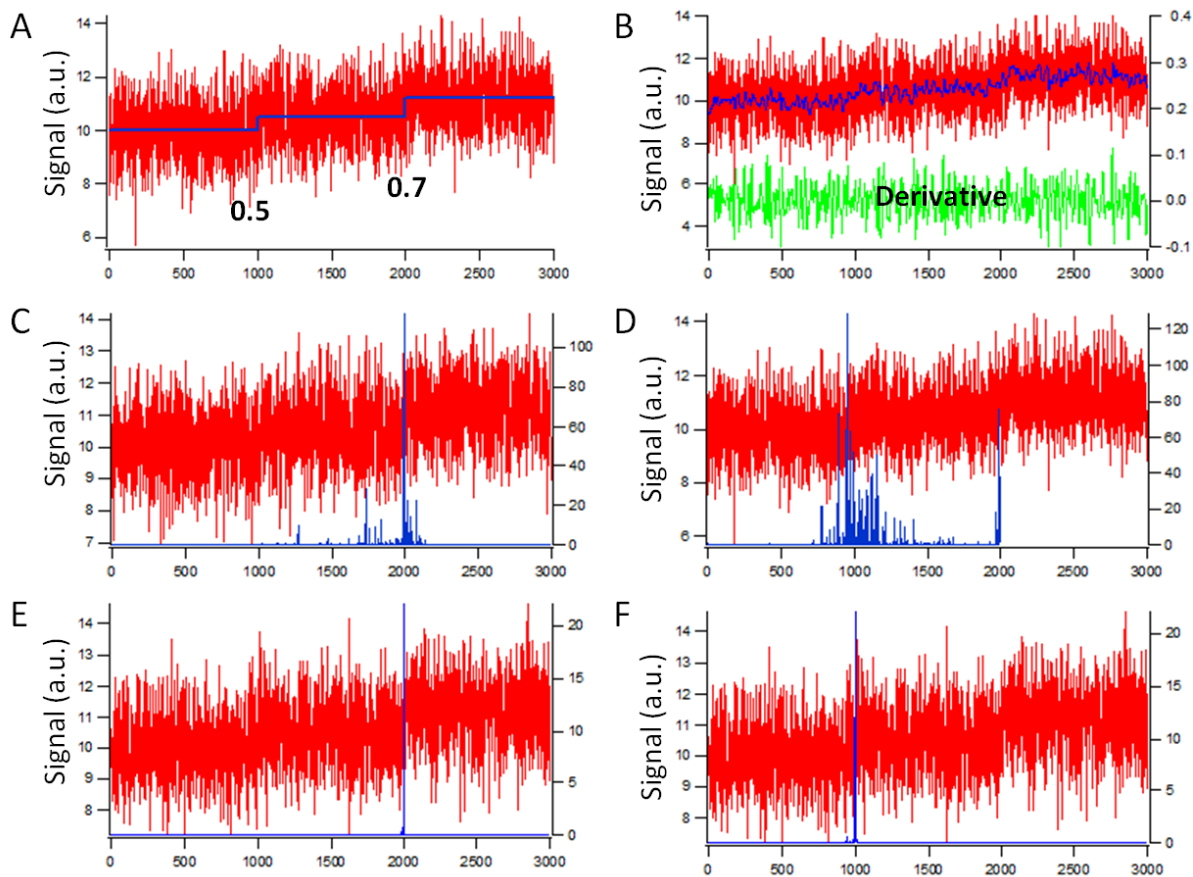


Figure 6.7: A test case comparison for force transition detection. A. The test trajectory (red) is synthesized from the step function (blue). B. Ineffectiveness of the differential method (green) and signal smoothing (blue). C.  $1/\delta$  trajectory (blue) of the entire force curve, indicating the most likely position of the primary force transition. D.  $1/\delta$  trajectory (blue) of the force trajectory to the left of the primary transition point, indicating the most likely position of secondary force transition. E. and F. show the  $\exp(-\delta)$  trajectories (blue), giving better indications of both primary and secondary force transition events.

where  $z$  is the tip-surface distance,  $dz/dt$  is the tip velocity, which may differ from the  $z$ -piezo velocity  $v$  (Figure 6.8A). It is critical to correct for the molecular drag effect to recover the true force curve from the molecular responses, as much information about the molecule rely on accurate fit and statistics of the force curves. Uncorrected force curves will cause systematic errors in parameters such as persistence length, contour length, rupture force and the force loading rate at the rupture.

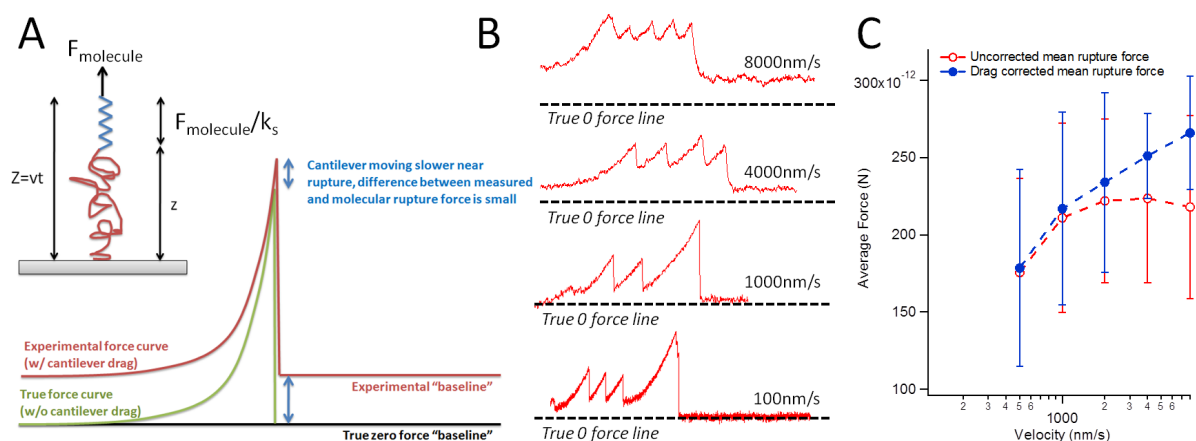


Figure 6.8: Effects of solvent viscous drag on the force curves. A. Schematic showing the experimental force curve (red) is offset from true force curve (green) by a velocity dependent drag. B. Examples of force curves from different pulling velocity. The sample being pulled is the multi-domain GB1 fusion protein. C. the corrected and uncorrected velocity dependent rupture force

The drag is not worrisome for force plateaus, as  $dF_{molecule}/dt = 0$ , leading to the tip velocity equal to the driving velocity  $v$ . Therefore, the experimental baseline can be used as zero-force reference force plateaus. However,  $dF_{molecule}/dt$  is non-zero when the molecule exhibits non-constant force responses such as the entropic elastic response. In this case,  $F_{molecule}$  rises faster towards the rupture point, thereby lowering the true tip velocity at rupture. The apparent rupture force with respect to the experimental baseline would be lower than expected (Figure 6.8B, C).

Two parameters are needed to correct for drift: the tip velocity  $dz/dt$ , and the drag coefficient  $\eta$ . The tip velocity can be determined directly from taking derivative of the tip-surface separation (Figure 6.9B, C). The drag coefficient in a particular solution can be calibrated by moving the tip forward and backward at constant velocities without touching the surface or any molecular attachments. The difference in force between the forward and backward force trajectories is  $2\eta v$ . One also needs to determine the distance dependence of  $\eta$ , as  $\eta$  increases as the tip approaches the surface [92]. Placing these determined factors allows the reconstruction of the entire force curve, giving rise to more

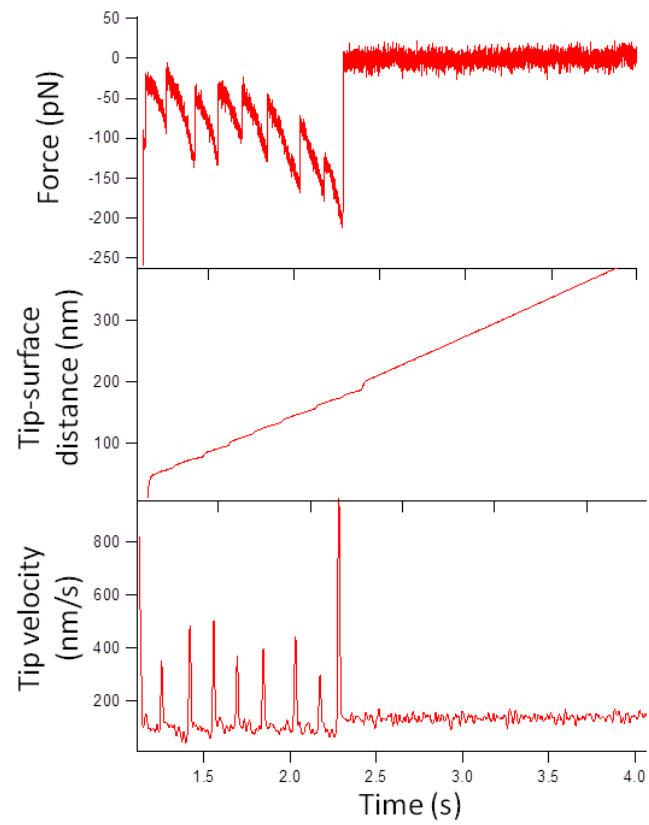


Figure 6.9: Force (top), tip-surface distance (middle), and tip velocity (bottom) trajectories of a multiple-domain GB1 protein unfolding force curve.

accurate rupture force parameters and WLC fitting parameters.

## 6.6 Statistical analysis of force plateaus

Statistical analysis on the mean value of the force plateaus was carried out. Two methods were used that gave agreeing results. The first method is to get statistical information from all data points along the force curves. After data conditioning and filtering, the force trajectory segment containing only the force plateau and the baseline are isolated. Joining up 840 such force trajectories for PVBP end-to-end shows a statistically well-defined plateau (Figure 6.10A, B). Force histograms taking all data points along the joined force trajectory in Figure 6.10A shows two well defined Gaussian distributions, the tall one corresponds to the 0 force baseline (Figure 6.10D); while the smaller one corresponds to the plateau force (Figure 6.10D). The force difference from baseline peak to force plateau peak is  $75.57 \pm 0.02$  pN. The baseline distribution has a width of  $11.87 \pm 0.02$  pN and the width is  $13.42 \pm 0.03$  pN for force plateau. The errors here represent Gaussian fitting error.

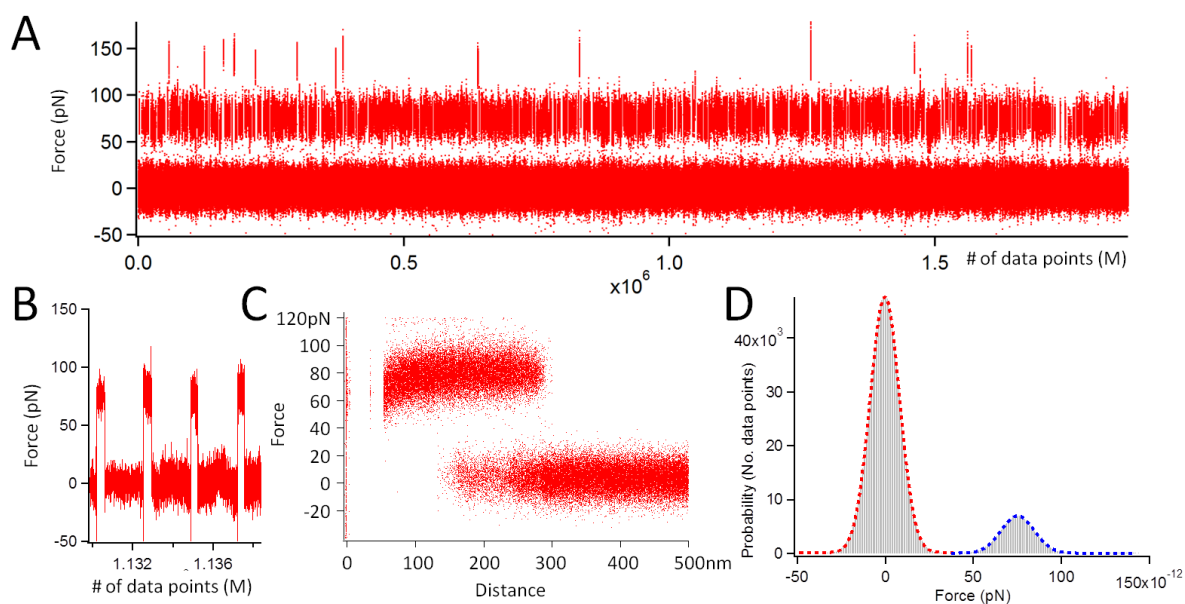


Figure 6.10: Statistics of plateau force by taking all data points into distribution. A. joining 840 force trajectories containing only the plateau and baseline, end to end. The lower baseline (centered around 0 pN) clearly distinguishes from the force plateau (centered around 75 pN). B. zooming into a segment of A. C. overlapping all force-extension curves. D. the force histogram, showing two clear peaks. Both fit to Gaussian distributions. Red Gaussian distribution indicates the baseline, while blue distribution is where the force plateau is.

The distribution of all force curve data points is convolved with the thermal fluctuation of the cantilever. In order to obtain the distribution of the underlying physical process, one must remove the cantilever's thermal fluctuations. To do so, the distribution of the mean value of each force plateau was investigated, which forms a Gaussian centered at  $75.30 \pm 0.07$  pN with a width of  $6.4 \pm 0.1$  pN (Figure 6.11A). The distribution of the mean value and the distribution of all data points peak at the same value, however, the distribution of the mean value is significantly narrower (Figure 6.11B). All results in this thesis are processed by the distribution of the mean plateau force.

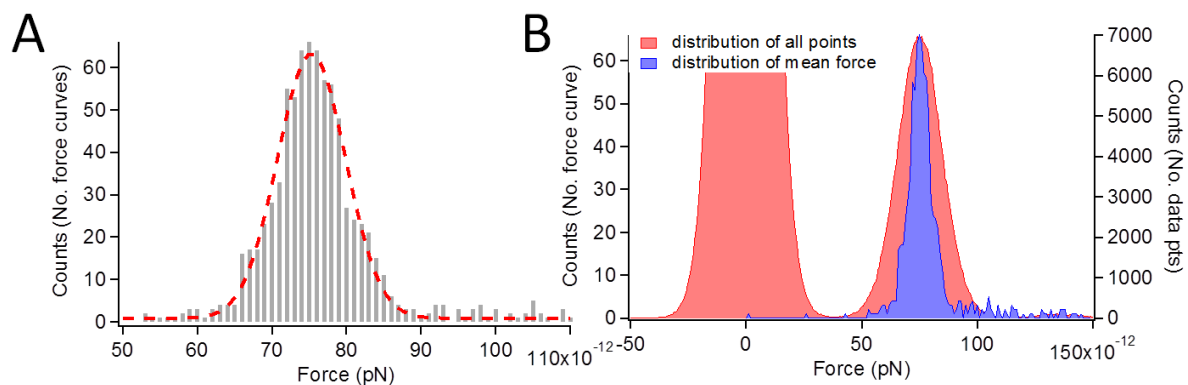


Figure 6.11: Distribution of the mean force. A. Histogram of mean plateau force. B. Comparison of the histogram of mean force (blue) vs. the histogram of all force points from force curves (red).

## 6.7 Graphical User Interface (GUI)

As all experiments step into unknown territory, there are risks to assume the code that works for one case would work for another. In particular, if the force curve shapes differ from one experiment to another. Blindly filtering force curves may result in representative curves being discarded because they do not resemble the filtering criteria. Furthermore, failures to either properly condition the force curves, or to detect rupture events, or to fit the curves will result in systematic biases if these analysis are done blindly. Therefore, it is necessary to monitor both filtering and analyzing stages of automated processing. Graphical User Interfaces (GUIs) were designed to combat this issue. During the loading and filtering of the force curves, a GUI displays the force curve being processed and its score (Figure 6.12). Typically the program can process 400 force curves per minute (depending on the computer speed), which is more than 10 times faster than manual filtering and is slow enough to spot common features in the force curves and whether they are picked up by the program.

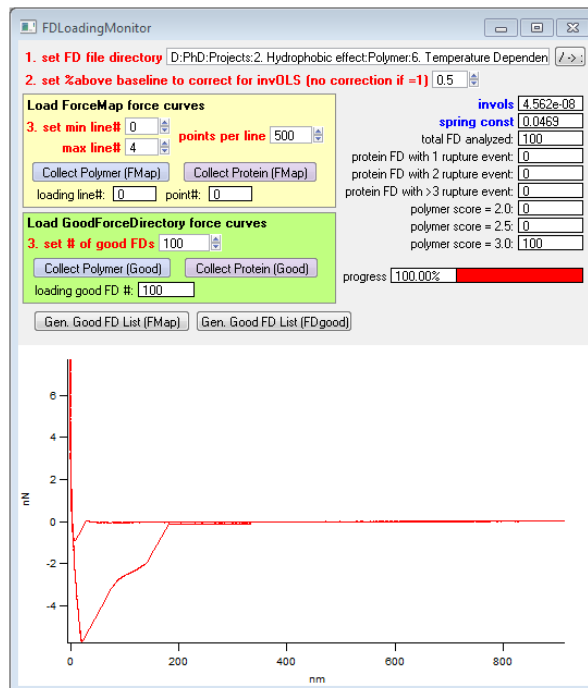


Figure 6.12: Force curve loading GUI, featuring live display of force curves and the filtering results.

The data analysis GUI allows one to either manually analyze individual force curves or automatically analyze all force curves. Different parameters for manual processing must be changed within the code. The analysis results are displayed live on the GUI. The force curve itself is color-coded for different every segment including approach curve, individual pulling events, and retraction baseline (Figure 6.13). The curve fit results are displayed overlapping the force curves, the fit parameters and overall statistics are also graphically displayed. Such a GUI is not only good for analysis, but also good for quickly determine the results right after an experiment to provide guidance for the next experimental condition.

## 6.8 Conclusion

Due to the sheer volume of force curves that needs to be analyzed for single molecule force spectroscopy experiments, automated programs are required to perform unbiased processing. The development of an automated program was described; in particular, the critical steps taken to condition, filter, and analyze force curves. Single molecule force curves directly from experiments may not be in the form for direct analysis due to instrumental drift and noise. Conditioning of these force curves by detecting and

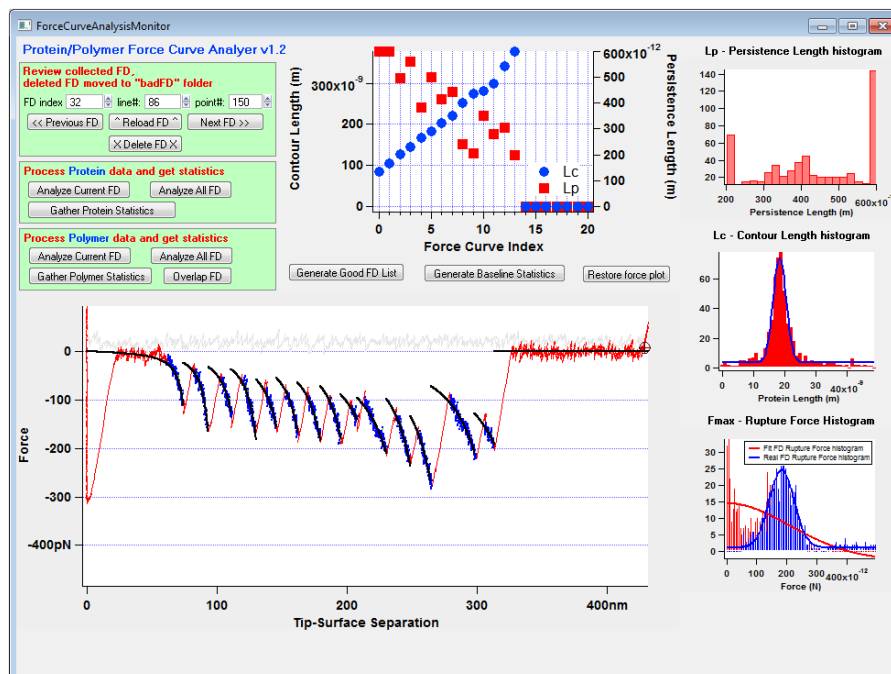


Figure 6.13: Force curve analysis GUI. Force curves can be individually analyzed or batch processed. The fitting parameters such as contour length ( $L_c$ ) and persistence length ( $L_p$ ) of each force curve are displayed for immediate assessments. Accumulated statistical results are displayed on the right.

correcting problems in invOLS, baseline tilt, and viscous drag was undertaken. Once conditioned, the force curves containing single molecule pulling events satisfying a set of criteria are filtered and further statistically analyzed. In addition, GUIs were developed to monitor all these processes to ensure the automated processes do not introduce systematic biases to the results.

## Chapter 7

# Solvent Dependence of Hydrophobic Hydration

In this chapter, the hypothesis that polymer-solvent interfacial tension is adequate to describe the energetics of the collapse of a hydrophobic homopolymer chain at fixed temperature is examined, which serves as a simplified model for studying the hydrophobic collapse of a protein. This implies that changes in polymer-solvent interfacial tension should be directly proportional to the force to extend a collapsed polymer into a bad solvent. To test this hypothesis, single molecule force spectroscopy on a collapsed, single, polystyrene chain in water-ethanol and water-salt mixtures were undertaken where the monomer solvation free energy ( $\Delta G^{solv}$ ) was measured from ensemble average conformations. (In this chapter, the term “solvation free energy” is used rather than “hydration free energy” due to the fact that general solvents are used that are not necessarily aqueous. In the case of aqueous solutions,  $\Delta G^{solv}$  would have the same meaning as  $\Delta G^{hyd}$  used in other parts of the thesis.) Different proportions within the binary mixture were used to create solvents with different interfacial free energies with polystyrene. In these mixed solvents, a linear correlation was observed between the interfacial tension and the force required to extend the chain into solution, which is a direct measure of  $\Delta G^{solv}$  per monomer on a single chain at room temperature. A simple analytical model compares favorably with the experimental results. This knowledge supports a common assumption that explicit water solvent may not be necessary for cases whose primary concerns are hydrophobic interactions and hydrophobic hydration.

## 7.1 Introduction

The hydrophobic interaction is involved in many important chemical and biological processes including receptor-ligand interactions, protein folding and assembly, as well as interactions in lipid membranes. Understanding the mechanism of the hydrophobic effect has become increasingly important to explain fundamental biophysics and biochemistry [156, 54, 72, 88, 32, 111, 85] as well as to engineer new materials [53, 47, 187, 19, 62]. Despite the rich theoretical literature on hydrophobicity, the mechanism of the interaction is still not completely understood due to the relatively small amount of experimental verification. The effects of microscopic bubble bridges [8, 29], water structure [44, 55], dewetting transition surrounding hydrophobes [77, 83, 78] and solvent density fluctuation [167, 121, 177] have been investigated to explain the hydrophobic effect in various systems including particles [77, 177], plates [78, 34], proteins [54, 110, 189, 57, 24, 86, 33] and polymers [55, 167, 121, 7, 82] (see reviews [32, 15, 166, 39, 142, 147, 12]). The role of hydrophobic interaction in polymer and protein system is of special interest due to the fact that the majority of functional biomolecules are polymeric. Because of the complex interactions involved in the hydrophobic collapse of polymers, it is difficult to directly apply the concept of hydrophobic interaction to study these systems of interest. In this study, a simple parameter, namely the interfacial tension between the hydrophobic polymer and solvents (interfacial tension refers to polymer-solvent interfacial tension for the rest of this chapter), was explored to see how it can describe the force that holds a hydrophobic polymer chain (polystyrene) out of solutions - poor solvents for polystyrene. Indeed, theories and simulations studying the hydrophobic effect have used the solvent-vapor surface tension to predict the free energy of the interaction (surface tension refers to the liquid-vapor surface tension for the rest of this article). There is evidence that showed the  $\Delta G^{solv}$  of hydrophobic particles scale with the surface area [4]. However, some theories have predicted that this scaling law holds for large hydrophobic particles but fails for small hydrophobic particles where  $\Delta G^{solv}$  scales with the volume [74, 112, 75, 146]. In particular, it has been argued that the size of biological systems falls in the cross-over region between small and large hydrophobic particles, making hydrophobic interaction's role there even more difficult to predict. It is shown from force-extension curves and solvent dependence data, that the system's  $\Delta G^{solv}$  scales with the length of the extended polymer, and the  $\Delta G^{solv}$  per monomer unit in aqueous solution is proportional to the interfacial tension. At the same time, this does not contradict the size dependence effect predicted for small solutes.

Analytical theories and simulations have shown that a homopolymer in poor solvent

under tension undergoes a phase transition where a single chain is forced to solvate by the external force as it is being pulled out of the collapsed state and into the solvent. When this happens, the collapsed state (beads) coexists with extended state (connecting thread) in a single chain in what is called the “necklace of beads” model where the force-extension profile in this transition region is constant [57, 41, 140, 66, 35, 190, 65]. In these models, the total free energy of the system is related to the solvent–solvent, polymer–solvent and polymer–polymer interactions; these effects are combined to give rise to the constant force profile. In the case of a hydrophobic polymer in aqueous solvents, the dominant driving force for the polymer collapse is the hydrophobic interaction. Therefore, the hydrophobic hydration of a polymer chain in solvent can be directly probed in the force plateau region. This is experimentally challenging as highly hydrophobic polymer does not dissolve in aqueous solvents, making it impossible to study with conventional ensemble measurements. However, it is possible to study such a system at a single molecule level where a single chain is pulled into solution by force spectroscopy using atomic force microscopy (AFM).

Force spectroscopy has become relatively commonplace during the past decade with the advancement of AFM, optical tweezers and other single molecule techniques. It has enabled numerous single molecule mechanical studies on biological molecules such as proteins and DNAs [161, 98, 150, 117]. Much has been learned about the unfolding and refolding pathways of proteins under mechanical forces [117, 118, 16, 131, 125, 102] as well as the binding activities between receptors and ligands [119, 128, 116] for example. Despite the numerous theoretical and simulation efforts, experimental studies focusing directly on hydrophobic collapse of polymers and proteins are still rare [61, 60, 100, 172, 184]. Due to the complex interactions of amino acids in proteins, it is difficult to isolate the role of hydrophobicity for study. Therefore in this work, a simple homopolymer was used whose primary apparent cause of collapse in water is the hydrophobic interaction. This facilitates theoretical modeling efforts and hence enables direct comparison of simulation and experiment. Although the polystyrene chain used in this experiment is a homopolymer and is roughly three times longer than that of a typical globular protein, it serves as a simple model for pulling hydrophobic chain from a single protein globule. The focus of the model here is to look at the effects of solvent conditions and how it affects the hydrophobic collapse from an energetic perspective. Single molecule force spectroscopy allows us to observe the force response of a single molecule under mechanical perturbation.

In this chapter, single molecule pulling experiments on polystyrene in various aqueous solvents was reported. The results show a linear correlation between the force to

extend the hydrophobic polymer and the polymer-solvent interfacial tension obtained from macroscopic measurement. Our analytical model confirms the experimental results by showing similar force-extension profiles and linear dependency of the extension force to the interfacial tension. These results suggest that, fixed at room temperature, the macroscopically measured interfacial tension between polystyrene polymer and aqueous solvent captures most of the essential interactions that are still applicable to microscopic systems down to a single macromolecule.

## 7.2 Methods and materials

### 7.2.1 Sample preparation

Polystyrene with a molecular weight of 130k and a polydispersity of 1.05 was purchased from Polymer Source Inc. (P5157-S). The polymer was dissolved in distilled tetrahydrofuran (Sigma Aldrich) or toluene (Sigma Aldrich) at 1 mg/mL concentration for 6 hours and subsequently diluted to 1  $\mu\text{g}/\text{mL}$  and left to further dissolve for 24 hours. The diluted solution was then spin-coated on piranha-cleaned silicon wafer or flame-annealed gold at 2000 rpm for 1 minute. The sample was then thoroughly dried in vacuum chamber before use. Ethanol and deionized water were passed through 0.2  $\mu\text{m}$  PTFE and cellulose filters respectively.

### 7.2.2 Single molecule force spectroscopy

Gold-coated biolevers from Olympus (BL-RC150VB-C1) and silicon nitride cantilevers from Veeco (MLCT-AUNM) were used in the single molecule pulling experiments. The cantilever spring constants were calibrated by thermal method, and are 5 pN/nm and  $\sim 15$  pN/nm respectively. All experiments were performed using the MFP-3D AFM from Asylum Research. For all experiments, the system temperature was kept constant at 300 K using the thermal controller from Asylum Research. The data acquisition rate was 5 kHz and various pulling velocities between 500 nm/s and 3000 nm/s were used. Data analysis was performed according to Chapter 6.

## 7.3 Determination of macroscopic interfacial tension

The hypothesis is that the force plateau is due to hydrophobic hydration and the magnitude of the plateau force is therefore proportional to the interfacial tension between the

aqueous solvent and the polymer. To test this hypothesis, pulling experiments on single polystyrene molecules adsorbed on silicon surface in different aqueous solvents were performed. Different polymer-solvent interfacial tension  $\gamma_{ps}$  can be achieved by changing solvent surface tension and can be calculated according to the extended Fowkes equation [48, 56, 139, 49, 50]:

$$\gamma_{ps} = \gamma_p + \gamma_s - 2\sqrt{\gamma_p^d \gamma_s^d} - 2\sqrt{\gamma_p^p \gamma_s^p} \quad (7.1)$$

or Wu's equation [179, 180]:

$$\gamma_{ps} = \gamma_p + \gamma_s - \left( \frac{4\gamma_p^d \gamma_s^d}{\gamma_p^d + \gamma_s^d} \right) - \left( \frac{4\gamma_p^p \gamma_s^p}{\gamma_p^p + \gamma_s^p} \right) \quad (7.2)$$

with:

$$\gamma_p = \gamma_p^d + \gamma_p^p \quad (7.3)$$

$$\gamma_s = \gamma_s^d + \gamma_s^p \quad (7.4)$$

where  $\gamma_p$  and  $\gamma_s$  are the surface tensions of polystyrene and the solvent,  $\gamma_p^d$  and  $\gamma_s^d$  are the dispersive contributions to the surface tensions,  $\gamma_p^p$  and  $\gamma_s^p$  are the polar contributions to the surface tensions of the polymer and the solvent.

The dispersion and polar components of polystyrene have been reported with great variations, which is also the case for many other polymers [154, 17]. The discrepancy in the reported dispersion and polar component values can be a result of the model or equation used to produce them. For instance, in the study by Saito [154], the polar component of polystyrene of 0.9 mJ/m<sup>2</sup> was generated using the extended Fowkes equation whereas the polar component is 4.8 mJ/m<sup>2</sup>, over 5 times greater when generated using Wu's equation (see Table 7.1 and Table 7.2) [154]. Since both values are calculated from the same experimental contact angle measurements, they should reproduce the same work of adhesion with the corresponding equations. The discrepancies in polar and dispersive contributions from the two equations are entirely due to their different definitions in the work of adhesion calculation. Hence, as long as the equation used to calculate the interfacial tension matches the one used to obtain the polar and dispersive contributions, these discrepancies will not affect the interfacial tension. In this study, the solvent polar and dispersive components from literature [154, 37] are calculated using the extended Fowkes equation; to match it, the polar and dispersive components of polystyrene was used, calculated also by the extended Fowkes equation (see Table 7.1).

Decreasing the surface tension of the aqueous solution most effectively reduces the interfacial tension with the polymer. To reduce the surface tension of the aqueous solution in the experiment, ethanol was added to deionized water at different molar ratios (see Table 7.2). The addition of ethanol to water strongly influences the surface tension of water, giving surface tensions that range from 72.6 to 21.9 mJ/m<sup>2</sup>. It has been reported that ethanol reduces the surface tension of water by changes in hydrophobic hydration [133]. The dispersive and polar contributions to the surface tension of ethanol-water mixture were taken from earlier contact angle experiments [37]. It has been shown that addition of salt increases the surface tension of the water by a combination of factors including the electrostatic image force, ion hydration and others as described by Weissenborn [79, 176]. For NaCl in water, the surface tension increases by 2.08 mJ/m<sup>2</sup> for every additional molar increase in the concentration of NaCl [79, 176]. Higher surface tension does not necessarily result in higher interfacial tension; Table 7.2 shows that iodomethane has a large surface tension but a low interfacial tension. Apparently the boundary between good and bad solvent for polystyrene occurs at an interfacial tension of  $\sim 5$  mJ/m<sup>2</sup>.

The addition of ethanol or salt affects mainly the polar component of solution surface tension while the dispersion component does not change much. At the same time, the polar component of the surface energy of polystyrene according to the extended Fowkes equation contributes only 2.2% of the total adhesive interaction energy between polystyrene and the various solvents, while the rest comes from dispersive interactions (Table 7.1 and Table 7.2). This indicates that the change in interfacial tension contributed by dispersive interaction is relatively constant for our aqueous solutions while the greatest contribution comes from the changes in the polar component of the solvent. Since the polar interaction and hydrogen bonding in aqueous solution is the putative cause of hydrophobic effect, this result suggests that by adding ethanol and salt, one is directly modifying the strength of hydrophobic hydration and hydrophobic interaction.

Polymer	$\gamma_s$ (mJ/m <sup>2</sup> )	$\gamma_s^d$ (mJ/m <sup>2</sup> )	$\gamma_s^p$ (mJ/m <sup>2</sup> )	
Polystyrene [154]	40.7	35.9	4.8	Derived from Wu's eq
Polystyrene [154]	40.6	39.7	0.9	Derived from ext. Fowkes eq

Table 7.1: Dispersive and polar contributions to surface tensions of polystyrene used in this study by Wu's equation and extended Fowkes equation

Solvent	$\gamma_s$ (mJ/m <sup>2</sup> )	$\gamma_s^d$ (mJ/m <sup>2</sup> )	$\gamma_s^p$ (mJ/m <sup>2</sup> )	$\gamma_{ps}$ (mJ/m <sup>2</sup> )
<b>Poor solvents</b>				
2M NaCl in water [79, 176]	76.8	22.1	54.7	43.6
Water [37]	72.6	22.1	50.6	40.0
2.5 mol% EtOH[37]	57.6	20.6	37.0	29.0
5.0 mol% EtOH[37]	47.7	19.6	28.1	22.1
10 mol% EtOH[37]	36.8	18.5	18.3	14.7
20 mol% EtOH[37]	29.5	17.8	11.8	10.2
30 mol% EtOH[37]	27.6	17.6	10.0	9.1
40 mol% EtOH[37]	26.6	17.5	9.1	8.5
EtOH[37]	21.9	17.0	4.9	6.2
<b>Good solvents</b>				
Iodomethane [157]	45.0	42.1	2.9	0.5
Hexadecane [96]	27.6	27.6	0.0	2.0
Benzene	28.9	28.9	0.0	1.8

Table 7.2: Dispersive and polar contributions to surface tensions of the solvent used in this study as well as the interfacial tension between the solvent and polystyrene

## 7.4 Unfolding polystyrene in aqueous solutions

Varying the concentration of ethanol in water changes the surface tension of the solution and consequently changes the interfacial tension between the polymer and the solvent. All experiments were done in a closed fluid cell, to minimize solvent evaporation that would lead to changes in concentration of ethanol and NaCl. Force plateaus were seen in pulling experiments in all water-ethanol mixtures and pure ethanol (Figure 7.1). With increasing ethanol content, the plateau force decreases (Figure 7.1), while NaCl salt solution elevates the plateau force (Table 7.3). To find the magnitude of the plateau forces more accurately, the force curves from each solvent experiment are overlapped by their retraction baseline (Figure 7.2a) and created a histogram of forces from regions of the force-extension curve that contains only the force plateaus (i.e., no indentation) and the retraction baseline (Figure 7.2b). The retraction baseline is used because the cantilever is moving at the same velocity at the force plateau region as in the retraction baseline. As will be described later in the article, the force plateau is also velocity independent over the range studied. Hence, there is no need to correct for any effects due to pulling velocity. The histogram containing only the plateau and baseline is then fitted to Gaussian curves to assess the mean and standard deviations of the plateau force (Figure 7.2b).

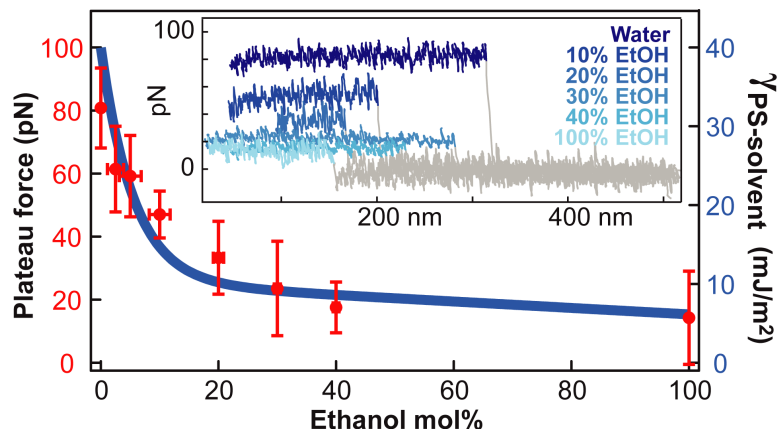


Figure 7.1: Plateau force magnitude and interfacial tension as a function of the mol% ethanol in water. The closed circles with error bars are calculated from the experimental force plateau data. The vertical errors are due to the cantilever thermal noise and standard deviation in the results for multiple samples, the horizontal error bars comes from the precision of preparing and maintaining the correct ethanol concentrations (as a result, zero error bars for pure water and pure ethanol). The thick gray line is the calculated polymer-solvent interfacial tension at various ethanol concentrations. The inset shows force curves corresponding to a range of ethanol concentration. The height of the force curve decreases as the concentration of ethanol increases.

	Pure water	2M NaCl solution
Interfacial tension ( $\text{mJ}/\text{m}^2$ )	40.0	43.6
Plateau force (pN)	$80 \pm 13$	$97 \pm 15$

Table 7.3: Plateau force magnitude and interfacial tension in pure water and 2M NaCl solution.

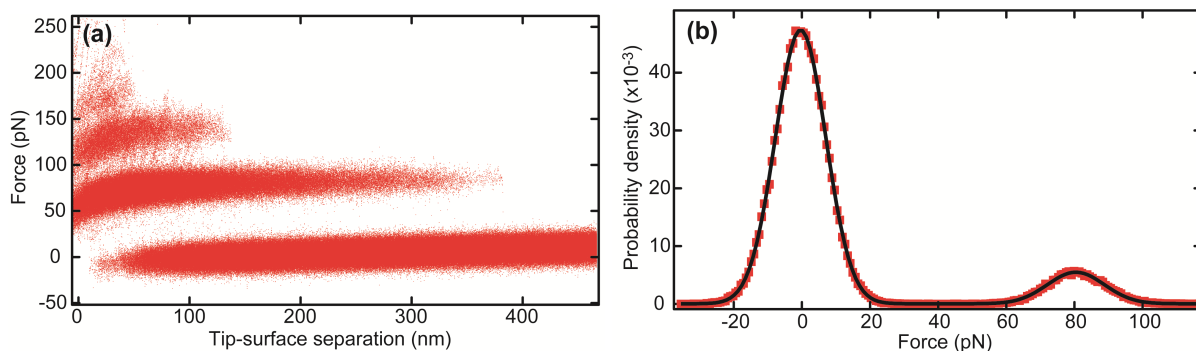


Figure 7.2: (a) Superposition of  $\sim 300$  force-extension curves shows discrete steps, which indicates the pulling of single chain from the surface. (b) Histograms (gray open squares) showing the baseline and the first step from the figure above. Gaussian distribution (solid black) fits well over the histogram. The taller peak on the left corresponds to the baseline, whereas the one on the right is the distribution of the first plateau forces.

The transition from plateau to entropic elastic behavior in the high surface tension aqueous solvents such as pure water and NaCl solution is more distinct than for those in higher concentrations of ethanol. This suggests that the collapsed and extended structures are more distinct in higher surface tension aqueous solutions (e.g., pure water and salt solutions) than in low surface tension solutions (e.g., high ethanol concentration). It has been shown that polystyrene swells slightly 81 in ethanol while remaining in the collapsed state. Since the driving force for polystyrene to collapse in water is much greater than in ethanol solutions due to higher interfacial tension, the collapsed structure should be more tightly condensed. Compared with well collapsed polystyrene in water, the swelling in ethanol gives polystyrene chain a conformation closer to that of an extended structure because more chains are solvent exposed in the swelled state. This could contribute to the observed, more gradual transition from force plateau to entropic elasticity in ethanol.

## 7.5 Unfolding polystyrene in good solvents

Due to the incompatibility between the material of our microscope and good solvents for polystyrene such as tetrahydrofuran and toluene, previous results for polystyrene pulling in toluene was used [60]. It has been shown that polystyrene force-extension profile agrees well with models describing entropic elasticity such as the freely joined chain model (Figure 7.3). This is not surprising, as one would expect this type of behavior for a homopolymer in good solvent. Because benzene, toluene, hexadecane and iodomethane are all good solvents for polystyrene, it is reasonable to assume that the force-extension profile in all four solvents exhibit similar entropic elastic response. Therefore, we assigned a magnitude of zero to the hypothetical force plateau in these solvents.

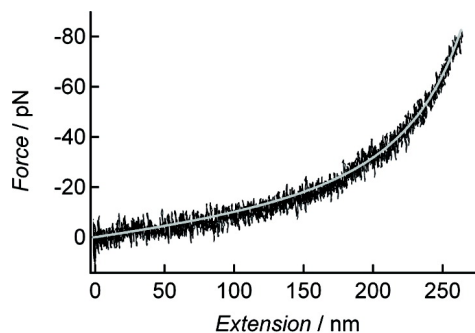


Figure 7.3: Pulling PS in toluene, a good solvent, shows a purely entropic elastic response. (Figure adapted from Gunari and Walker [60].)

## 7.6 Correlation between extension force and interfacial tension

Figure 7.4a plots the plateau force against the interfacial tension in different solvents. While benzene, hexadecane and iodomethane (on the very low end of interfacial tension) are good solvents for polystyrene, the rest of the solvents used in this study, which includes ethanol, ethanol water mixture, water and salt solutions, are bad solvents. The general trend is the worse the solvent, the higher the plateau force. The data are well fitted by a line that passes through the origin, within the margin of error:

$$F_{\text{plateau}} = (2.2 \pm 0.3)\gamma_{ps} + (2 \pm 7) \quad (7.5)$$

where  $F_{\text{plateau}}$  is in the unit of pN,  $\gamma_{ps}$  is in unit of mJ/m<sup>2</sup>, and the errors correspond to 95% confidence interval. This result strongly indicates the dependence of the magnitude of force plateau on the polymer-solvent interfacial tension. The values are comparable to results from the analytical model introduced in Section 4.2.1, which assumed a flexible cylindrical hydrophobic polymer with dimensions estimated from the size of a styrene molecule. Of course, the assumption of the cylindrical polymer shape gives only a crude approximation of the solvent exposure area per polymer unit. However, the linear dependency and the similar values between experiment and theory show that the basic physics behind the force plateau is captured by the model.

As mentioned above, in the water-ethanol and water-salt systems, the change in interfacial energy is mainly due to the polar and hydrogen bonding interactions of the solvent alone, while the solvent-polymer and polymer-polymer interaction energies remain relatively constant. The dependence of the plateau force on the interfacial energy then suggests that the plateau forces are direct results of hydrophobic interaction at fixed room temperature. This also suggests that the net effect of water structure at the microscopic interface with the hydrophobic polystyrene is already incorporated in the macroscopically measured interfacial tension parameter. This knowledge could help reduce the complexity of simulations by showing that explicit water solvent may not be necessary for cases whose only concerns are hydrophobic hydration and hydrophobic interaction at fixed temperature.

A similar solvent dependent study reported a linear dependence of the unbinding force between hydrophobic small molecules –  $\beta$ -cyclodextrin and adamantane on the surface tension of the solvent instead of the interfacial tension [184]. For highly hydrophobic solute in alcohol-water mixtures, the interfacial tension scales relatively linearly with

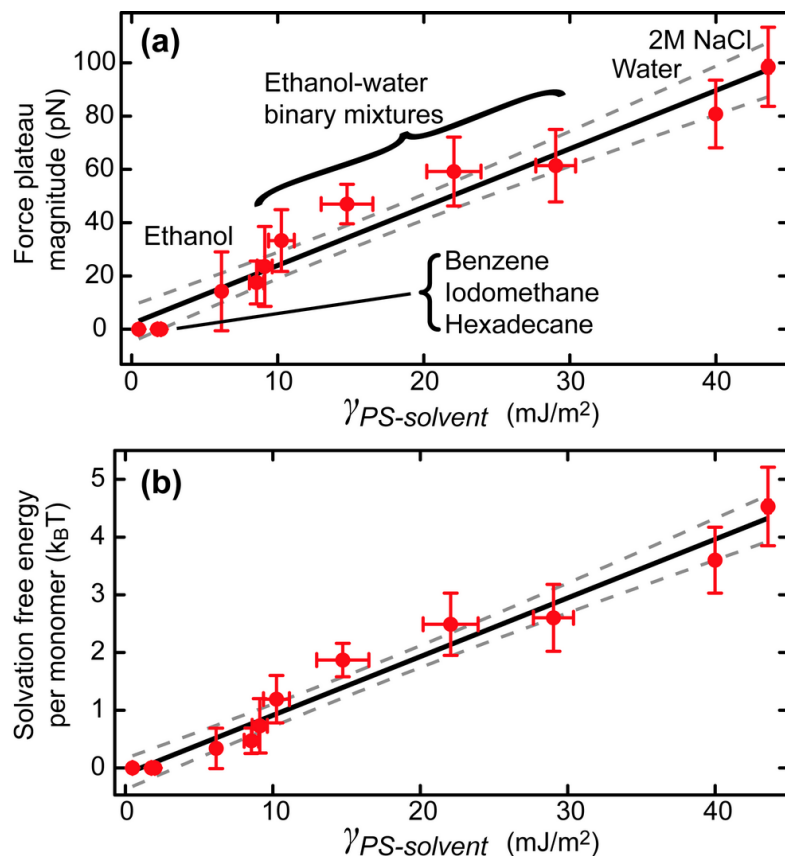


Figure 7.4: Correlation between plateau force and  $\gamma_{ps}$ . (a) The force plateau magnitude plotted against the interfacial energy between the solvent and polystyrene for various solvents. (b)  $\Delta G^{solv}$  per monomer calculated from force plateau corrected for chain entropic elasticity. The linear fit and the 95% confidence interval of the fit are shown as solid and dashed lines. The vertical errors are due to the cantilever thermal noise and standard deviation in the results for multiple samples, the horizontal error bars comes from the precision of preparing and maintaining the correct ethanol concentrations (as a result, zero error bars for pure water and pure ethanol).

the surface tension of the solvent due to linear scaling of the dispersive contribution of the solvent and the lack of polar contribution of the solutes. Hence, a linear correlation between force and interfacial tension would also result in linear correlation between force and surface tension. However, the interfacial tension is a more fundamentally significant parameter because it incorporates not only solvent-solvent interaction (surface tension), but also solvent-solute and solute-solute interactions. This is evident from the zero  $y$ -intercept of force-interfacial tension plot and non-zero  $y$ -intercept [184] when graphing force against solvent surface tension. Therefore, it is more meaningful to use the interfacial tension to explain hydrophobic and the more general solvophobic interaction. Furthermore, interfacial tension is a more general description of the interaction between polymer and solvent and therefore can also be extended to explain polymers in good solvents. For example, iodomethane is a good solvent for polystyrene with interfacial tension value of  $0.5 \text{ mJ/m}^2$ , but has a high surface tension value of  $45 \text{ mJ/m}^2$ . This places the force vs. interfacial tension data point of iodomethane on the line extrapolated from Figure 7.4a and b, but the iodomethane data point of force vs. surface tension would not lie on any line that extrapolates force against surface tension.

## 7.7 Interfacial tension provides solvent condition on microscopic scale

The results presented here tested how the hydrophobic interaction strength in a polymer depends on the solvent condition. Ethanol was used to decrease the strength of hydrophobic interaction, while NaCl salt was used to increase it. Ethanol effectively decreases the surface tension of water (Figure 7.1) by disrupting water-water hydrogen bonds and adsorbing at interfaces [20], thereby weakening the hydrophobic interaction. Indeed, SMFS on PS in aqueous ethanolic solutions revealed plateau forces whose magnitude decreased with increasing ethanol fraction (Figure 7.1). Ethanol is a poor solvent for PS, and a low plateau force in pure ethanol was observed (Figure 7.1 inset). The magnitude of the decreasing plateau force can be correlated to the interfacial tension at bulk PS-water interface (Figure 7.4). This linear correlation was observed for other solvents too. Pulling experiments in good solvents for PS such as toluene and benzene generated force curves that exhibit purely entropic elastic response indicating that PS was initially not in a collapsed state; hence, the energy associated with the unfolding is zero. Furthermore, NaCl solutions increased the magnitude of the plateau in the same way it increases the surface tension of water and thereby strengthens the hydrophobic

interaction. Therefore, the macroscopically measured interfacial tension describes the strength of hydrophobic interaction well even on the microscopic level. Another single molecule experiment drew a similar conclusion, that the unbinding force between hydrophobic small molecules ( $\beta$ -cyclodextrin and adamantine) linearly depends on the surface tension of the water-ethanol mixture [184].

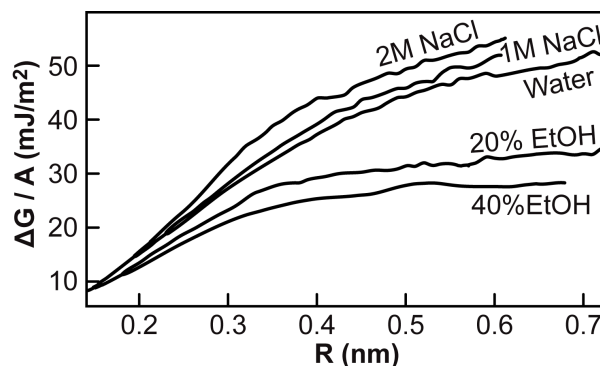


Figure 7.5: The effects of salt and ethanol on the size dependence of the hydration  $\Delta G$  per unit area. (Graph adapted from Rajamani et al.42)

One might ask whether the proportionality with macroscopic interfacial tension contradicts our finding that the hydration of hydrophobic polymers is dominated by the microscopic scale. Theoretical studies of solvent additives indicate that ethanol decreases, while NaCl increases, the hydration  $\Delta G$  on both small and large length scales (Figure 7.5)42. Therefore, it is expected that even though the hydration  $\Delta G$  to unfold a hydrophobic polymer is on the microscopic scale, the strength of the hydrophobic interaction scales with the macroscopic counter-part, the interfacial tension. Therefore, the correlation between microscopic hydration and macroscopic interfacial tension can be expected (Figure 7.6).

## 7.8 Conclusion

In this paper, the force-extension behavior of a hydrophobic polymer in aqueous solutions by single molecule force spectroscopy was examined in detail. The force-extension curves from all aqueous solutions show a constant force plateau region as predicted by theoretical model based on the established idea that collapsed and extended components coexist on a hydrophobic polymer under tension. The dependency of the extension force on the solvent condition was examined using ethanol-water and salt-water solutions that shows a linear dependence of the extension force to the interfacial tension between the polymer and the solvent. The changes in the macroscopic interfacial tension values are mainly

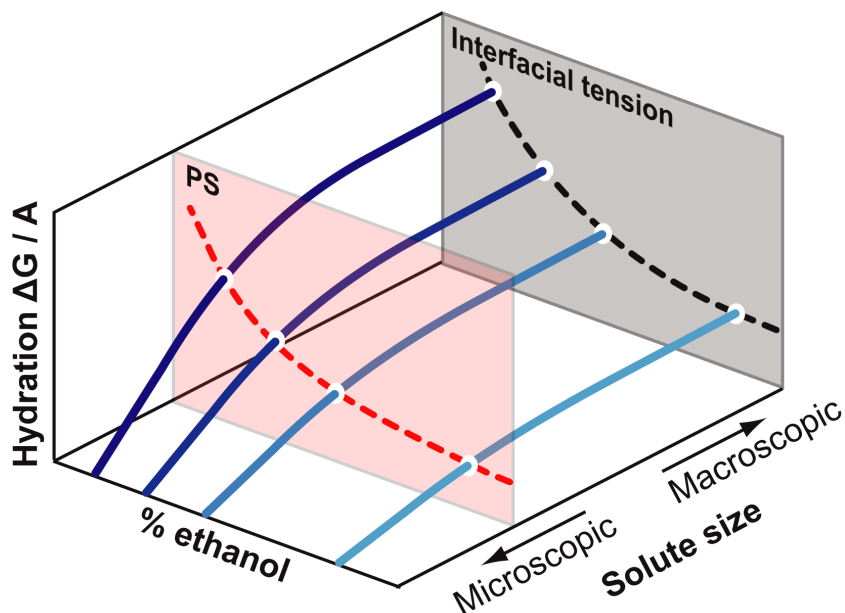


Figure 7.6: Ethanol alters the hydration  $\Delta G/A$  on the microscopic and macroscopic scales similarly. This gives rise to similar solvent-dependent profiles between the microscopic polymer  $\Delta G^{solv}$  and the macroscopic interfacial tension.

due to changes in polar and hydrogen bonding interactions of the solvent. The linear transition of the polymer extension force in pure water to that of pure ethanol indicates that the hydration of hydrophobic polymer in pure water transitions smoothly to the more general solvophobic effect. This may suggest that hydrophobic effect is essentially solvophobic effect with water as the main solvent. The linear fit intersects the origin of the plot corresponding to the zero-interfacial energy and zero  $\Delta G^{solv}$ , where purely entropic elasticity response for the polymer in good solvent is expected. The correlation between the microscopic  $\Delta G^{solv}$  per monomer unit and the macroscopic interfacial tension implies that the macroscopically measured interfacial tension has a corresponding counterpart on the microscopic level. This suggests that the interfacial tension alone is enough to describe the behavior of polystyrene in various solvents at fixed temperature. Finally, the force-extension profile was found to be independent of pulling velocity, which confirms that the plateau force observed is due to hydrophobic hydration and not polymer plasticity or polymer-solvent friction.

# Chapter 8

## Temperature and Size Dependence of Hydrophobic Hydration

A signature of hydrophobicity is its temperature dependence. This chapter reports the first experimental evaluation of the temperature and size dependence of hydration free energy ( $\Delta G^{hyd}$ ) in a single hydrophobic polymer, which tests key assumptions in models of hydrophobic interactions in protein folding. Herein,  $\Delta G^{hyd}$  required to extend three hydrophobic polymers with differently sized aromatic side-chains was directly measured by single molecule force spectroscopy. The results are three-fold. First,  $\Delta G^{hyd}$  per monomer is found to be strongly dependent on temperature and does not follow interfacial thermodynamics. Second, the temperature-dependence profiles are distinct among the three hydrophobic polymers as a result of a hydrophobic size effect at the sub-nanometer scale. Third,  $\Delta G^{hyd}$  of a monomer on a macromolecule is different from a free monomer; corrections for the reduced  $\Delta G^{hyd}$  due to hydrophobic interaction from neighboring units are required.

### 8.1 Introduction

Hydrophobic hydration involves the minimization of the free energies of water molecules near non-polar surfaces. Hydrophobic hydration of macromolecules is central to understanding protein folding [24, 189, 10, 52, 33, 32] and advancing materials science and biotechnologies [40, 132, 31]. A detailed methodology has been developed to study hydrophobic hydration by the mechanical unfolding of a collapsed single hydrophobic polymer [105]. Typically,  $\Delta G^{hyd}$  is assumed to scale with the solvent accessible surface area (SASA) of molecules according to macroscopic interfacial thermodynamics, which is supported by the linear correlation between the SASA and the free energy to transfer hydro-

carbons from a hydrophobic solvent (such as hexadecane) to water [1]. Despite a strong correlation, the experimentally measured small hydrocarbon  $\Delta G^{hyd}$  is smaller than that predicted by the calculated SASA [165], showing the breakdown of macroscopic interfacial thermodynamics at the microscopic scale and suggesting that the origin of the correlation goes beyond SASA. In addition, the temperature dependence of  $\Delta G^{hyd}$  (the signature of hydrophobic hydration) varies according to the size of the solute; this cannot be explained simply by the macroscopic interfacial tension. In an earlier attempt to address these issues, Tolman [169] developed a thermodynamic treatment that lowers the surface tension of water at the solute-water interface by taking into account the cavity curvature. Later developments included temperature dependence of the Tolman length using simulations to address the temperature dependence of  $\Delta G^{hyd}$  [5, 3]. However, it was argued that the correction to the effective surface tension to maintain the correlation between  $\Delta G^{hyd}$  and SASA at small length scales lacked a clear physical meaning [59]. Instead of depending on a scaling relation with SASA, theories and simulations were developed predicting that  $\Delta G^{hyd}$  has nontrivial size dependence: below approximately 1 nm radius,  $\Delta G^{hyd}$  of a spherical solute scales roughly with the solute volume; whereas above this value,  $\Delta G^{hyd}$  scales with SASA and asymptotically approaches the behavior described by macroscopic interfacial thermodynamics [32, 143, 87, 84, 83, 162, 112, 74, 76, 146, 159, 7, 75]. These treatments correctly predict the trend for the temperature dependence of  $\Delta G^{hyd}$  for small molecules.

Theoretical studies of hydrophobic hydration relied on experimental measurements of small molecule solubilities in water and their transfer free energies from organic solvents to water. It is usually assumed that these small molecule  $\Delta G^{hyd}$  can be directly applied to hydrophobic side chains in polymers and proteins. However, this assumption has not been experimentally tested due to the lack of a suitable experimental model system and the difficulty of studying hydrophobic macromolecules insoluble in water. Hydrophobic homopolymers provide simple models of the hydrophobic hydration and collapse of proteins and other linear biological molecules (Figure 1.1). Preceding hydrophobic collapse, an initially extended hydrophobic polymer in water undergoes entropic coiling that reduces the tension along the chain to a point where the coil-globule transition can occur. The onset of this transition depends on the overall hydrophobicity of the polymer such that the transition begins at higher tension and radius of gyration for a hydrophobic homopolymer than for a mixed hydrophobic/hydrophilic polymer such as a protein (Figure 1.1). Similar to a protein, a hydrophobic homopolymer collapses in an aqueous environment into a compact globule that is largely disordered. This captures the essential physics governing the hydrophobic hydration of a protein and is illustrated

in Figure 1.1. Ensemble studies of hydrophobic polymers are not viable due to their insolubility in water and limited experimental access to different conformational states (e.g., extended and collapsed). However, by way of single molecule force spectroscopy using Atomic Force Microscopy (AFM), the conformation of a single hydrophobic polymer can be changed from collapsed globule to extended coil (Figure 5.1) and  $\Delta G^{hyd}$  in this process can be estimated (Figure 5.3). A previous study provides a detailed description of the control experiments undertaken here for the mechanical unfolding of a collapsed single hydrophobic polymer in aqueous solvents [105]. This report presents the effect of temperature on hydrophobic hydration of several polymers and how the size of side chains affects their temperature dependence. The result shows that a phenomenological model using SASA and macroscopic interfacial thermodynamics cannot account for the observed temperature dependence of macromolecular hydrophobic hydration. The observed temperature dependence shows the turnover behavior typically seen in the hydration of small hydrophobic molecules. Moreover, individual monomers along the chain cannot simply be viewed as independent units threaded together, and analysis of the magnitude of  $\Delta G^{hyd}$  shows that there are significant hydrophobic interactions between adjacent units that make the energetic cost to hydrate the chain much smaller than the sum of energies of individual monomers. Therefore, it suggests that free monomer  $\Delta G^{hyd}$  cannot be directly applied to calculate  $\Delta G^{hyd}$  of a hydrophobic macromolecule.

## 8.2 Methods and materials

### 8.2.1 Choosing polymers

In order to study the behavior due to the side chains only, we choose polymers with the same backbone but different side chains. Another criterion for choosing the polymer is that the side-chain must be non-polar. This limits the side-chain selection to alkanes and aromatic groups. However, we found that the interaction between the AFM tip and polyethylene and polypropylene are too weak to be picked up by the AFM tip via physisorption. Therefore, we choose polystyrene based polymers for our studies. Due to the availability of polymers, the following three polymers were chosen: polystyrene (PS), poly-4-tert-butylstyrene (PtBS), and poly-vinyl-biphenyl (PVBP) (Figure 8.1).

### 8.2.2 Polymer sample preparation

The preparation and surface deposition of PS, PtBS and PVBP polymers were performed according to the previously described procedure. 10 PS and PtBS are purchased

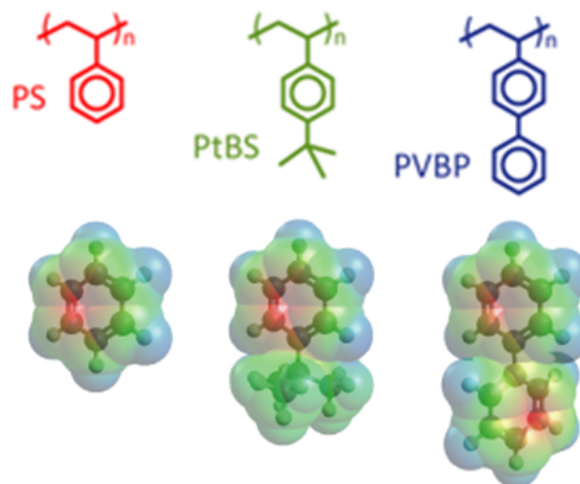


Figure 8.1: Three hydrophobic polymers used in this study, PS, PtBS, and PVBP, share the same backbone but differ in the non-polar side chains. The van der Waals surface of the side chain is illustrated below each polymer.

from Polymer Source Inc (P5157-S and P8213-4tBuS); PVBP was purchased from Sigma Aldrich (CAS No. 25232-08-0, 182540-1G). Details of the polymer preparation can be found in Section 5.3.2.

### 8.2.3 Single molecule force spectroscopy

All single molecule experiments in this study employed the Asylum Research MFP-3D AFM. The use of stiffer 60 pN/nm  $\text{Si}_3\text{N}_4$  AFM tips from Veeco (MLCT-AUNM) minimized the intrinsic cantilever bending due to different experiment temperatures, a problem that makes softer cantilevers employed in the previous work [105] unusable. The spring constants of the cantilevers do not change significantly ( $< 1\%$ ) from  $30^\circ\text{C}$  to  $80^\circ\text{C}$ , as verified by the thermal noise method. The following methods were employed to minimize measurement errors: first, one AFM cantilever was used for every set of temperature dependent experiments ( $30^\circ\text{C}$  to  $80^\circ\text{C}$ ), which eliminated the cantilever calibration error ( $\sim 5\text{--}10\%$ ) within each set of temperature dependent experiment. The final force value at each temperature is obtained from averaging 5–8 sets of independent experiments. Second, it was verified that the measured force was unaffected by any slow-drifting parameters, such as changes in laser intensity or formation of air bubbles on the AFM cantilever. This was achieved using different temperature sequences (Figure 8.2) to ensure that there was no correlation between temperature and time. In order to avoid finite size effect of the collapsed state, single chains were pulled from a layer of polymer aggregate such that the change of surface area of the collapsed state can be approximated

to zero. Roughly 150000 force curves were collected per polymer sample per experiment to ensure sufficient statistics of the results. Approximately 75% of the force curves did not exhibit chain pulling events, roughly 15% percent exhibited rugged profiles characteristic of complex adhesion rupture processes and were discarded. The remaining  $\sim 10\%$  of the force curves were selected for further analysis. For each of the selected force-extension curves, the last force plateau corresponding to single chain hydration was identified and a force histogram containing the last force plateau and the baseline was collected and fitted to two Gaussian functions. The peak to peak distance between the two Gaussians gave the plateau force magnitude of each force curve.

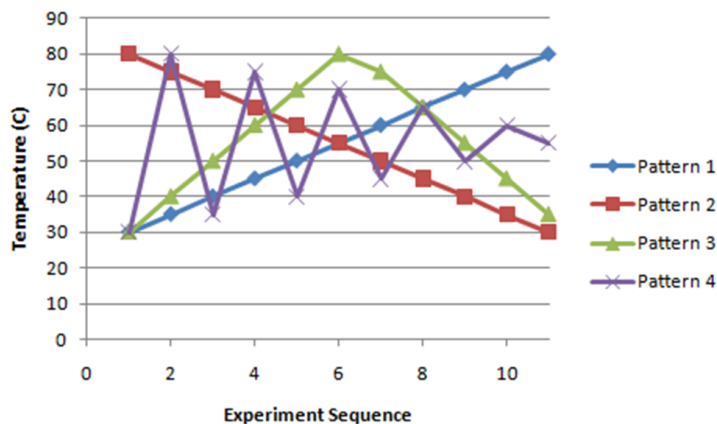


Figure 8.2: Different temperature sequences used in the experiment ensures no systematic errors from slow varying parameters affect the subtle temperature dependencies.

The experimentally accessible temperature range is  $25^{\circ}\text{C}$  to  $80^{\circ}\text{C}$ . Due to the lack of cooling options such as a Peltier device or coolant circulation, the lower temperature limit is the room temperature at  $22^{\circ}\text{C}$ . However, due to heat conduction from the electronics in the AFM head, the equilibrium temperature of the fluid is roughly  $25^{\circ}\text{C}$ . As we have discussed in Section 3.7.1, it is critical for the cantilever to reach thermal equilibrium before experiments. Hence,  $25^{\circ}\text{C}$  is the lower limit of this temperature study. The upper temperature limit of  $80^{\circ}\text{C}$  is chosen for AFM stability. Above  $80^{\circ}\text{C}$ , convection current inside the fluid cell makes measurement instable. In addition, bubbles form easily on the cantilever, causing the cantilever to bend quickly over time. Even with the sealed fluid cell, water vapor was able to escape, causing the fluid cell to lose water rapidly.

## 8.2.4 Renormalization of forces

The thermal AFM cantilever calibration procedure introduces approximately 10% error to the spring constant. Therefore, the force values from separate sets of experiments

(each set using the same cantilever) differ (Figure 8.3A). Because each set of experiment uses the same cantilever, the trend within each set is preserved. Therefore, the differences between different sets can be scaled to the same level. Each set of experiment is linearly scaled such that the sum of the standard deviation of each data point is minimized. The result is that all data points from different sets of experiments are condensed as shown in Figure 8.3B.

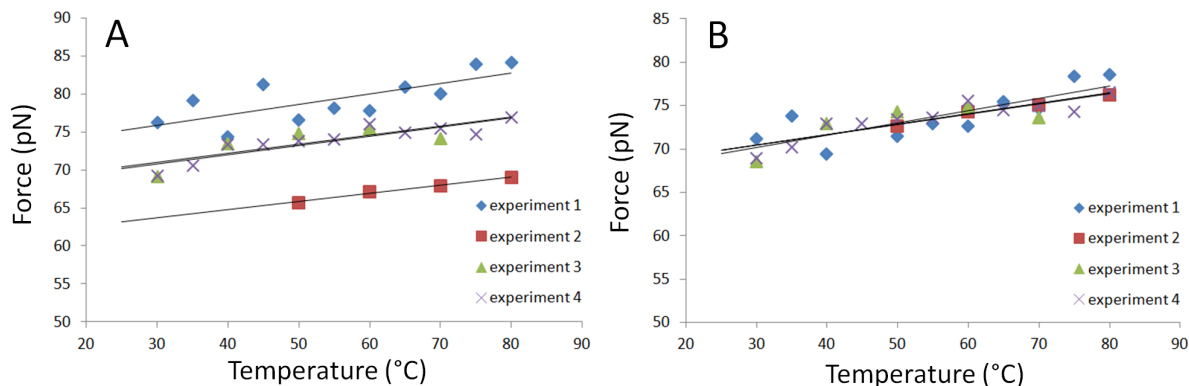


Figure 8.3: Normalizing the temperature dependence data from several independent experiments. Lines are linear fit to each set of experiment. A. Raw data for 4 independent experiments showing large inconsistencies due to AFM cantilever calibration. B. After normalizing, all data overlaps.

### 8.3 Single chain hydration responsible for force plateau in all three polymers

Using atomic force microscopy (AFM), a single polymer chain can be pulled from a naturally collapsed state to a hydrated, extended state as illustrated in (Figure 5.1). It has been predicted theoretically and shown in simulations that forced hydration of a collapsed hydrophobic polymer produces a constant force-distance profile (Figure 5.2) [57, 35, 66]. Force-extension curves of single hydrophobic polymers such as PS, PtBS and PVBP show characteristic constant force plateaus corresponding to single chain hydration [105, 60, 155, 168], followed by entropic elastic stretching before the chain detaches from the AFM cantilever or the Si substrate (Figure 5.2 and Figure 5.3). Statistical analysis of the force plateau magnitudes from thousands of independent molecular pulling events at a given temperature for a given polymer shows a quantized distribution (Figure 5.11), which suggests that the lowest force plateau results from hydration of a single polymer chain. Furthermore, when normalized to the same contour length, the force curves can be

superimposed on top of one another (Figure 5.12), showing that the polymer chains have the same persistence length and that the physics behind the forced hydration is length independent within the range of polymer sizes accessible to our experiment (hundreds of nm). The constant force profile is an indication that  $\Delta G^{hyd}$  for each monomer on the chain is identical within experimental accuracy; and its contribution to the total  $\Delta G^{hyd}$  of the extended chain is additive [105]. Surface topography scans of all three polymers samples confirm that they form compact globules on the Si surface (Figure 5.7 and Figure 8.4).

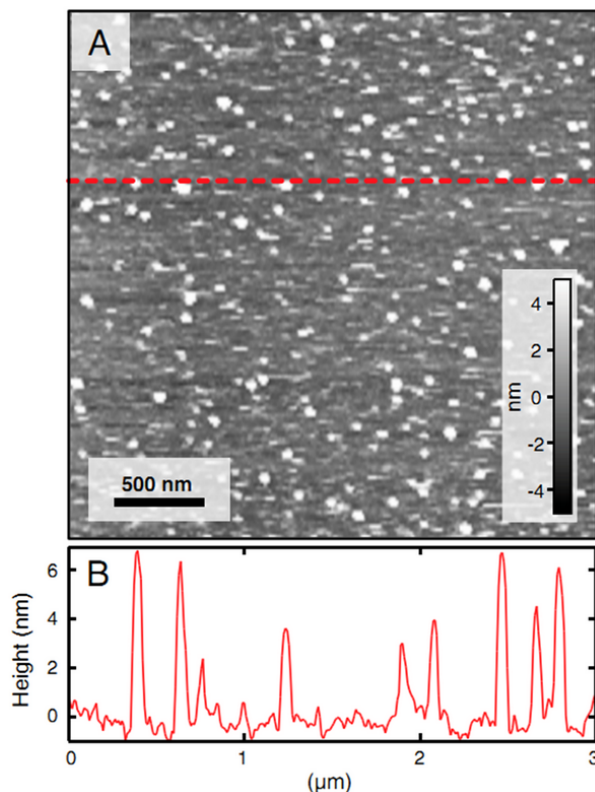


Figure 8.4: A. An AFM topography image of a PVBP sample shows single, isolated, PVBP molecules forming globules in water. The image is typical of hydrophobic polymer samples (PS, PtBS and PVBP) deposited on Si Surface used in this study. B. Cross-sectional profile of the red dashed line in A.

## 8.4 Temperature and size dependencies of single chain hydration

The effect of polymer side-chain size on the  $\Delta G^{hyd}$  of an extended polymer is investigated [106]. Evidence from small molecule  $\Delta G^{hyd}$  illustrates that molecular size does

not necessarily correlate with the magnitude of hydration  $\Delta G^{hyd}$  due to differences in solvent-solute attraction. However, the temperature dependence of hydration  $\Delta G^{hyd}$  contains rich information on hydration entropy and enthalpy, which allows probing of the effect of molecular size on hydrophobic hydration.

### 8.4.1 PS unfolding energy is temperature dependent

Large hydrophobic particles (radius much greater than 1 nm) behave differently from small ones (radius smaller than 1 nm). In the macroscopic limit, the temperature dependence of the  $\Delta G^{hyd}$  of large solutes is well described by interfacial thermodynamics. This implies that the temperature dependence of macroscopic  $\Delta G^{hyd}$  follows similar decreasing trend of the surface tension of water when temperature rises. The macroscopic phenomenon is surface area dominated and enthalpy driven as the number of disrupted water H-bonds at the interface scales with the surface area. For length scales less than 1 nm,  $\Delta G^{hyd}$  of a hydrophobic solute is predicted to scale with its volume rather than surface area [112, 74, 76, 13]. In contrast to the temperature dependence of macroscopic interfacial tension,  $\Delta G^{hyd}$  for a hydrophobic solute increases at low temperature, reaches a maximum and decreases at high temperature. This temperature dependence has been observed for small hydrocarbon molecules [181], and has been reproduced by many theoretical studies [83, 162, 74, 75]. This anomalous increase in  $\Delta G^{hyd}$  before the turnover point is believed to originate from the lowered entropy of water molecules adjacent to the small hydrophobic molecules, as the degrees of freedom of these water molecules are reduced by the formation of more ordered, dynamic structures.

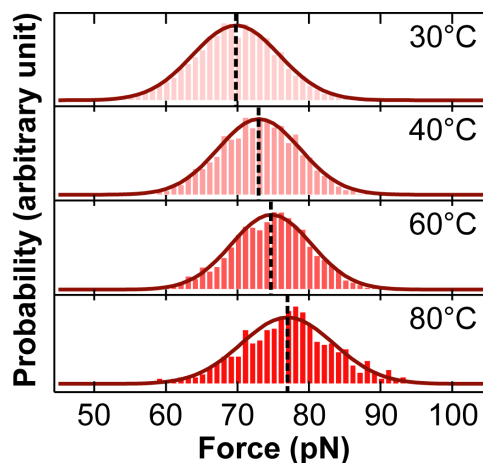


Figure 8.5: PS plateau force histograms show a steady increase of the mean force value as temperature increases.

To examine whether hydrophobic macromolecules follow a macroscopic or microscopic

temperature dependence, the hydration of a single PS chain in water was studied at temperatures ranging from 30°C to 80°C. Force plateaus from approximately two thousand force-extension curves corresponding to independent single chain pulling events show Gaussian distributions of the plateau force at each given temperature (Figure 8.5). The mean plateau force increases monotonically as a function of temperature (Figure 8.5 and Figure 8.6). An increase of roughly 7 pN in the mean plateau force from 30°C to 80°C corresponds to a 10% increase in the absolute value of the plateau force. A mean force resolution of less than 5 pN, below the thermal noise floor of  $\sim 20$  pN in typical AFM force spectroscopy, was achieved from a large sample population that forms well defined Gaussian distributions.  $\Delta G^{hyd}$  is calculated from the work done in the plateau region of the force curve by subtracting the entropic contribution from a single polystyrene chain using a method described previously [105]; the value of  $\Delta G^{hyd}$  ranges from 5.6 kJ/mol at 30°C to 6.1 kJ/mol at 80°C for PS (Table 8.1 and Figure 8.6).

$T$ (°C)	PS: $F$ (pN)	PtBS: $F$ (pN)	PVBP: $F$ (pN)
25		$65.11 \pm 4.08$	$67.75 \pm 3.13$
30	$69.54 \pm 1.90$	$70.17 \pm 1.13$	$70.18 \pm 2.15$
35	$71.69 \pm 2.08$	$71.97 \pm 3.04$	$74.43 \pm 1.31$
40	$72.54 \pm 1.38$	$74.31 \pm 1.44$	$75.06 \pm 5.28$
45	$72.93 \pm 1.66$	$74.69 \pm 0.98$	$75.66 \pm 1.17$
50	$73.05 \pm 1.10$	$75.55 \pm 2.54$	$77.79 \pm 1.09$
55	$73.40 \pm 0.42$	$76.37 \pm 2.68$	$74.90 \pm 1.68$
60	$74.78 \pm 1.37$	$77.05 \pm 2.12$	$76.38 \pm 0.35$
65	$74.83 \pm 0.59$	$77.39 \pm 1.64$	$73.35 \pm 3.06$

Table 8.1: Experimental data of the temperature dependence of the plateau force.

### 8.4.2 Differences in temperature dependence due to side-chain sizes

To further characterize the nature of the temperature dependence of  $\Delta G^{hyd}$ , the effect of side-chain size was examined. Direct verification of the size dependence of  $\Delta G^{hyd}$  is experimentally challenging. Theoretical studies often use ideal spherical hydrophobic particles with well defined sub-nanometer radii. Experimentally, even the smallest nanoparticles are several nanometres in diameter; too large to study the length scale of interest concerning microscopic hydrophobic hydration. Differently sized hydrophobic molecules fall in the right size range for studying microscopic hydrophobic size dependency, but there is no single parameter to describe the ‘size’ of a molecule considering the different molecular geometry (molecules are usually not spheres) and interactions with

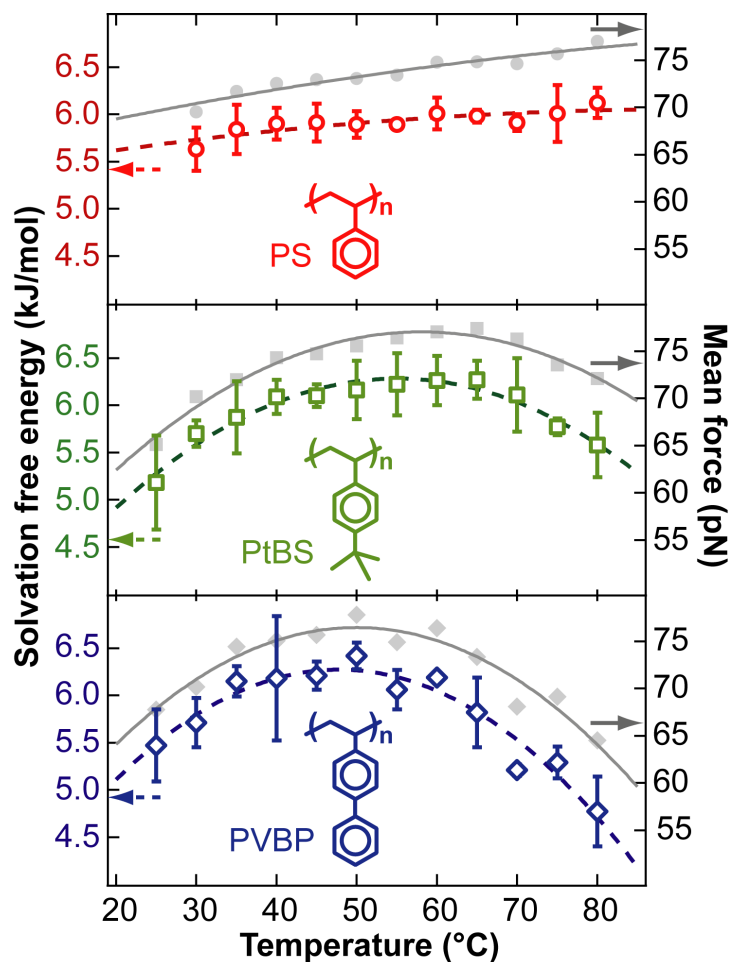


Figure 8.6: Experimental results of size and temperature dependencies on hydrophobic hydration. The temperature dependencies of plateau force (solid gray markers) and  $\Delta G^{hyd}$  (open colored markers) are shown in C, PS (circle), D, PtBS (box) and E, PVBP (diamond). Parabolic fits to the force (solid line) and  $\Delta G^{hyd}$  (dashed line) data illustrate their distinct dependencies on temperature. While the profile of  $\Delta G^{hyd}$  for PS is monotonically increasing, the profiles for PtBS and PVBP peak at 55.1 $^{\circ}\text{C}$  and 47.8 $^{\circ}\text{C}$ , respectively. The vertical error bars reflect the standard deviations of the mean from different sets of measurements.

water. These complications make it difficult to interpret direct comparison of  $\Delta G^{hyd}$  with molecular size even when good correlation exists, such as in the case of linear alkanes. However, one can verify the effect of molecular size on hydrophobic hydration by examining the effect of size on the temperature dependence of  $\Delta G^{hyd}$ .

The  $\Delta G^{hyd}$  of small (1–3 Å) non-polar molecules monotonically increases with temperature in the experimentally accessible range as in the case of short-chain alkanes and noble gases. Larger non-polar molecules ( $< 10$  Å) such as benzene and toluene exhibit a different characteristic temperature dependence of  $\Delta G^{hyd}$ , which increases with temperature and reaches a maximum before it decreases as temperature continues to rise. Once the particle size is greater than a few nanometers, its  $\Delta G^{hyd}$  follows macroscopic interfacial thermodynamics, which monotonically decreases as temperature rises. Theories on small particle hydration have shown that as the particle size increases, the temperature at which  $\Delta G^{hyd}$  is maximized will shift lower, providing a smooth transition between the temperature dependence of  $\Delta G^{hyd}$  from small to large solute 21, 23, 28.

To examine this effect, two other hydrophobic polymers with identical backbones but side-chains of different sizes were used: poly(4-tert-butylstyrene) (PtBS) and poly(4-vinylbiphenyl) (PVBP) with calculated monomer sizes (backbone + side-chain) of  $\sim 9.5$  Å and  $\sim 11.4$  Å, respectively. Both polymers' monomers are larger than that of PS ( $\sim 7.2$  Å), but not large enough to fall into the macroscopic regime. The single molecule force-extension curves for PtBS and PVBP have the same features as PS due to the same physical phenomena (coil-globule transition and hydrophobic hydration) governing their shape.

Interestingly, the temperature dependences for the three polymers are different (Figure 8.6). We found that the unfolding force and  $\Delta G^{hyd}$  of PS monotonically increase with temperature (Figure 8.5 and Figure 8.6) while PtBS and PVBP show turn-over behavior at different temperatures (Figure 8.6). The turnover behavior is characteristic of solutes whose sizes lie in the cross-over regime between hydrophobic hydration of small ( $< 7$  Å) and large ( $> 20$  Å) solutes (Figure 2.1b) and are distinct from macroscopic interfacial thermodynamics (Figure 2.1a), indicating that the polymer hydration mechanism is determined by the microscopic scale of their side-chains. Fitting the  $\Delta G^{hyd}$  as a function of temperature to Equation 8.1 [5] yields turn-over temperatures of  $92 \pm 45^\circ\text{C}$ ,  $55.1 \pm 0.9^\circ\text{C}$ , and  $47.8 \pm 0.9^\circ\text{C}$  for PS, PtBS, and PVBP, respectively. The turn-over temperatures decrease as the size of the hydrophobic side-chain increases from 7.2 Å for PS to 9.5 Å for PtBS and 11.4 Å for PVBP, in agreement with theoretically predicted length scales [5, 74, 7] (Figure 2.2b). The different temperature dependencies of PS, PtBS and PVBP are direct results of the differing sizes of the side-chains. The vanished

hydration entropy at the turn-over temperature indicates a characteristic hydrophobic hydration length scale that is directly related to the microscopic-macroscopic cross-over length scales associated with this temperature.

$$G(T) = G(T_0) + (T - T_0)(C_p - S(T_0)) - T \ln\left(\frac{T}{T_0}\right) C_p \quad (8.1)$$

$$H(T) = H(T_0) + (T - T_0)C_p \quad (8.2)$$

$$S(T) = S(T_0) + \ln\left(\frac{T}{T_0}\right) C_p \quad (8.3)$$

The entropic and enthalpic contributions to the  $\Delta G^{hyd}$  can be separated (Figure 8.7) based on Equation (8.1), (8.2), and (8.3) (Equations 15a-c from Ashbaugh et al. [5]), assuming the heat capacity is constant over the temperature range. Both hydration entropy and enthalpy are negative at room temperature (Figure 8.7), in agreement with experimental small molecule (e.g. methane) data. The negative entropy indicates the local restructuring of water, while the negative enthalpy is due to the dispersive attractive interaction between polymer and water. The temperature and monomer size dependence of  $\Delta G^{hyd}$  are consistent with hydrophobic polymer unfolding simulations from Athawale et al. [7]. Their work suggests that the presence of the turnover behavior of  $\Delta G^{hyd}$  is the result of Lennard-Jones attraction between polymer and water. Ashbaugh et al. also showed that increasing attraction lowers the  $\Delta G^{hyd}$  and shifts the turn-over point to higher temperature [5]. A study from Huang et al. [75] showed that attraction between the solute and water does not significantly alter the turnover temperature of  $\Delta G^{hyd}$ , as the attraction does not contribute greatly to hydration entropy. In addition, the turnover temperature is much more sensitive to the size of the solute than the attraction between the solute and solvent [75].

As Figure 5.3 illustrates, the forced hydration process changes the conformation of the hydrophobic polymer from collapsed to extended state with constant tension. The tension on the extended, solvent exposed portion of the chain keeps that portion of the chain constantly extended at  $\sim 75\%$  of its contour length, which significantly lowers the entropy ( $\Delta S_{ext} < 0$ ) between the extended and relaxed conformations, both of which are fully hydrated. (Figure 5.3) Here, the fully hydrated, relaxed conformation is not a stable state accessible to our experiment as it would only exist transiently and undergo rapid hydrophobic collapse (shown by the reversible force curves in [105]). Such a transient state was considered in order to compute the free energy contributed from only hydration

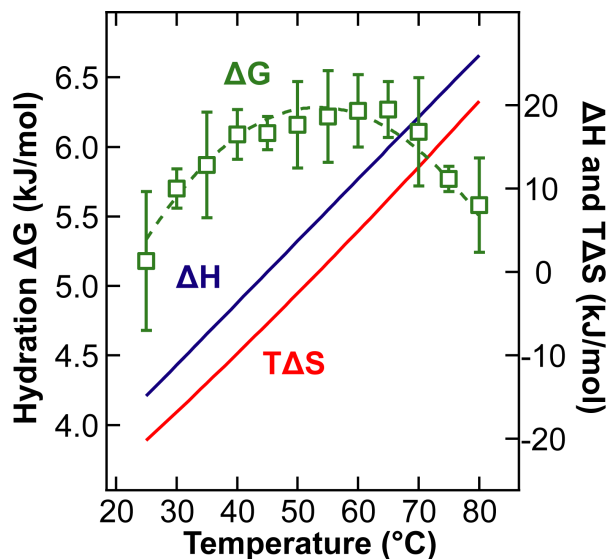


Figure 8.7: The temperature dependencies of hydration entropy (red), enthalpy (blue), and free energy (green) of PtBS.

as the chain unfolds. A fully hydrated, but extended state shares the same hydration contribution but also has a large free energy contribution from the reduced chain entropy  $\Delta S_{ext}$ . The temperature dependent contribution of  $T\Delta S_{ext}$  causes the turnover temperature of  $\Delta G^{hyd}$  to be lower than that of  $F(T)$  as shown in Figure 8.6.

### 8.4.3 Significance of the temperature and size dependence

The turnover behavior of the extended polymer  $\Delta G^{hyd}$  has an important ramification: the hydration entropy diminishes at a critical temperature corresponding to  $\Delta G^{hyd}$  maximum. The negative hydration entropy below this temperature suggests that the overall degree of conformational freedom of water is reduced surrounding the solute. Above the critical temperature, the thermal motion overcomes the restrained water molecules' confining potentials and the hydration entropy becomes positive. The results indicate that the critical temperature corresponding to zero hydration entropy decreases as the solute size increases. Therefore, at a given temperature, different mechanisms govern the hydration of hydrophobic side chains depending on their sizes. The negative hydration entropy at lower temperature suggests that water is more structurally organized around extended hydrophobic polymers. Even though the length of the polymer extends hundreds of nanometers, the size across the chain is sub-nanometer, which is small enough to allow water connectivity across the chain. Temperature dependence of extended polymer  $\Delta G^{hyd}$  showed similar size dependence as for small molecules, whose  $\Delta G^{hyd}$  per surface area decreases from macroscopic interfacial tension (when the spherical solute

radius exceeds  $\sim 1$  nm) to 0 as the solute size shrinks [32, 74, 75]. This places the interaction between extended polymers on the same small molecule length scale as their free monomer counterparts. The different nature of small molecule hydration from macroscopic interfacial energy warrants re-examining the hydrophobic interaction of polymers. In particular, the lower-than-SASA-predicted  $\Delta G^{hyd}$  suggests a weaker driving force for the association of hydrophobic residues in a chain.

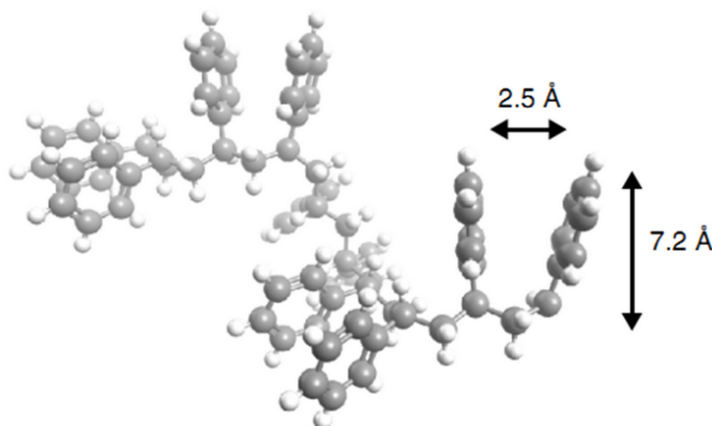


Figure 8.8: Molecular structure of a short segment of PS illustrates the approximate dimensions of the polymer. The diameter was taken as the longest distance between two atoms in the monomer. In the case of PS, the distance is 7.2 Å. The length per monomer along the chain is measured by adding bond length projections that total 2.5 Å.

However, free monomer  $\Delta G^{hyd}$  cannot be directly applied to polymer systems. As Figure 5.3 illustrates,  $\Delta G^{hyd}$  can be obtained by measuring free monomer solubility or transfer energy from the equilibrium between free monomers and their aggregates (similar to the collapsed state of a polymer). The change of  $\Delta G^{hyd}$  due to polymerization from free monomers to a polymer is significant, as the magnitude of  $\Delta G^{hyd}$  of free monomers is 3–4 times greater than that assigned to repeated units on the polymer. This is not surprising when a realistic picture of the polymer is considered: for PS, the size of each monomer from the back-bone to the end of the side chain is approximately 7.2 Å, whereas the distance between adjacent monomers is only 2.5 Å (Figure 8.8). The proximity of neighboring side chains indicates that there are likely significant hydrophobic interactions between them. As a result, the net free energy required to hydrate each sandwiched monomer unit on the chain is reduced compared to the free energy required to hydrate a free monomer without neighbors. Therefore, the resulting estimated driving force for hydrophobic collapse of a chain is actually much lower than if one were to assume each monomer on the chain has the same  $\Delta G^{hyd}$  as a free monomer. Knowing  $\Delta G^{hyd}$  of free monomers from either transfer or solubility experiments may be insufficient to predict

the free energy of macromolecules, and the direct measurement of  $\Delta G^{hyd}$  in the system of interest by the single molecule technique presented here may be necessary for accurate assessment.

The temperature and monomer size dependence of  $\Delta G^{hyd}$  are consistent with hydrophobic polymer unfolding simulations from Athawale et al. [7]. Their work suggests that the turnover behavior of  $\Delta G^{hyd}$  is present only when a Lennard-Jones attraction between polymer and water is introduced. However, study from Huang et al. [75] indicates that attraction between solute and water does not significantly alter the turnover temperature of  $\Delta G^{hyd}$ , as the attraction does not add to the entropic contribution to the free energy. In experimental systems, it would be difficult to assess the contribution due to polymer-solvent attraction. Furthermore, it was pointed out that the turnover temperature is much more sensitive to the size of the solute than the attraction between solute and solvent [75]. The length of the polymer used in the experiment reported here is much greater (100s of nm) than the 25-mer ( $\sim 4$  nm) used in the simulation from Athawale et al. [7]. As a result, the experiment does not probe the finite size effect as the work of Athawale et al. did. In addition, since both area and volume of the extended polymer are proportional to the extended chain length, the experiment cannot directly test whether the extended polymer  $\Delta G^{hyd}$  is area or volume dependent.

Traditionally, the hydration of linear alkanes has been studied as a model for hydrophobic hydration and interaction. Similar to polymers, the lengths of linear alkanes can be increased (from  $\sim 3.5$  Å for methane to  $\sim 12.5$  Å for decane), while the cross-sectional diameter remains  $\sim 3.5$  Å. As shown below, the implications of these results are consistent with the existing linear alkane data. Data from transfer free energy experiment at 298K [1] show that  $\Delta G^{hyd}$  linearly correlates with alkane chain lengths of various hydrocarbons and derivatives (Figure 8.9), suggesting the total  $\Delta G^{hyd}$  is additive for each additional  $\text{CH}_2$  at a given temperature [178]. The additive effect is consistent with the finding that, for a linear macromolecule,  $\Delta G^{hyd}$  of the extended state is the sum of the contributions by individual monomers along the chain. The additive nature implies that the temperature dependence of  $\Delta G^{hyd}$  for the whole extended polymer chain is identical to  $\Delta G^{hyd}$  of a single repeated unit on the chain, independent of the chain length. The temperature dependence of linear alkane hydration energies shows weak length dependence from methane to nonane even though the length spans from the microscopic to the macroscopic thermodynamics regimes. To explain this, one must distinguish the different molecular geometries – the size of a linear molecule such as alkane and polymer cannot be characterized by its length, whereas size dependence in theoretical studies usually refers to the radii of spherical particles. In addition, there are significant hydrophobic

interactions between adjacent  $\text{CH}_2$  units on the linear alkane because the transfer free energy of methane from hexadecane to water is 16.6 kJ/mol, but the additional transfer free energy for each additional  $\text{CH}_2$  is only 4.7 kJ/mol (Figure 8.9).

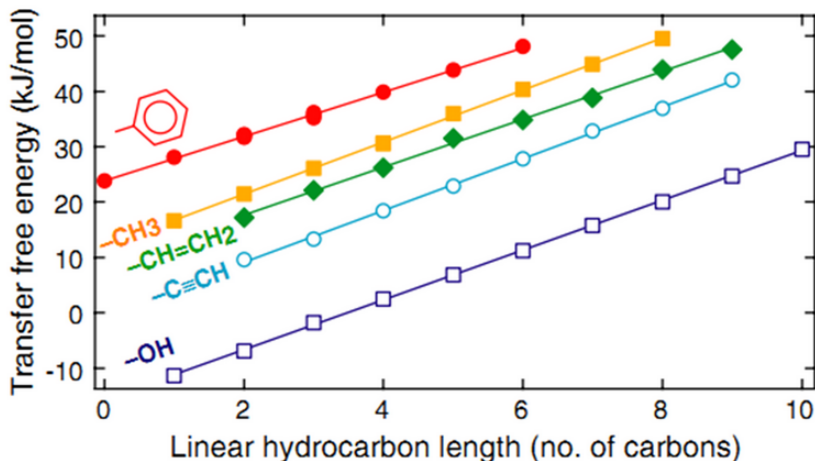


Figure 8.9: Transfer free energy from water to hexadecane at 298 K for various length alkanes with different functional groups: aromatic (red solid circle): benzene to hexylbenzene, alkane (yellow solid square): methane to octane, alkene (green solid diamond): ethene to nonene, alkyne (cyan open circle): ethyne to nonyne, alcohol (blue open square): methanol to decanol. The horizontal axis shows the length of the alkane chain attached to these functional groups. Solid lines show linear fit to the data. The numerical values of the data come from published tables of transfer free energy [1].

This work adds an important piece to the puzzle of hydrophobic solvation. It is worth noting that in previous work the solvation free energy was shown to correlate with interfacial tension when both monomer size and temperature were kept constant; the only varying parameter being the chemical composition of the solvent [105, 184]. The results of this study show that, in the more general case, one should include a temperature  $T$  dependence in both the monomer  $\Delta G^{hyd}$  and the solvent quality terms in the simple total solvation free energy expression for the extension of the polymer  $\Delta G_{total}^{solv}$  [105]:

$$\Delta G_{total}^{solv}(T) = \Delta G^{hyd}(r, T)\chi(T)N \quad (8.4)$$

where  $r$  is the size of monomers on the chain,  $\Delta G^{hyd}$  is the hydration free energy per monomer on the chain in pure water,  $N$  is the number of solvent exposed monomers and  $\chi(T)$  is the relative solvent quality correction factor defined by the ratio between solvent-polymer and water-polymer interfacial free energies ( $\gamma_{sp}$  and  $\gamma_{wp}$ ):

$$\chi(T) = \frac{\gamma_{sp}(T)}{\gamma_{wp}(T)} \quad (8.5)$$

We found that the overall free energy of collapse per monomer  $\sim 6$  kJ/mol is lower than the  $\Delta G^{hyd}$  of similarly sized monomers in the range of 20–30 kJ/mol. This is mainly due to the hydrophobic and dispersive interactions between adjacent side-chains (Figure 2.2c), which are sufficient to offset the reduction of solute configurational entropy going from free monomers to polymers.

Chandler showed that in the microscopic regime, the hydration free energy per unit area ( $\Delta G^{hyd}/A$ ) increases linearly with particle size, indicating an apparent volume-dependent scaling relation, which strengthens with temperature [32] (Figure 8.10). On the other hand,  $\Delta G^{hyd}/A$  in the macroscopic regime plateaus at the surface tension value, indicating an area-dependent scaling relation, which weakens with temperature [32] (Figure 8.10). Our observation of the thermal signature of  $\Delta G^{hyd}$  at different molecular sizes is the evidence for this view, suggesting that an entropically driven, volume scaling relationship exists for the microscopic length scale, as illustrated in Figure 8.11.

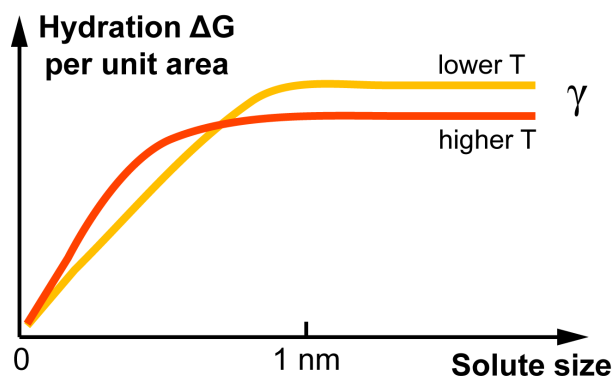


Figure 8.10: The effect of temperature on the size-dependence of hydration  $\Delta G^{hyd}/A$  (Adapted from Chandler [32]).

## 8.5 Other sources of possible temperature dependencies

Many physical processes are sensitive to temperature. This section investigates other potential sources of temperature dependencies that could lead to the observed effect. It was found that these sources are unlikely the cause of the temperature and size dependencies observed in the experiments.

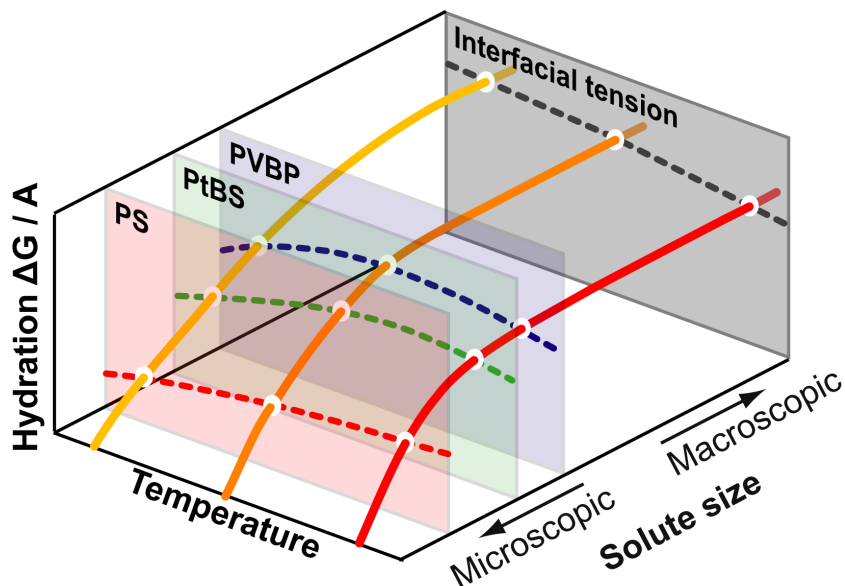


Figure 8.11: The observed temperature dependent hydration  $\Delta G^{hyd}/A$  are signatures of hydrophobic hydration at different length scales. This schematic relates the experimental results of polymers with different side-chain sizes to the theoretical hydrophobic size effect curves.

### 8.5.1 Temperature dependence of polymer desorption from surface

As discussed in Section 5.4, the surface desorption mechanism can also give rise to force plateau in the force-extension curves (Figure 5.6 and Figure 5.8) [36, 80, 81, 108, 43]. Whittington and colleagues have studied the forced desorption behavior of polymers from a surface by directed walk models [2, 138, 137]. Both two- and three-dimensional models used in their studies showed force-extension curves with a plateau, similar to what other experimental studies have concluded; the effects of temperature, finite length, and anchoring point on the pulling behavior were also investigated. A particularly interesting temperature dependence of the critical desorption force arises from their studies using three-dimensional directed walk model (Figure 8.12) [2]. Below the critical temperature ( $T_c$ ), a temperature dependent force plateau is present in the polymer desorption force curve. As the temperature rises from  $T = 0$  to  $T = T_c$ , the critical force needed to detach the polymer from the surface increases, then decrease (Figure 8.12A). At temperature above  $T_c$ , the polymer detaches from the surface spontaneously without mechanical force (Figure 8.12B). The phase diagram for polymer adsorption is shown in Figure 8.12C, above the phase transition curve, the polymer is desorbed from the surface; while below it, the polymer is adsorbed. The phase transition curve corresponds to the temperature

response of the force plateau in the force-extension curve, where adsorbed and desorbed polymer can coexist. Similar behavior for two-dimensional directed walk model was also observed, although the critical force monotonically decreases with temperature without any turn-over behavior [2].

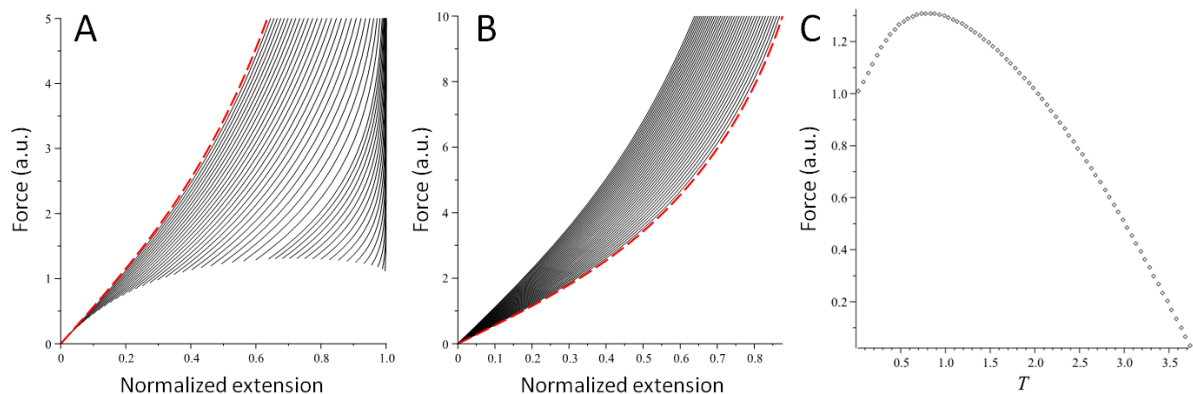


Figure 8.12: Temperature dependence of polymer desorption force curves, assuming one end of the polymer is attached to the surface, the other end is pulled away from the surface. A. Force-extension curves for  $T < T_c$ . B. Force-extension curves for  $T > T_c$ . Red dashed line corresponds to  $T = T_c$ . C. Phase diagram indicating the adsorbed and desorbed phases of the polymer, the phase transition line correspond to critical force for their coexistence. (Figure reproduced from Alvarez and Whittington [2].)

This is unlikely the cause for the temperature dependent plateau force as evidence suggests that the plateau force is not caused by polymer-surface adhesion (Section 5.4). Although the surface adhesion may contribute to the overall unfolding free energy to some extent, the hydrophobic effect is the dominant driving force in this case. The facts that the plateau force is surface independent (Section 5.4.2) but solvent dependent (Section 7.4, 7.5, and 7.6) are strong evidence that the polymer-surface interaction is weak in comparison to the solvent effect. In addition, pulling experiment by physisorption on a surface adsorbed polymer is unlikely to pull on the ends of the polymer. The force curves in such scenario will always contain a double step with identical step sizes. This is not what was observed in experiments for three reasons: first, single plateau force curves are the dominant events when surface density of polymer is low; second, the double/multiple plateau events are much better controlled by the polymer density on the surface, indicating that the plateaus are likely from independent chains; and third, the non-uniform plateau steps cannot be explained by polymer desorption mechanism (Section 5.4.3). Lastly, the temperature dependent plateau force observed in this experiment turns over more sharply than what was predicted by the surface desorption mechanism, as the extrapolated desorption force at  $T = 0$  K would be negative (see Figure 2.1, Fig-

ure 8.5, Figure 8.6, and Figure 8.7). Therefore, surface desorption mechanism is unlikely to contribute to the temperature dependence in this experiment.

Although not the case in this study, polymer surface interaction is one of the most important problems in surface and polymer science. Experimental evidence for temperature and polymer length dependencies of the critical desorption force is lacking and requires future investigations.

### 8.5.2 Temperature dependence of cantilever spring constant

The spring constant  $k_s$  of the cantilever is related to the Young's modulus of the cantilever material and its dimensions [64]:

$$k_s = \frac{Et^3w}{4L^3} \quad (8.6)$$

where  $E$  is the Young's modulus,  $t$  is the thickness,  $w$  is the width, and  $L$  is the length of the cantilever. The spring constant is linearly proportional to the Young's modulus. Since the dimensional change of the cantilever is negligible [173] from 20°C to 80°C, the only other contribution comes from the Young's modulus. The Young's modulus of both Si and Si<sub>3</sub>N<sub>4</sub> decreases by < 0.2% from 20°C to 80°C (Figure 8.13). This variation in spring constant is below the noise floor of our measurement and is insignificant comparing to the temperature dependent effect of  $\Delta G^{hyd}$ . It has been shown that the spring constant calibrated by the thermal method [90] has a weak temperature dependence [64, 145] of up to 5% from 20 to 80°C. This difference is a systematic error from the thermal calibration method rather than true spring constant differences [145]. Therefore, it is necessary that all initial spring constant calibrations of the AFM cantilever are performed within 5 degrees of ambient temperature.

### 8.5.3 Temperature dependence of the piezoelectric actuators

Although separated from the heated fluid cell, the temperature inside the AFM head was higher than the equilibrium operation temperature in the fluid. The piezoelectric actuator used for single molecule pulling is housed inside the AFM head, and will be affected by this uncontrolled temperature change. The piezoelectric coefficient has a temperature dependence of roughly 0.05% per degree K in the range between 0°C and 75°C (Figure 8.14), other studies have also shown the effect on piezoelectric sensitivity is negligible [120]. This corresponds to an upper bound of 2.5% change if the piezoelectric actuator's temperature follows the experimental temperature. The piezo sensitivity change

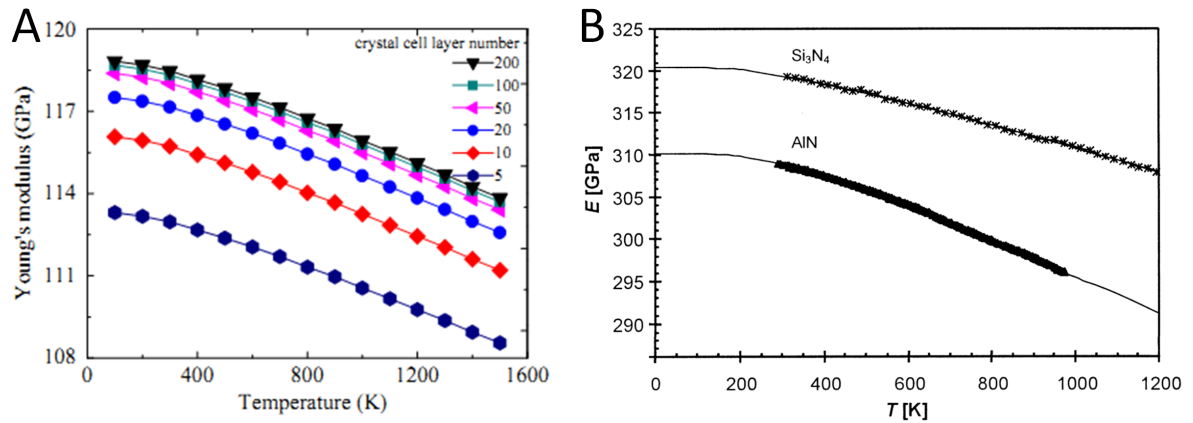


Figure 8.13: Temperature dependence of the Young's modulus of A. Si [173] and B. Si<sub>3</sub>N<sub>4</sub> [23]. (Figures adapted from Wang et al. [173] and Bruls et al. [23].)

directly affects the calibration of the cantilever's optical sensitivity (invOLS), if one were to use the factory calibrated room temperature piezo sensitivity for higher temperatures. Fortunately, the displacement of the piezoelectric actuator is separately monitored by a LVDT, which records the true displacement. Its measurement is completely independent from the piezo sensitivity, hence temperature independent. Therefore, the invOLS and subsequent force values would be influenced by temperature changes in the AFM head. All measurements in this study are based on the LVDT measurement, rather than the piezo sensitivity.

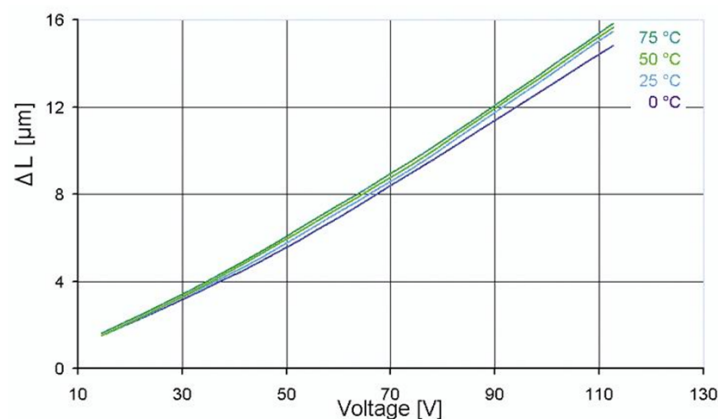


Figure 8.14: The effect of temperature on the piezoelectric actuator. (Figure adapted from Physik Instrumente [141].)

## 8.6 Conclusion

The experimental results presented here provide a fundamental description of the hydration of a single hydrophobic chain in water. The temperature dependencies of  $\Delta G^{hyd}$  for single chain PS, PtBS and PVBP differ from macroscopic interfacial thermodynamics specifically due to the small length scales of the monomer units along the chain. Furthermore,  $\Delta G^{hyd}(T)$  from the 3 polymers clearly showed the temperatures that correspond to  $\Delta G^{hyd}(T)$  maxima decrease, for increasing hydrophobic side-chain sizes. This trend provides an apparent transition from the monotonically increasing profile of  $\Delta G^{hyd}(T)$  for PS to the monotonically decreasing profile of a macroscopic hydrophobe. The results of this paper demonstrate that monomer size plays a key role in the origin of hydrophobic interaction energy in polymer systems from homopolymers to heteropolymers such as proteins. The length scale of amino acid is relevant here; the deviation of the actual  $\Delta G^{hyd}$  from the prediction of interfacial thermodynamics is significant to the folding and stability of proteins. When only a few hydrophobic residues associate, the resulting complex may not reach the length scale where the hydrophobic interaction is driven by the minimization of interfacial area; but rather, the energy to form the complex scales according to its volume. Therefore, the resulting hydrophobic complex should be rather weak and short-lived until the complex reaches a certain critical “nucleation” size, which may play a key role in the stability of early-stage protein folding. For instance, during the early stage of protein folding from a random coil, the path of hydrophobic association among different-sized hydrophobic core residues may be significant to the stability of particular intermediates. This work highlights the risks of underestimating how many amino acids are required to form a stable hydrophobic core of a protein.

# Chapter 9

## Summary and Future Work

### 9.1 Summary

Single molecule force spectroscopy was successfully applied to investigate the hydration behavior of hydrophobic polymers. In the end, a system was established where the behavior of hydrophobicity in polymers can be studied quantitatively. Due to their relatively simple structures, hydrophobic homopolymers were used to study hydrophobic collapse in both theories and experiments.

The mechanical unfolding behaviors of a single chain in different solvent conditions were studied from a theoretical perspective. Both an analytical and a lattice model indicated a force plateau in the force-extension curve is the signature of hydrophobic hydration of a single chain. Such force plateau signature was indeed observed in single molecule pulling experiment of hydrophobic polymer in aqueous solutions. Extensive control experiments were performed to study the nature of the observed force plateau. All evidences point to solvent effect as the main driving force behind the observed force plateau. To analyze and find single molecule events from the vast majority of force curves that contains nothing or contaminants, automated analysis programs were developed and tested to streamline data collection, filtering, conditioning, force curve analysis, and statistical analysis. Combining this with the techniques to control noise, drift and contamination in the AFM system produced large quantities of high precision data that allowed force variations below thermal noise floor to be revealed.

The ability to accurately determine the unfolding force, and thereby the hydration free energy per monomer has advanced the understanding of the size, temperature and solvent dependent hydration behavior of hydrophobic polymers. The results indicate that although the length of a polymer can be hundreds of nanometers long, its hydration behavior is dominated by the dimension of its monomers on the sub-nanometer length

scale. The temperature dependence of hydration free energy is highly sensitive to molecular size. From the temperature dependence of hydration free energy, we identified that the length scale crossing over from microscopic to macroscopic hydration is on the order of 1 nm, which is consistent with theoretical predictions. The apparent volume scaling relationship in this length regime implies that the hydrophobic driving force for small molecules to aggregate is smaller than what a surface area dependent model would predict. For instance, the stability of hydrophobic clusters in the folding intermediates may not be as stable as might be assumed, which may impact the folding pathway predictions. In addition, the turn-over points at a particular temperature signify the characteristic length scales where the entropic contribution of hydration is zero, which is indicative of the cross-over length scale of hydrophobic hydration at that temperature.

## 9.2 Ongoing and future work

Moving forward, several critical questions remain to be answered. Although spherical cavities in theoretical calculations showed interesting size dependent behavior, molecules are not spherical. An ongoing investigation shows that as the molecular size increases, its shape deviates further from being spherical. In fact, the molecular surface area is linearly proportional to the molecular volume for an almost exhaustive list of 118 small hydrocarbon molecules (Figure 9.1). The linear correlation of molecular surface area and molecular volume makes it difficult to assess the hydrophobic size effect at the sub-nanometer scale, i.e. whether the hydration free energy is surface area dependent or volume dependent. This indicates that a single parameter such as molecular volume or surface area may be insufficient to fully describe the hydrophobic size effect for real molecules. Further theoretical and experimental works are needed to understand how molecular geometry, solute-solvent attraction and surface chemistry heterogeneity affect a molecule's hydration behavior.

Another ongoing quest is to understand the ruggedness of the unfolding landscape (Figure 5.15 and Figure 9.2). When a constant force equal to plateau force is applied to the chain, the overall energy landscape is leveled. The ruggedness of the leveled landscape may provide information on the hydration mechanism of a single polymer unit right at the interface between the collapsed polymer and water. Every polymer unit at the interface can either go into the collapsed state, or stay hydrated. Therefore, the measurable total length of the extended state will undergo a one-dimensional random walk. Extensive single molecule force clamp studies have been carried out to characterize this random walk behavior. In a force clamp experiment, the force pulling on the polymer

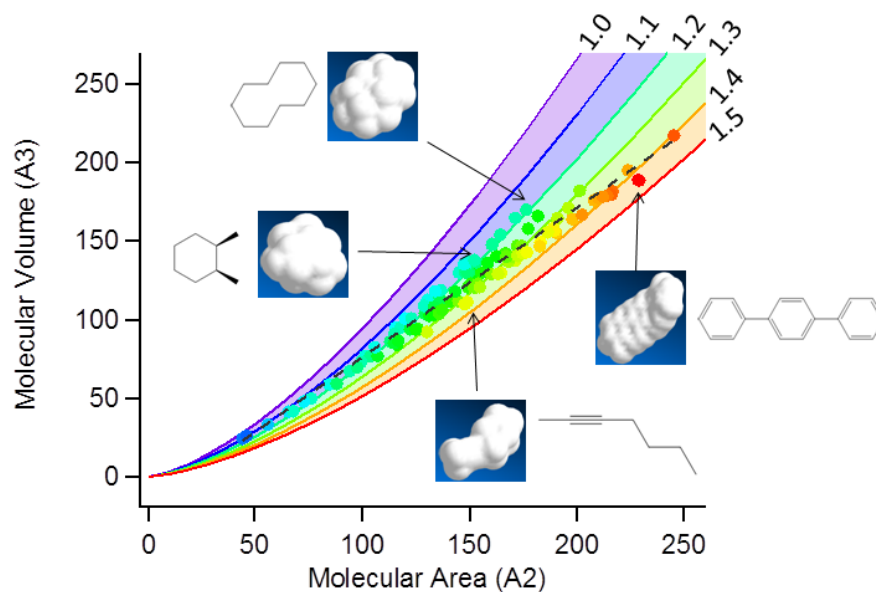


Figure 9.1: Molecular volume vs. area of 118 small hydrocarbons. The molecular surface is defined as the surface traced by the contact point of a spherical probe, representing the solvent molecule, as it is rolled over the target molecule. The solvent excluded volume is defined as the volume enclosed within the molecular surface. The graph is color coded by the ovality of the molecule, defined as the ratio of molecular surface area and the minimal surface area for the solvent excluded volume. A few representative molecules with their van der Waal surfaces are shown in the insets. The dashed line is a linear fit of the volume vs. area data.

is kept constant via a feedback mechanism that constantly adjusts the z-position of the cantilever such that a constant cantilever deflection is achieved. Unfortunately, due to the large size of the AFM cantilever (hundreds of  $\mu\text{m}$  in length) its thermal fluctuation due to surrounding water molecules overwhelms the molecular fluctuation from the tip attached single polymer. In addition, the solvent damping effect prevents short time-scale ( $< 1$  ms) force fluctuations from being directly detected. What the cantilever can pick up is the averaged molecular force fluctuation over 1 ms. Therefore, the force feedback mechanism falsely tracks the thermal fluctuation of the cantilever rather than real molecular events.

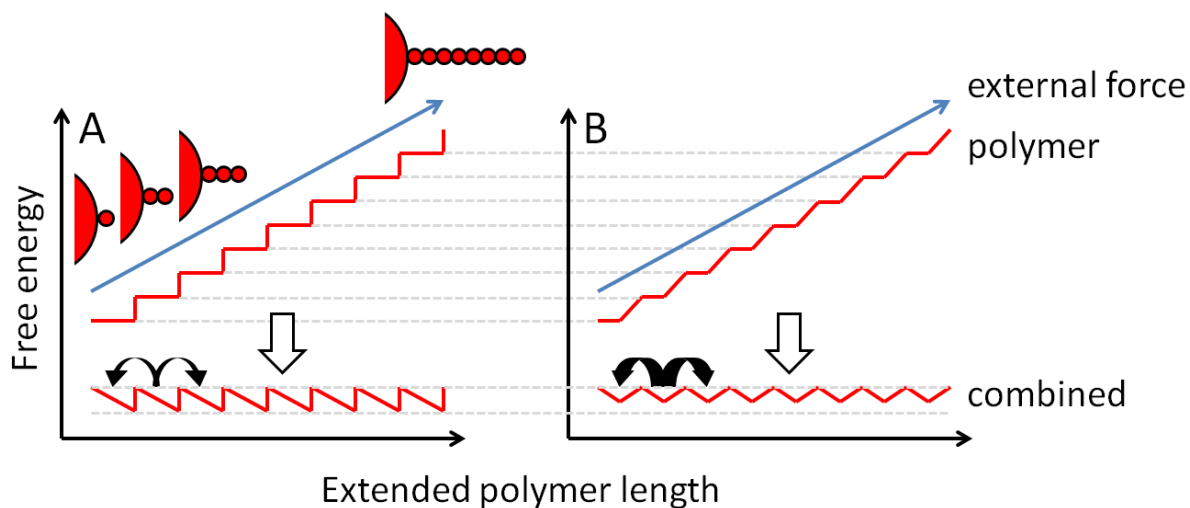


Figure 9.2: The rugged energy landscape of hydrophobic polymer unfolding. The stair function in red marks the free energy landscape of the polymer being hydrated, each step correspond to the hydration of an additional polymer unit. The blue arrow marks the energy provided by a constant force. The saw-tooth patterns at the bottom are the free energy landscapes of the combined system. Even though both require identical unfolding force, A. shows a more rugged landscape than B. Therefore, the energy barrier in the combined energy landscape in A is higher than B. As a result, B is closer to thermal equilibrium and has a shorter transition life. Experimentally, the velocity dependency in A. would be more pronounced than in B.

Although the molecular force fluctuation is smaller than the thermal fluctuation, they are still convoluted, making it possible to be detected via dynamic force spectroscopy. However, as Section 5.4.7 mentioned, no statistically significant velocity dependence was observed for pulling velocities from 500 nm/s to 3000 nm/s, as a result of the molecular system being close to equilibrium in this time scale. Ongoing studies using faster data acquisition card is able to extend the pulling velocity up to 40  $\mu\text{m}/\text{s}$  where a small but noticeable velocity dependency emerged (Figure 9.3). A modest increase of  $\sim 3$  pN in

plateau force over the velocity range is promising. Velocity dependent forces are usually associated with energy barrier crossing events, which in this case is an indication of the ruggedness of the unfolding free energy surface. Performing and analyzing pulling experiment at such high pulling velocity is technically challenging, as the requirement for sensitivity is even higher than the temperature dependent studies. Further investigations are needed to understand: 1. the effects of viscosity differences due to surface proximity, 2. how sampling frequency and the number of data points affect the statistical distribution, 3. the half time for cantilever to recover from rupture events (ringing), and 4. how the intrinsic force fluctuation changes at different velocities.

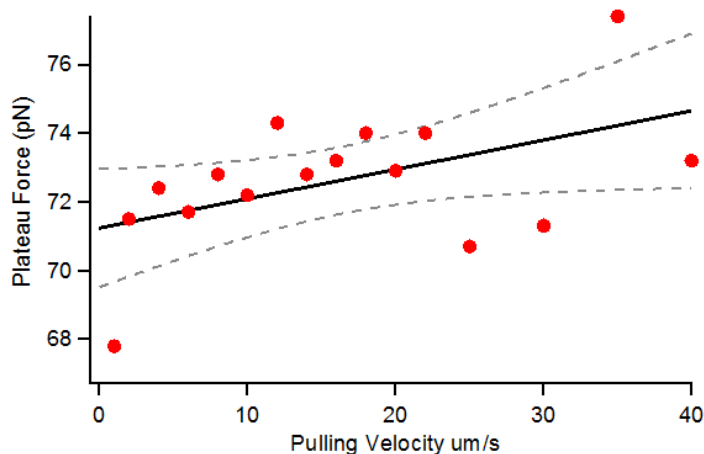


Figure 9.3: Velocity dependent plateau force at very high pulling velocities. Data point at each velocity is marked by a red circles. A linear fit (solid black line) and a 95% confidence interval (dashed grey curves) indicate an overall positive correlation between force and pulling velocity.

Another critical question that can be addressed by the system presented here is to understand the effects of urea and guanidine hydrochloride (GdnHCl) on polymer hydrophobic collapse. Both urea and GdnHCl are commonly used protein denaturant agents; however, their denaturation mechanisms are elusive. Whether the driving force behind protein denaturation is due to water structure breaking or denaturant-protein interaction is actively debated. It is expected that single polymer unfolding studies in these solvents may be able to put an end to this debate.

Lastly, interfaces represent important loci for biomolecular interactions; the effect of surface chemistry and surface patterning on polymer hydrophobic collapse is important for understanding protein-surface interactions such as denaturation and aggregation. Garde et al predicted intriguing behaviors of hydrophobic polymers at hydrophobic interfaces [91], which is still a challenge to experimentalists.

We have entered a golden age where single molecule experiments and simulations can be compared. We expect that the synergy between experiment and theory in the area of hydrophobic hydration will accelerate our understanding of molecular hydrophobicity and improve our ability to include it in biomolecular engineering.

# Bibliography

- [1] M. H. Abraham, G. S. Whiting, R. Fuchs, and E. J. Chambers. Thermodynamics of solute transfer from water to hexadecane. *Journal of the Chemical Society-Perkin Transactions 2*, (2):291–300, 1990.
- [2] J. Alvarez and S. G. Whittington. Force-extension relations for adsorbing polymers subject to a force. *Journal of Statistical Mechanics-Theory and Experiment*, page 04016, 2009.
- [3] H. S. Ashbaugh. Entropy crossover from molecular to macroscopic cavity hydration. *Chemical Physics Letters*, 477(1-3):109–111, 2009.
- [4] H. S. Ashbaugh, E. W. Kaler, and M. E. Paulaitis. A "universal" surface area correlation for molecular hydrophobic phenomena. *Journal of the American Chemical Society*, 121(39):9243–9244, 1999.
- [5] H. S. Ashbaugh and L. R. Pratt. Colloquium: Scaled particle theory and the length scales of hydrophobicity. *Reviews of Modern Physics*, 78(1):159–178, 2006.
- [6] Asylum-Research. Closed fluid cell data sheet, 2012.
- [7] M. V. Athawale, G. Goel, T. Ghosh, T. M. Truskett, and S. Garde. Effects of lengthscales and attractions on the collapse of hydrophobic polymers in water. *Proceedings of the National Academy of Sciences of the United States of America*, 104(3):733–738, 2007.
- [8] P. Attard. Thermodynamic analysis of bridging bubbles and a quantitative comparison with the measured hydrophobic attraction. *Langmuir*, 16(10):4455–4466, 2000.
- [9] A. A. Bakulin, C. Liang, T. L. Jansen, D. A. Wiersma, H. J. Bakker, and M. S. Pshenichnikov. Hydrophobic solvation: A 2d ir spectroscopic inquest. *Accounts of Chemical Research*, 42(9):1229–1238, 2009.

- [10] R. L. Baldwin. Temperature-dependence of the hydrophobic interaction in protein folding. *Proceedings of the National Academy of Sciences of the United States of America*, 83(21):8069–8072, 1986.
- [11] R. L. Baldwin. Energetics of protein folding. *Journal of Molecular Biology*, 371(2):283–301, 2007.
- [12] P. Ball. Water as an active constituent in cell biology. *Chemical Reviews*, 108(1):74–108, 2008.
- [13] D. Ben-Amotz. Global thermodynamics of hydrophobic cavitation, dewetting, and hydration. *Journal of Chemical Physics*, 123(18):184504, 2005.
- [14] D. Ben-Amotz and R. Underwood. Unraveling water’s entropic mysteries: A unified view of nonpolar, polar, and ionic hydration. *Accounts of Chemical Research*, 41(8):957–967, 2008.
- [15] B. J. Berne, J. D. Weeks, and R. H. Zhou. Dewetting and hydrophobic interaction in physical and biological systems. *Annual Review of Physical Chemistry*, 60:85–103, 2009.
- [16] R. B. Best, S. B. Fowler, J. L. Toca-Herrera, and J. Clarke. A simple method for probing the mechanical unfolding pathway of proteins in detail. *Proceedings of the National Academy of Sciences of the United States of America*, 99(19):12143–12148, 2002.
- [17] Jozef Bicerano. *Prediction of polymer properties*. Marcel Dekker, New York, 3rd edition, 2002.
- [18] G. Binnig, C. F. Quate, and C. Gerber. Atomic force microscope. *Physical Review Letters*, 56(9):930–933, 1986.
- [19] S. M. Biros, E. C. Ullrich, F. Hof, L. Trembleau, and J. Rebek. Kinetically stable complexes in water: The role of hydration and hydrophobicity. *Journal of the American Chemical Society*, 126(9):2870–2876, 2004.
- [20] F. Biscay, A. Ghoufi, and P. Malfreyt. Surface tension of water-alcohol mixtures from monte carlo simulations. *Journal of Chemical Physics*, 134(4), 2011.
- [21] C. Bouchiat, M. D. Wang, J. F. Allemand, T. Strick, S. M. Block, and V. Croquette. Estimating the persistence length of a worm-like chain molecule from force-extension measurements. *Biophysical Journal*, 76(1):409–413, 1999.

- [22] D. T. Bowron, A. Filipponi, M. A. Roberts, and J. L. Finney. Hydrophobic hydration and the formation of a clathrate hydrate. *Physical Review Letters*, 81(19):4164–4167, 1998.
- [23] R. J. Bruls, H. T. Hintzen, G. de With, and R. Metselaar. The temperature dependence of the young’s modulus of mgsin<sub>2</sub>, aln and si<sub>3</sub>n<sub>4</sub>. *Journal of the European Ceramic Society*, 21(3):263–268, 2001.
- [24] M. Brylinski, L. Konieczny, and I. Roterman. Hydrophobic collapse in (in silico) protein folding. *Computational Biology and Chemistry*, 30(4):255–267, 2006.
- [25] P. Buchanan, N. Aldiwan, A. K. Soper, J. L. Creek, and C. A. Koh. Decreased structure on dissolving methane in water. *Chemical Physics Letters*, 415(1-3):89–93, 2005.
- [26] C. Bustamante, J. F. Marko, E. D. Siggia, and S. Smith. Entropic elasticity of lambda-phage dna. *Science*, 265(5178):1599–1600, 1994.
- [27] Y. Cao, M. M. Balamurali, D. Sharma, and H. B. Li. A functional single-molecule binding assay via force spectroscopy. *Proceedings of the National Academy of Sciences of the United States of America*, 104(40):15677–15681, 2007.
- [28] Y. Cao and H. B. Li. Polyprotein of gb1 is an ideal artificial elastomeric protein. *Nature Materials*, 6(2):109–114, 2007.
- [29] A. Carambassis, L. C. Jonker, P. Attard, and M. W. Rutland. Forces measured between hydrophobic surfaces due to a submicroscopic bridging bubble. *Physical Review Letters*, 80(24):5357–5360, 1998.
- [30] M. Carrion-Vazquez, A. F. Oberhauser, S. B. Fowler, P. E. Marszalek, S. E. Broedel, J. Clarke, and J. M. Fernandez. Afm and chemical unfolding of a single protein follow the same pathway. *Biophysical Journal*, 76(1):A173–A173, 1999.
- [31] M. A. Cejas, W. A. Kinnney, C. Chen, J. G. Vinter, H. R. Almond, K. M. Balss, C. A. Maryanoff, U. Schmidt, M. Breslav, A. Mahan, E. Lacy, and B. E. Maryanoff. Thrombogenic collagen-mimetic peptides: Self-assembly of triple helix-based fibrils driven by hydrophobic interactions. *Proceedings of the National Academy of Sciences of the United States of America*, 105(25):8513–8518, 2008.
- [32] D. Chandler. Interfaces and the driving force of hydrophobic assembly. *Nature*, 437(7059):640–647, 2005.

- [33] M. S. Cheung, A. E. Garcia, and J. N. Onuchic. Protein folding mediated by solvation: Water expulsion and formation of the hydrophobic core occur after the structural collapse. *Proceedings of the National Academy of Sciences of the United States of America*, 99(2):685–690, 2002.
- [34] N. Choudhury and B. M. Pettitt. On the mechanism of hydrophobic association of nanoscopic solutes. *Journal of the American Chemical Society*, 127(10):3556–3567, 2005.
- [35] I. R. Cooke and D. R. M. Williams. Stretching polymers in poor and bad solvents: Pullout peaks and an unraveling transition. *Europhysics Letters*, 64(2):267–273, 2003.
- [36] S. X. Cui, C. J. Liu, Z. Q. Wang, and X. Zhang. Single molecule force spectroscopy on polyelectrolytes: Effect of spacer on adhesion force and linear charge density on rigidity. *Macromolecules*, 37(3):946–953, 2004.
- [37] J. R. Dann. Forces involved in adhesive process .1. critical surface tensions of polymeric solids as determined with polar liquids. *Journal of Colloid and Interface Science*, 32(2):302–320, 1970.
- [38] K. A. Dill, S. Bromberg, K. Z. Yue, K. M. Fiebig, D. P. Yee, P. D. Thomas, and H. S. Chan. Principles of protein-folding - a perspective from simple exact models. *Protein Science*, 4(4):561–602, 1995.
- [39] K. A. Dill, T. M. Truskett, V. Vlachy, and B. Hribar-Lee. Modeling water, the hydrophobic effect, and ion solvation. *Annual Review of Biophysics and Biomolecular Structure*, 34:173–199, 2005.
- [40] D. E. Discher and A. Eisenberg. Polymer vesicles. *Science*, 297(5583):967–973, 2002.
- [41] A. V. Dobrynin, M. Rubinstein, and S. P. Obukhov. Cascade of transitions of polyelectrolytes in poor solvents. *Macromolecules*, 29(8):2974–2979, 1996.
- [42] O. K. Dudko, G. Hummer, and A. Szabo. Theory, analysis, and interpretation of single-molecule force spectroscopy experiments. *Proceedings of the National Academy of Sciences of the United States of America*, 105(41):15755–15760, 2008.
- [43] M. Erdmann, R. David, A. Fornof, and H. E. Gaub. Electrically controlled dna adhesion. *Nature Nanotechnology*, 5(2):154–159, 2010.

- [44] J. C. Eriksson and U. Henriksson. Bridging-cluster model for hydrophobic attraction. *Langmuir*, 23(20):10026–10033, 2007.
- [45] E. Evans and K. Ritchie. Dynamic strength of molecular adhesion bonds. *Biophysical Journal*, 72(4):1541–1555, 1997.
- [46] M. Favre, S. K. Sekatskii, and G. Dietler. Single-molecule avidin-biotin association reaction studied by force-clamp spectroscopy. *Ultramicroscopy*, 108(10):1135–1139, 2008.
- [47] X. J. Feng, L. Feng, M. H. Jin, J. Zhai, L. Jiang, and D. B. Zhu. Reversible super-hydrophobicity to super-hydrophilicity transition of aligned zno nanorod films. *Journal of the American Chemical Society*, 126(1):62–63, 2004.
- [48] F. M. Fowkes. Determination of interfacial tensions, contact angles, and dispersion forces in surfaces by assuming additivity of intermolecular interactions in surfaces. *Journal of Physical Chemistry*, 66(2):382–382, 1962.
- [49] F. M. Fowkes. Additivity of intermolecular forces at interfaces .1. determination of contribution to surface and interfacial tensions of dispersion forces in various liquids. *Journal of Physical Chemistry*, 67(12):2538–2541, 1963.
- [50] F. M. Fowkes. Attractive forces at interfaces. *Industrial and Engineering Chemistry*, 56(12):40–52, 1964.
- [51] T. G. Fox and P. J. Flory. 2nd-order transition temperatures and related properties of polystyrene .1. influence of molecular weight. *Journal of Applied Physics*, 21(6):581–591, 1950.
- [52] B. S. Gerstman and P. P. Chapagain. Self-organization in protein folding and the hydrophobic interaction. *Journal of Chemical Physics*, 123(5):054901, 2005.
- [53] N. Giovambattista, P. G. Debenedetti, and P. J. Rossky. Enhanced surface hydrophobicity by coupling of surface polarity and topography. *Proceedings of the National Academy of Sciences of the United States of America*, 106(36):15181–15185, 2009.
- [54] N. Giovambattista, C. F. Lopez, P. J. Rossky, and P. G. Debenedetti. Hydrophobicity of protein surfaces: Separating geometry from chemistry. *Proceedings of the National Academy of Sciences of the United States of America*, 105(7):2274–2279, 2008.

- [55] G. Goel, M. V. Athawale, S. Garde, and T. M. Truskett. Attractions, water structure, and thermodynamics of hydrophobic polymer collapse. *Journal of Physical Chemistry B*, 112(42):13193–13196, 2008.
- [56] R. J. Good and L. A. Girifalco. A theory for estimation of surface and interfacial energies .3. estimation of surface energies of solids from contact angle data. *Journal of Physical Chemistry*, 64(5):561–565, 1960.
- [57] F. Gräter, P. Heider, R. Zangi, and B. J. Berne. Dissecting entropic coiling and poor solvent effects in protein collapse. *Journal of the American Chemical Society*, 130(35):11578–+, 2008.
- [58] G. Graziano. Scaled particle theory study of the length scale dependence of cavity thermodynamics in different liquids. *Journal of Physical Chemistry B*, 110(23):11421–11426, 2006.
- [59] G. Graziano. Significance of the tolman length at a molecular level. *Chemical Physics Letters*, 497(1-3):33–36, 2010.
- [60] N. Gunari, A. C. Balazs, and G. C. Walker. Force-induced globule-coil transition in single polystyrene chains in water. *Journal of the American Chemical Society*, 129(33):10046–10047, 2007.
- [61] N. Gunari and G. C. Walker. Nanomechanical fingerprints of individual blocks of a diblock copolymer chain. *Langmuir*, 24(10):5197–5201, 2008.
- [62] Z. G. Guo, F. Zhou, J. C. Hao, and W. M. Liu. Stable biomimetic superhydrophobic engineering materials. *Journal of the American Chemical Society*, 127(45):15670–15671, 2005.
- [63] A. N. Gupta, A. Vincent, K. Neupane, H. Yu, F. Wang, and M. T. Woodside. Experimental validation of free-energy-landscape reconstruction from non-equilibrium single-molecule force spectroscopy measurements. *Nature Physics*, 7(8):631–634, 2011.
- [64] U. Gysin, S. Rast, P. Ruff, E. Meyer, D. W. Lee, P. Vettiger, and C. Gerber. Temperature dependence of the force sensitivity of silicon cantilevers. *Physical Review B*, 69(4), 2004.
- [65] A. Halperin and E. B. Zhulina. On the deformation behavior of collapsed polymers. *Europhysics Letters*, 15(4):417–421, 1991.

- [66] A. Halperin and E. B. Zhulina. Stretching polymer brushes in poor solvents. *Macromolecules*, 24(19):5393–5397, 1991.
- [67] N. C. Harris, Y. Song, and C. H. Kiang. Experimental free energy surface reconstruction from single-molecule force spectroscopy using jarzynski’s equality. *Physical Review Letters*, 99(6), 2007.
- [68] B. J. Haupt, T. J. Senden, and E. M. Sevick. Afm evidence of rayleigh instability in single polymer chains. *Langmuir*, 18(6):2174–2182, 2002.
- [69] Herzan. Aek-2002 acoustic enclosure data sheet, 2011.
- [70] H. A. Heus, E. M. Puchner, A. J. van Vugt-Jonker, J. L. Zimmermann, and H. E. Gau. Atomic force microscope-based single-molecule force spectroscopy of rna unfolding. *Analytical Biochemistry*, 414(1):1–6, 2011.
- [71] S. Hofinger and F. Zerbetto. Simple models for hydrophobic hydration. *Chemical Society Reviews*, 34(12):1012–1020, 2005.
- [72] A. Honciuc and D. K. Schwartz. Probing hydrophobic interactions using trajectories of amphiphilic molecules at a hydrophobic/water interface. *Journal of the American Chemical Society*, 131(16):5973–5979, 2009.
- [73] C. Horejs, R. Ristl, R. Tscheliessnig, U. B. Sleytr, and D. Pum. Single-molecule force spectroscopy reveals the individual mechanical unfolding pathways of a surface layer protein. *Journal of Biological Chemistry*, 286(31):27416–27424, 2011.
- [74] D. M. Huang and D. Chandler. Temperature and length scale dependence of hydrophobic effects and their possible implications for protein folding. *Proceedings of the National Academy of Sciences of the United States of America*, 97(15):8324–8327, 2000.
- [75] D. M. Huang and D. Chandler. The hydrophobic effect and the influence of solute-solvent attractions. *Journal of Physical Chemistry B*, 106(8):2047–2053, 2002.
- [76] D. M. Huang, P. L. Geissler, and D. Chandler. Scaling of hydrophobic solvation free energies. *Journal of Physical Chemistry B*, 105(28):6704–6709, 2001.
- [77] X. Huang, C. J. Margulis, and B. J. Berne. Dewetting-induced collapse of hydrophobic particles. *Proceedings of the National Academy of Sciences of the United States of America*, 100(21):11953–11958, 2003.

- [78] X. H. Huang, R. H. Zhou, and B. J. Berne. Drying and hydrophobic collapse of paraffin plates. *Journal of Physical Chemistry B*, 109(8):3546–3552, 2005.
- [79] Arthur T. Hubbard. *Encyclopedia of surface and colloid science*. Marcel Dekker, New York, 2002.
- [80] T. Hugel, M. Grosholz, H. Clausen-Schaumann, A. Pfau, H. Gaub, and M. Seitz. Elasticity of single polyelectrolyte chains and their desorption from solid supports studied by afm based single molecule force spectroscopy. *Macromolecules*, 34(4):1039–1047, 2001.
- [81] T. Hugel and M. Seitz. The study of molecular interactions by afm force spectroscopy. *Macromolecular Rapid Communications*, 22(13):989–1016, 2001.
- [82] G. Hummer. Water pulls the strings in hydrophobic polymer collapse. *Proceedings of the National Academy of Sciences of the United States of America*, 104(38):14883–14884, 2007.
- [83] G. Hummer and S. Garde. Cavity expulsion and weak dewetting of hydrophobic solutes in water. *Physical Review Letters*, 80(19):4193–4196, 1998.
- [84] G. Hummer, S. Garde, A. E. Garcia, M. E. Paulaitis, and L. R. Pratt. Hydrophobic effects on a molecular scale. *Journal of Physical Chemistry B*, 102(51):10469–10482, 1998.
- [85] G. Hummer, S. Garde, A. E. Garcia, M. E. Paulaitis, and L. R. Pratt. The pressure dependence of hydrophobic interactions is consistent with the observed pressure denaturation of proteins. *Proceedings of the National Academy of Sciences of the United States of America*, 95(4):1552–1555, 1998.
- [86] G. Hummer, S. Garde, A. E. Garcia, M. E. Paulaitis, and L. R. Pratt. Role of hydrophobic interactions in pressure denaturation of proteins. *Biophysical Journal*, 74(2):A233–A233, 1998.
- [87] G. Hummer, S. Garde, A. E. Garcia, A. Pohorille, and L. R. Pratt. An information theory model of hydrophobic interactions. *Proceedings of the National Academy of Sciences of the United States of America*, 93(17):8951–8955, 1996.
- [88] G. Hummer, J. C. Rasaiah, and J. P. Noworyta. Water conduction through the hydrophobic channel of a carbon nanotube. *Nature*, 414(6860):188–190, 2001.

- [89] G. Hummer and A. Szabo. Free energy surfaces from single-molecule force spectroscopy. *Accounts of Chemical Research*, 38(7):504–513, 2005.
- [90] J. L. Hutter and J. Bechhoefer. Calibration of atomic-force microscope tips. *Review of Scientific Instruments*, 64(7):1868–1873, 1993.
- [91] S. N. Jamadagni, R. Godawat, and S. Garde. Hydrophobicity of proteins and interfaces: Insights from density fluctuations. *Annual Review of Chemical and Biomolecular Engineering, Vol 2*, 2:147–171, 2011.
- [92] H. Janovjak, J. Struckmeier, and D. J. Muller. Hydrodynamic effects in fast afm single-molecule force measurements. *European Biophysics Journal with Biophysics Letters*, 34(1):91–96, 2005.
- [93] A. Janshoff, M. Neitzert, Y. Oberdorfer, and H. Fuchs. Force spectroscopy of molecular systems - single molecule spectroscopy of polymers and biomolecules. *Angewandte Chemie-International Edition*, 39(18):3213–3237, 2000.
- [94] C. Jarzynski. Nonequilibrium equality for free energy differences. *Physical Review Letters*, 78(14):2690–2693, 1997.
- [95] J. P. Junker and M. Rief. Single-molecule force spectroscopy distinguishes target binding modes of calmodulin. *Proceedings of the National Academy of Sciences of the United States of America*, 106(34):14361–14366, 2009.
- [96] D. H. Kaelble and E. H. Cirlin. Dispersion and polar contributions to surface tension of poly(methylene oxide) and na-treated polytetrafluoroethylene. *Journal of Polymer Science Part a-2-Polymer Physics*, 9(2):363–368, 1971.
- [97] A. Kedrov, H. Janovjak, K. T. Sapra, and D. J. Muller. Deciphering molecular interactions of native membrane proteins by single-molecule force spectroscopy. *Annual Review of Biophysics and Biomolecular Structure*, 36:233–260, 2007.
- [98] M. S. Z. Kellermayer, S. B. Smith, H. L. Granzier, and C. Bustamante. Folding-unfolding transitions in single titin molecules characterized with laser tweezers. *Science*, 276(5315):1112–1116, 1997.
- [99] Werner Kern and Knovel (Firm). Handbook of semiconductor wafer cleaning technology science, technology, and applications, 1993.

- [100] A. Kiriy, G. Gorodyska, S. Minko, W. Jaeger, P. Stepanek, and M. Stamm. Cascade of coil-globule conformational transitions of single flexible polyelectrolyte molecules in poor solvent. *Journal of the American Chemical Society*, 124(45):13454–13462, 2002.
- [101] Y. Levy and J. N. Onuchic. Water and proteins: A love-hate relationship. *Proceedings of the National Academy of Sciences of the United States of America*, 101(10):3325–3326, 2004.
- [102] H. Li, A. Oberhauser, S. Fowler, J. Clarke, P. E. Marszalek, and J. M. Fernandez. Mechanical unfolding of titin is under kinetic control. *Biophysical Journal*, 78(1):402a–402a, 2000.
- [103] H. B. Li, B. B. Liu, X. Zhang, C. X. Gao, J. C. Shen, and G. T. Zou. Single-molecule force spectroscopy on poly(acrylic acid) by afm. *Langmuir*, 15(6):2120–2124, 1999.
- [104] H. B. Li, M. Rief, F. Oesterhelt, and H. E. Gaub. Single-molecule force spectroscopy on xanthan by afm. *Advanced Materials*, 10(4):316–319, 1998.
- [105] I. T. S. Li and G. C. Walker. Interfacial free energy governs single polystyrene chain collapse in water and aqueous solutions. *Journal of the American Chemical Society*, 132(18):6530–6540, 2010.
- [106] I. T. S. Li and G. C. Walker. Signature of hydrophobic hydration in a single polymer. *Proceedings of the National Academy of Sciences of the United States of America*, 108(40):16527–16532, 2011.
- [107] M. Li, L. Q. Liu, N. Xi, Y. C. Wang, Z. L. Dong, G. Y. Li, X. B. Xiao, and W. J. Zhang. Detecting cd20-rituximab interaction forces using afm single-molecule force spectroscopy. *Chinese Science Bulletin*, 56(35):3829–3835, 2011.
- [108] C. J. Liu, W. Q. Shi, S. X. Cui, Z. Q. Wang, and X. Zhang. Force spectroscopy of polymers: Beyond single chain mechanics. *Current Opinion in Solid State & Materials Science*, 9(3):140–148, 2006.
- [109] C. Y. Liu and H. Morawetz. Kinetics of the unfolding of collapsed polystyrene chains above the glass-transition temperature. *Macromolecules*, 21(2):515–518, 1988.
- [110] P. Liu, X. H. Huang, R. H. Zhou, and B. J. Berne. Observation of a dewetting transition in the collapse of the melittin tetramer. *Nature*, 437(7055):159–162, 2005.

- [111] X. P. Liu, M. J. S. Miller, M. S. Joshi, D. D. Thomas, and J. R. Lancaster. Accelerated reaction of nitric oxide with o-2 within the hydrophobic interior of biological membranes. *Proceedings of the National Academy of Sciences of the United States of America*, 95(5):2175–2179, 1998.
- [112] K. Lum, D. Chandler, and J. D. Weeks. Hydrophobicity at small and large length scales. *Journal of Physical Chemistry B*, 103(22):4570–4577, 1999.
- [113] S. Lynch, H. Baker, S. G. Byker, D. J. Zhou, and K. Sinniah. Single molecule force spectroscopy on g-quadruplex dna. *Chemistry-a European Journal*, 15(33):8113–8116, 2009.
- [114] D. Marenduzzo, A. Maritan, A. Rosa, and F. Seno. Stretching of a polymer below the theta point. *Physical Review Letters*, 90(8), 2003.
- [115] J. F. Marko and E. D. Siggia. Stretching dna. *Macromolecules*, 28(26):8759–8770, 1995.
- [116] B. T. Marshall, K. K. Sarangapani, J. H. Lou, R. P. McEver, and C. Zhu. Force history dependence of receptor-ligand dissociation. *Biophysical Journal*, 88(2):1458–1466, 2005.
- [117] P. E. Marszalek, H. Lu, H. B. Li, M. Carrion-Vazquez, A. F. Oberhauser, K. Schulten, and J. M. Fernandez. Mechanical unfolding intermediates in titin modules. *Nature*, 402(6757):100–103, 1999.
- [118] P. Y. Meadows, J. E. Bemis, and G. C. Walker. Single-molecule force spectroscopy of isolated and aggregated fibronectin proteins on negatively charged surfaces in aqueous liquids. *Langmuir*, 19(23):9566–9572, 2003.
- [119] R. Merkel, P. Nassoy, A. Leung, K. Ritchie, and E. Evans. Energy landscapes of receptor-ligand bonds explored with dynamic force spectroscopy. *Nature*, 397(6714):50–53, 1999.
- [120] C. Miclea, C. Tanasoiu, L. Amarande, C. F. Miclea, C. Plavitu, M. Cioangher, L. Trupina, C. T. Miclea, and C. David. Effect of temperature on the main piezoelectric parameters of a soft pzt ceramic. *Romanian Journal of Information Science and Technology*, 10(3):243–250, 2007.

- [121] T. F. Miller, E. Vanden-Eijnden, and D. Chandler. Solvent coarse-graining and the string method applied to the hydrophobic collapse of a hydrated chain. *Proceedings of the National Academy of Sciences of the United States of America*, 104(37):14559–14564, 2007.
- [122] D. D. L. Minh and A. B. Adib. Optimized free energies from bidirectional single-molecule force spectroscopy. *Physical Review Letters*, 100(18), 2008.
- [123] Minus. Bm-4 bench top vibration isolation platform specification sheet, 2012.
- [124] G. Mitchell, C. A. Lamontagne, R. Lebel, M. Grandbois, and F. Malouin. Single-molecule dynamic force spectroscopy of the fibronectin-heparin interaction. *Biochemical and Biophysical Research Communications*, 364(3):595–600, 2007.
- [125] S. Mitternacht, S. Luccioli, A. Torcini, A. Imparato, and A. Irback. Changing the mechanical unfolding pathway of fniii(10) by tuning the pulling strength. *Biophysical Journal*, 96(2):429–441, 2009.
- [126] V. Montana, W. Liu, U. Mohideen, and V. Parpura. Single molecule probing of exocytotic protein interactions using force spectroscopy. *Croatica Chemica Acta*, 81(1):31–40, 2008.
- [127] T. Mori, M. Asakura, and Y. Okahata. Single-molecule force spectroscopy for studying kinetics of enzymatic dextran elongations. *Journal of the American Chemical Society*, 133(15):5701–5703, 2011.
- [128] V. T. Moy, C. Yuan, A. Chen, and P. Kolb. Bond strength of individual ligand-receptor complexes measured by atomic force microscopy. *Molecular Biology of the Cell*, 10:75a–75a, 1999.
- [129] K. C. Neuman and A. Nagy. Single-molecule force spectroscopy: optical tweezers, magnetic tweezers and atomic force microscopy. *Nature Methods*, 5(6):491–505, 2008.
- [130] K. Neupane, H. Yu, D. A. N. Foster, F. Wang, and M. T. Woodside. Single-molecule force spectroscopy of the add adenine riboswitch relates folding to regulatory mechanism. *Nucleic Acids Research*, 39(17):7677–7687, 2011.
- [131] S. P. Ng, R. W. S. Rounsevell, A. Steward, C. D. Geierhaas, P. M. Williams, E. Paci, and J. Clarke. Mechanical unfolding of tfn3: The unfolding pathway of

- a fniii domain probed by protein engineering, afm and md simulation. *Journal of Molecular Biology*, 350(4):776–789, 2005.
- [132] Z. H. Nie, D. Fava, E. Kumacheva, S. Zou, G. C. Walker, and M. Rubinstein. Self-assembly of metal-polymer analogues of amphiphilic triblock copolymers. *Nature Materials*, 6(8):609–614, 2007.
- [133] S. Y. Noskov, G. Lamoureux, and B. Roux. Molecular dynamics study of hydration in ethanol-water mixtures using a polarizable force field. *Journal of Physical Chemistry B*, 109(14):6705–6713, 2005.
- [134] A. Noy. Force spectroscopy 101: how to design, perform, and analyze an afm-based single molecule force spectroscopy experiment. *Current Opinion in Chemical Biology*, 15(5):710–718, 2011.
- [135] T. Odijk. Stiff chains and filaments under tension. *Macromolecules*, 28(20):7016–7018, 1995.
- [136] Olympus. Micro cantilever product line, 2012.
- [137] E. Orlandini and M. C. Tesi. Modelling the adsorption of a polymer subject to an elongational force by directed walk models. *Journal of Mathematical Chemistry*, 45(1):72–94, 2009.
- [138] E. Orlandini, M. C. Tesi, and S. G. Whittington. Adsorption of a directed polymer subject to an elongational force. *Journal of Physics a-Mathematical and General*, 37(5):1535–1543, 2004.
- [139] D. K. Owens. Some thermodynamic aspects of polymer adhesion. *Journal of Applied Polymer Science*, 14(7):1725–1730, 1970.
- [140] G. T. Pickett and A. C. Balazs. Conformations of bridging polyelectrolytes in poor solvent: Single-chain self-consistent field calculations. *Langmuir*, 17(16):5111–5117, 2001.
- [141] Piezo-University. Piezo-university - environmental conditions and influences, 2011.
- [142] L. R. Pratt. Molecular theory of hydrophobic effects: "she is too mean to have her name repeated.". *Annual Review of Physical Chemistry*, 53:409–436, 2002.
- [143] L. R. Pratt and D. Chandler. Theory of hydrophobic effect. *Journal of Chemical Physics*, 67(8):3683–3704, 1977.

- [144] J. Qvist and B. Halle. Thermal signature of hydrophobic hydration dynamics. *Journal of the American Chemical Society*, 130(31):10345–10353, 2008.
- [145] A. Radenovic, E. Bystrenova, L. Libioulle, F. Valle, G. T. Shubeita, S. Kasas, and G. Dietler. Characterization of atomic force microscope probes at low temperatures. *Journal of Applied Physics*, 94(6):4210–4214, 2003.
- [146] S. Rajamani, T. M. Truskett, and S. Garde. Hydrophobic hydration from small to large lengthscales: Understanding and manipulating the crossover. *Proceedings of the National Academy of Sciences of the United States of America*, 102(27):9475–9480, 2005.
- [147] J. C. Rasaiah, S. Garde, and G. Hummer. Water in nonpolar confinement: From nanotubes to proteins and beyond. *Annual Review of Physical Chemistry*, 59:713–740, 2008.
- [148] C. Ray, J. R. Brown, and B. B. Akhremitchev. Single-molecule force spectroscopy measurements of "hydrophobic bond" between tethered hexadecane molecules. *Journal of Physical Chemistry B*, 110(35):17578–17583, 2006.
- [149] C. Ray, J. R. Brown, A. Kirkpatrick, and B. B. Akhremitchev. Pairwise interactions between linear alkanes in water measured by afm force spectroscopy. *Journal of the American Chemical Society*, 130(30):10008–10018, 2008.
- [150] M. Rief, M. Gautel, F. Oesterhelt, J. M. Fernandez, and H. E. Gaub. Reversible unfolding of individual titin immunoglobulin domains by afm. *Science*, 276(5315):1109–1112, 1997.
- [151] M. Rief, F. Oesterhelt, B. Heymann, and H. E. Gaub. Single molecule force spectroscopy on polysaccharides by atomic force microscopy. *Science*, 275(5304):1295–1297, 1997.
- [152] M. Rief, J. Pascual, M. Saraste, and H. E. Gaub. Single molecule force spectroscopy of spectrin repeats: Low unfolding forces in helix bundles. *Journal of Molecular Biology*, 286(2):553–561, 1999.
- [153] P. J. Rossky. Exploring nanoscale hydrophobic hydration. *Faraday Discussions*, 146:13–18, 2010.
- [154] M. Saito and A. Yabe. Dispersion and polar force components of surface-tension of some polymer-films. *Textile Research Journal*, 53(1):54–59, 1983.

- [155] A. Scherer, C. Q. Zhou, J. Michaelis, C. Brauchle, and A. Zumbusch. Intermolecular interactions of polymer molecules determined by single-molecule force spectroscopy. *Macromolecules*, 38(23):9821–9825, 2005.
- [156] J. B. Schlenoff, A. H. Rmaile, and C. B. Bucur. Hydration contributions to association in polyelectrolyte multilayers and complexes: Visualizing hydrophobicity. *Journal of the American Chemical Society*, 130(41):13589–13597, 2008.
- [157] A. Schwarcz and R. S. Farinato. Surface-tension of polymers with long unbranched side chains. *Journal of Polymer Science Part B-Polymer Physics*, 10(10):2025–2031, 1972.
- [158] M. Seitz, C. Friedsam, W. Jostl, T. Hugel, and H. E. Gaub. Probing solid surfaces with single polymers. *Chemphyschem*, 4(9):986–990, 2003.
- [159] K. A. Sharp, A. Nicholls, R. F. Fine, and B. Honig. Reconciling the magnitude of the microscopic and macroscopic hydrophobic effects. *Science*, 252(5002):106–109, 1991.
- [160] S. B. Smith, Y. J. Cui, and C. Bustamante. Overstretching b-dna: The elastic response of individual double-stranded and single-stranded dna molecules. *Science*, 271(5250):795–799, 1996.
- [161] S. B. Smith, L. Finzi, and C. Bustamante. Direct mechanical measurements of the elasticity of single dna-molecules by using magnetic beads. *Science*, 258(5085):1122–1126, 1992.
- [162] N. T. Southall and K. A. Dill. The mechanism of hydrophobic solvation depends on solute radius. *Journal of Physical Chemistry B*, 104(6):1326–1331, 2000.
- [163] F. H. Stillinger. Structure in aqueous solutions of nonpolar solutes from the standpoint of scaled-particle theory. *Journal of Solution Chemistry*, 2(2-3):141–158, 1973.
- [164] L. L. Sun, D. X. Zhao, Y. Zhang, F. G. Xu, and Z. A. Li. Dna adsorption and desorption on mica surface studied by atomic force microscopy. *Applied Surface Science*, 257(15):6560–6567, 2011.
- [165] C. Tanford. Interfacial free-energy and the hydrophobic effect. *Proceedings of the National Academy of Sciences of the United States of America*, 76(9):4175–4176, 1979.

- [166] P. R. ten Wolde. Hydrophobic interactions: an overview. *Journal of Physics-Condensed Matter*, 14(40):9445–9460, 2002.
- [167] P. R. ten Wolde and D. Chandler. Drying-induced hydrophobic polymer collapse. *Proceedings of the National Academy of Sciences of the United States of America*, 99(10):6539–6543, 2002.
- [168] E. Thormann, A. C. Simonsen, P. L. Hansen, and O. G. Mouritsen. Interactions between a polystyrene particle and hydrophilic and hydrophobic surfaces in aqueous solutions. *Langmuir*, 24(14):7278–7284, 2008.
- [169] R. C. Tolman. The effect of droplet size on surface tension. *Journal of Chemical Physics*, 17(3):333–337, 1949.
- [170] R. Underwood, J. Tomlinson-Phillips, and D. Ben-Amotz. Are long-chain alkanes hydrophilic? *Journal of Physical Chemistry B*, 114(26):8646–8651, 2010.
- [171] J. A. Wagoner and N. A. Baker. Assessing implicit models for nonpolar mean solvation forces: The importance of dispersion and volume terms. *Proceedings of the National Academy of Sciences of the United States of America*, 103(22):8331–8336, 2006.
- [172] K. A. Walther, F. Grater, L. Dougan, C. L. Badilla, B. J. Berne, and J. M. Fernandez. Signatures of hydrophobic collapse in extended proteins captured with force spectroscopy. *Proceedings of the National Academy of Sciences of the United States of America*, 104(19):7916–7921, 2007.
- [173] J. Wang, Q. A. Huang, and H. Yu. Size and temperature dependence of young’s modulus of a silicon nano-plate. *Journal of Physics D-Applied Physics*, 41(16), 2008.
- [174] M. D. Wang, H. Yin, R. Landick, J. Gelles, and S. M. Block. Stretching dna with optical tweezers. *Biophysical Journal*, 72(3):1335–1346, 1997.
- [175] H. Wei and T. G. M. van de Ven. Afm-based single molecule force spectroscopy of polymer chains: Theoretical models and applications. *Applied Spectroscopy Reviews*, 43(2):111–133, 2008.
- [176] P. K. Weissenborn and R. J. Pugh. Surface tension of aqueous solutions of electrolytes: Relationship with ion hydration, oxygen solubility, and bubble coalescence. *Journal of Colloid and Interface Science*, 184(2):550–563, 1996.

- [177] A. P. Willard and D. Chandler. The role of solvent fluctuations in hydrophobic assembly. *Journal of Physical Chemistry B*, 112(19):6187–6192, 2008.
- [178] J. Z. Wu and J. M. Prausnitz. Pairwise-additive hydrophobic effect for alkanes in water. *Proceedings of the National Academy of Sciences of the United States of America*, 105(28):9512–9515, 2008.
- [179] S. Wu. Surface and interfacial tensions of polymer melts .i. polyethylene, polyisobutylene, and polyvinyl acetate. *Journal of Colloid and Interface Science*, 31(2):153–161, 1969.
- [180] S. Wu. Calculation of interfacial tension in polymer systems. *Journal of Polymer Science Part C-Polymer Symposium*, (34):19–30, 1971.
- [181] Samuel H. Yalkowsky and Yan He. *Handbook of aqueous solubility data*. CRC Press, Boca Raton, Fla., 2003.
- [182] Samuel H. Yalkowsky, Yan He, and Parijat Jain. *Handbook of aqueous solubility data*. CRC Press, Boca Raton, FL, 2nd edition, 2010.
- [183] V. V. Yaminsky and E. A. Vogler. Hydrophobic hydration. *Current Opinion in Colloid & Interface Science*, 6(4):342–349, 2001.
- [184] S. Yasuda, I. Suzuki, K. Shinohara, and H. Shigekawa. Single molecular anatomy of solvophobic effects in host-guest interactions based on surface tension using atomic force microscopy. *Physical Review Letters*, 96(22):228303, 2006.
- [185] W. Zhang and X. Zhang. Single molecule mechanochemistry of macromolecules. *Progress in Polymer Science*, 28(8):1271–1295, 2003.
- [186] X. Zhang, C. J. Liu, and Z. Q. Wang. Force spectroscopy of polymers: Studying on intramolecular and intermolecular interactions in single molecular level. *Polymer*, 49(16):3353–3361, 2008.
- [187] X. Zhang, F. Shi, X. Yu, H. Liu, Y. Fu, Z. Q. Wang, L. Jiang, and X. Y. Li. Polyelectrolyte multilayer as matrix for electrochemical deposition of gold clusters: toward super-hydrophobic surface. *Journal of the American Chemical Society*, 126(10):3064–3065, 2004.
- [188] P. Zheng, Y. Cao, and H. B. Li. Facile method of constructing polyproteins for single-molecule force spectroscopy studies. *Langmuir*, 27(10):5713–5718, 2011.

- [189] R. H. Zhou, X. H. Huang, C. J. Margulis, and B. J. Berne. Hydrophobic collapse in multidomain protein folding. *Science*, 305(5690):1605–1609, 2004.
- [190] E. Zhulina, G. C. Walker, and A. C. Balazs. Modeling the interactions between atomic force microscope tips and polymeric substrates. *Langmuir*, 14(16):4615–4622, 1998.
- [191] E. B. Zhulina, O. V. Borisov, V. A. Pryamitsyn, and T. M. Birshtein. Coil globule type transitions in polymers .1. collapse of layers of grafted polymer-chains. *Macromolecules*, 24(1):140–149, 1991.
- [192] S. Zou, Y. J. Ma, M. A. Hempenius, H. Schonherr, and G. J. Vancso. Grafting of single, stimuli-responsive poly(ferrocenylsilane) polymer chains to gold surfaces. *Langmuir*, 20(15):6278–6287, 2004.

# Appendix A

## Derivation & Numerical Solution of Analytical Model

All symbols carry the same description as found in Section 4.2.1. This appendix is adapted from the Supporting Information of Li and Walker [105].

Assume:

$$V = \frac{4}{3}\pi R^3 + \pi r^2 L \quad (\text{A.1})$$

$$A = 4\pi R^2 + 2\pi r L \quad (\text{A.2})$$

WLC model:

$$F_{WLC} = \frac{k_B T}{L_p} \left[ \frac{1}{4} \left( 1 - \frac{x}{L} \right)^{-2} - \frac{1}{4} + \frac{x}{L} \right] \quad (\text{A.3})$$

Balancing  $\Delta E$  at collapsed state, at extended state interface:

$$\Delta E = F_{WLC} dx = \gamma_i dA \quad (\text{A.4})$$

$$\Delta E = F_{WLC} dx = F_{WLC} \frac{xdL}{L} \quad (\text{A.5})$$

$$\Delta E = \gamma_i dA = \gamma_i (8\pi R dR + 2\pi r dL) \quad (\text{A.6})$$

Relating  $dR$  to  $dL$ :

$$8\pi R^2 dR = -2\pi r dL \quad (\text{A.7})$$

$$4R^2 dR = -rdL \quad (\text{A.8})$$

Hence,

$$F_{WLC} \frac{xdL}{L} = \gamma_i (8\pi R dR + 2\pi r dL) \quad (\text{A.9})$$

$$F_{WLC} \frac{x}{L} dL = \gamma_i \left( 2\pi r dL - \frac{8\pi R r^2 dL}{4R^2} \right) \quad (\text{A.10})$$

$$F_{WLC} \frac{x}{L} dL = 2\pi r \gamma_i \left( 1 - \frac{r}{R} \right) dL \quad (\text{A.11})$$

$$F_{WLC} \frac{x}{L} = 2\pi r \gamma_i \left( 1 - \frac{r}{R} \right) \quad (\text{A.12})$$

Since  $F_{WLC}$  is a function of  $x/L$ , we use  $x/L$  as a variable to solve for  $R$  at each  $x/L$  value:

$$F_{WLC} \frac{x}{L} = f\left(\frac{x}{L}\right) \quad (\text{A.13})$$

$$R = \frac{r}{1 - \frac{f(x/L)}{2\pi r \gamma_i}} \quad (\text{A.14})$$

Since  $R$  and  $L$  are related by  $V$ , we can solve for  $L$ :

$$V = \frac{4}{3}\pi R^3 + \pi r^2 L \quad (\text{A.15})$$

$$L = \frac{V - 4/3\pi R^3}{\pi r^2} \quad (\text{A.16})$$

$$L = \frac{V}{\pi r^2} - \frac{4r}{3 \left( 1 - \frac{f(x/L)}{2\pi r \gamma_i} \right)^3} \quad (\text{A.17})$$

Hence, we can get  $F$  and  $x$  by parameterizing  $x/L$ :

$$x = L \frac{x}{L} = \frac{V}{\pi r^2} \frac{x}{L} - \frac{4r}{3 \left( 1 - \frac{F_{WLC}\left(\frac{x}{L}\right) \frac{x}{L}}{2\pi r \gamma_i} \right)^3} \quad (\text{A.18})$$

## Appendix B

# Derivation of Expected End-to-end Distance in FJC Model

Given:

$$\langle \vec{R}^2 \rangle = \int \int \int P(\vec{R}) \vec{R}^2 d\vec{R} \quad (\text{B.1})$$

$$\begin{aligned} \langle \vec{R}^2 \rangle &= \int \int \int_{\infty} \left( \frac{3}{2\pi Nl^2} \right)^{3/2} \exp \left[ -\frac{3(x^2 + y^2 + z^2)}{2Nl^2} \right] (x^2 + y^2 + z^2) dx dy dz \\ &= 3 \left( \frac{3}{2\pi Nl^2} \right)^{3/2} \int_{\infty} \exp \left( -\frac{3x^2}{2Nl^2} \right) x^2 dx \int \int_{\infty} \exp \left( -\frac{3(y^2 + z^2)}{2Nl^2} \right) dy dz \\ &= 3 \left( \frac{3}{2\pi Nl^2} \right)^{1/2} \int_{\infty} \exp \left( -\frac{3x^2}{2Nl^2} \right) x^2 dx \end{aligned} \quad (\text{B.2})$$

We make the substitution:

$$y = \sqrt{\frac{3}{2Nl^2}} x \quad (\text{B.3})$$

The previous equation becomes:

$$\langle \vec{R}^2 \rangle = \frac{3}{\sqrt{\pi}} \frac{2Nl^2}{3} \int_{\infty} y^2 e^{-y^2} dy \quad (\text{B.4})$$

We drive the following integral:

$$\begin{aligned}
\int_{-\infty}^{\infty} x^2 d^{-x^2} dx &= -\frac{1}{2} \int_{-\infty}^{\infty} x de^{-x^2} \\
&= -\frac{1}{2} \left( xe^{-x^2} \Big|_{-\infty}^{+\infty} - \int_{-\infty}^{\infty} e^{-x^2} dx \right) \\
&= \frac{\sqrt{\pi}}{2}
\end{aligned} \tag{B.5}$$

Apply this to the previous equation, we obtain:

$$\langle \vec{R}^2 \rangle = Nl^2 \tag{B.6}$$